PATTERN FORMATION IN FLUID INJECTION INTO DENSE GRANULAR MEDIA

A Thesis
Presented to
The Academic Faculty

by

Fengshou Zhang

In Partial Fulfillment
of the Requirements for the Degree
Doctor of Philosophy in the
School of Civil and Environmental Engineering

Georgia Institute of Technology
May 2012

PATTERN FORMATION IN FLUID INJECTION INTO DENSE GRANULAR MEDIA

Approved by:

Dr. Haiying Huang, Advisor
School of Civil and Environmental Engineering
Georgia Institute of Technology

Dr. Susan E. Burns
School of Civil and Environmental Engineering
Georgia Institute of Technology

Dr. Leonid Germanovich
School of Civil and Environmental Engineering
Georgia Institute of Technology

Dr. Paul W. Mayne
School of Civil and Environmental Engineering
Georgia Institute of Technology

Dr. J. Carlos Santamarina
School of Civil and Environmental Engineering
Georgia Institute of Technology

Dr. Christian Huber
School of Earth and Atmospheric Sciences
Georgia Institute of Technology

Date Approved: 13 March 2012

To my wife,

Zhuo (Sandra) Li,

for her endless support and love.

ACKNOWLEDGEMENTS

First of all I would like to express the special thanks to my PhD advisor, Dr. Haiying Huang. Without her endless encouragement, support and inspiration, I will certainly not be able to finish my PhD study at Georgia Tech.

I want to acknowledge my PhD thesis committee members: Dr. Susan Burns, Dr. Leonid Germanovich, Dr. Paul Mayne, Dr. Carlos Santamarina and Dr. Christian Huber, for their valuable comments and suggestions.

I want to acknowledge the help I have received from the past and present graduate students: Robert Hurt, Patrick Callahan, Longde Jin, Yifei Ma and Yixuan Sun. I also would like to express my appreciation to all Geosystems Engineering fellows who make my journey at Georgia Tech so unforgettable and pleasant.

The education software loan for the numerical codes $PFC2D^{®}$ and $PFC3D^{®}$ from Itasca Consulting Group, Inc. is gratefully acknowledged. I am indebted to Drs. Branko Damjanac, Jason Furtney and David Potyondy for the valuable discussions and mentorship.

Acknowledgment is made to the donors of the American Chemical Society Petroleum Research Fund through Grant ACS/PRF 49971-DNI9, National Science Foundation through grant NSF/CMMI-1055882 and to the past and current members of the Sand Control Client Advisory Board of Schlumberger for support of this research.

Lastly, I would like to thank my wife, Zhuo (Sandra) Li, for her endless support and love during my PhD study. I am particularly indebted to my parents, Xinbin Zhang and Xiwu Zhou, my parents-in-law, Hongshen Li and Guiying Zuo, as well as my three sisters, Xueming Zhang, Qiming Zhang and Xiaoming Zhang, for their continuous support and encouragement during my study abroad in the United States.

Contents

List of Tables

List of Figures

SUMMARY

Integrated theoretical and experimental analysis is carried out in this work to investigate the fundamental failure mechanisms and flow patterns involved in the process of fluid injection into dense granular media. The experimental work is conducted with aqueous glycerin solutions, utilizing a novel setup based on a Hele-Shaw cell filled with dense dry sand. The two dimensional nature of the setup allows direct visualization and imaging analysis of the real-time fluid and grain kinematics. The experimental results reveal that the fluid flow patterns show a transition from simple radial flow to a ramified morphology while the granular media behaviors change from that of rigid porous media to localized failure that lead to development of fluid channels. Based on the failure/flow patterns, four distinct failure/flow regimes can be identified, namely, (i) a simple radial flow regime, (ii) an infiltration-dominated regime, (iii) a grain displacement-dominated regime, and (iv) a viscous fingering-dominated regime. These distinct failure/flow regimes emerge as a result of competition among various energy dissipation mechanisms, namely, viscous dissipation through infiltration, dissipation due to grain displacements, and viscous dissipation through flow in thin channels and can be classified based on the characteristic times associated with fluid injection, hydromechanical coupling and viscoelastoplasticity.

The injection process is also analyzed numerically using the discrete element method (DEM) coupled with two fluid flow scheme, a fixed coarse grid scheme based on computational fluid dynamics (CFD) and a pore network modeling scheme. The numerical results from the two complementary methods reproduce phenomena consistent with the experimental observations and justify the concept of associating the

displacement regimes with the partition among energy dissipation mechanisms. The research in this work, though fundamental in nature, will have direct impacts on many engineering problems in civil, environmental and petroleum engineering such as ground improvement, environmental remediation and reservoir stimulation.

Chapter I

INTRODUCTION

1.1 Motivations and Research Objectives

How dense granular media behave when invaded by fluids is a subject of fundamental scientific importance and is relevant to many engineering applications, among them, grouting for ground improvement, hydraulic fracturing and waterflooding in soft formation for hydrocarbon recovery, drill cuttings reinjection for solid waste disposal and construction of permeable reactive barriers for environmental remediation. While extensive literature exists for the two limiting cases when granular media either behave as rigid porous media or are submerged in a fluid to behave as a dilute suspension, the injection process in densely packed granular media when grain displacements are coupled with fluid flow remains an area to be explored.

In the case when the dense granular media can be treated as rigid porous media, grain displacements resulted from fluid flow may be negligible and the displacement between the invading fluid and the pore fluid can be characterized by one of the following scenarios: hydrodynamic dispersion, capillary fingering, viscous fingering or stable displacement [Saffman and Taylor, 1958, Paterson, 1981, Bensimon et al., 1986, Homsy, 1987, Lenormand et al., 1988, Bear, 1988, Dullien, 1991]. Hydrodynamic dispersion occurs when the two fluids are miscible. When the two fluids are immiscible, viscous fingering, formation of patterns due to morphologically unstable interfaces between two fluids in porous media or in a Hele-Shaw cell [Saffman and Taylor, 1958, Chouke et al., 1959], may occur when a less viscous fluid is injected to displace a more viscous fluid. Furthermore, the experimental and numerical analysis in Lenormand et al. [1988] suggest that the immiscible fluid displacement patterns depend on two dimensionless parameters, namely, the capillary number, Ca, a ratio between the viscous force and the capillary force, and the viscosity ratio, M, between the invading fluid and the pore fluid. The fluid displacement can be characterized by

one of the three forms: (1) viscous fingering, (2) stable displacement and (3) capillary fingering. If the capillary number Ca is relatively large, i.e., the capillary effect is negligible, the fluid displacement is in the form of viscous fingering when the viscosity ratio $M < 1$ and in the form of stable displacement when the viscosity ratio $M > 1$. If the capillary number is very small, $Ca \ll 10^{-5}$, capillary fingering is the dominating displacement form. Meanwhile there are three statistical models, namely, invasion percolation, diffusion-limited aggregation (DLA) and anti-DLA, which can be used for describing the three displacement patterns. Invasion percolation describes the process of fluid flow through pore throats subjected to capillary pressure [Wilkinson and Willemsen, 1983]. Diffusion-limited aggregation (DLA) is the process when particles undergo random walks due to Brownian motion and cluster together to form aggregates of such particles [Witten and Sander, 1981]. The anti-DLA was firstly used to describe the stable displacements in a porous media by Paterson [1984]. The anti-DLA process consists of having a compact aggregate of initial particles with random walkers close by. When a random walker reaches an initial particle of the aggregate, then both the random walker and the initial particle are removed causing the aggregate size to be decreasing.

In the case when the grains are submerged in a fluid and the solid concentration is relatively low, the solid particles can be assumed to follow the fluid flow field and the grain displacements affect fluid flow only through the local solid concentration. The grain and fluid mixture can be considered as an apparent fluid with the effective viscosity $\eta = \eta_0 f(\phi)$, where η_0 is the clean fluid viscosity and $f(\phi) > 1$ is a function of the particle concentration ϕ [Einstein, 1905, Batchelor, 1967, Stickel and Powell, 2005]. As a result, the process of fluid injection into a grain-fluid mixture can be viewed as one viscous fluid displacing another viscous fluid. Pattern formation due to Saffman-Taylor type of instability has been observed in Chevalier et al. [2009] by injecting air into a granular suspension made by dispersing polystyrene beads in silicon oils in a confined linear Hele-Shaw cell, for grain fractions smaller than 50%.

Dense granular media, on the one hand, can be viewed as a nonlinear deformable

solid. Pressurization may lead to granular media responses similar to hydraulic fracturing [Khodaverdian and McElfresh, 2000, Chang, 2004, Bohloli and de Pater, 2006, de Pater and Dong, 2007, Dong and de Pater, 2008, Dong, 2010, Golovin et al., 2010, Hurt, 2012]. Under certain conditions, e.g., at large rate of deformation, dense granular media can also be considered a viscoelastic mixture of solid particles and fluid, i.e., a non-Newtonian fluid with a yield stress. The injection process may then be viewed as one viscous fluid invading another viscous fluid and the fluid-like response similar to viscous fingering may be expected. Following this line of reasoning, we therefore hypothesize that in the injection process, the granular media response may display a transition from the solid-like to the fluid-like behaviors.

The objectives of this work are to investigate the fundamental failure mechanisms and flow patterns involved in fluid injection into dense granular media and to verify the above conceptual hypothesis through an integrated experimental and theoretical analysis. In particular, we intend to address the following questions.

1. Does the transition from the solid-like to the fluid-like behaviors in the granular media response exist? If yes, what are the geometrical and physical parameters that govern the transition?

2. What are the grain displacement mechanisms in advancing localized features such as fractures or fingers? Are shear bands present in developing these localized features?

3. What are the conditions for the deformation to bifurcate from a diffuse mode (early elastoplastic deformation) to a localized mode (fracturing or fingering)?

4. How to characterize the failure geometry and flow patterns?

1.2 Research Outlines and Thesis Structures

Both experimental and theoretical analyses are carried out in this work. The experimental analysis focuses on the coupled fluid-grain displacement process when dry dense granular media are invaded by a Newtonian fluid. The injection experiments

utilize a novel setup based on the Hele-Shaw cell. The Hele-Shaw cell is a common analogous model that has been used to study the fluid-fluid displacement process in porous media. The logic for the analogy lies in the common linear relationships between the pressure gradient and the flow velocity in the equations for flow in a slot (Poiseuille's equation) and for flow in porous media (Darcy's law) [Saffman and Taylor, 1958]. In other words, pattern formation in both cases is due to Laplacian growth. In our experiments, since the Hele-Shaw cell is filled with dry sands not just fluids, in this context, the Hele-Shaw cell here is only a two-dimensional representation of the porous media. The Hele-Shaw cell has the unique advantage in allowing real-time visualization. Image processing techniques including Particle Imaging Velocimetry (PIV) are employed to analyze the development of the displacement patterns.

The injection process is also analyzed numerically using the Discrete Element Method (DEM) coupled with two fluid flow schemes: a Computational Fluid Dynamics (CFD) scheme and a pore network model scheme. The software packages $PFC3D^{®}$ with its add-on $CCFD$ (Coupled Computational Fluid Dynamics) option and $PFC2D^{®}$ with the pore network model option are used. The problem of fluid injection into granular media is multiscale in nature, involving both the grain/pore scale and the Darcy scale. DEM coupling with these two fluid flow schemes are therefore complementary in understanding the multiscale nature of the problem.

The thesis is organized as follows.

Chapter 1 "**Introduction**" outlines the motivations and objectives of this study.

Chapter 2 "**Injection Experiments in a Radial Hele-Shaw Cell**" presents the experimental observations obtained from the injection tests conducted in a radial Hele-Shaw cell filled with dry Ottawa F110 sand with aqueous glycerin solutions used as the invading fluid. In particular, we examine how the failure/flow mechanisms in the injection process are affected by the fluid viscosity and the injection velocity.

Chapter 3 "**Classification of Displacement Regimes and Growth Mechanisms**" presents the classification of the displacement regimes based on the global features characterizing pattern formation and the considerations of the characteristic

times associated with fluid injection, hydromechanical coupling and viscoelastoplasticity as well as image analysis on dynamics of tip growth mechanisms.

Chapter 4 "**DEM/CFD Coupling Analysis**" investigates numerically the failure mechanisms induced by fluid pressurization in a cylindrical wellbore in purely frictional media using the DEM code $PFC3D^{®}$ with the Coupled Computational Fluid Dynamics ($CCFD$) add-on option.

Chapter 5 "**DEM/Pore Network Model Coupling Analysis**" examines the injection process using the DEM code $PFC2D^{®}$ with the pore network model coupling option.

Chapter 6 "**Conclusions and Future Work**" summarizes the main findings obtained from this thesis and gives some suggestions for the future work.

Chapter II

INJECTION EXPERIMENTS IN A RADIAL HELE-SHAW CELL

2.1 Introduction

Fluid injection experiments are conducted in a radial Hele-Shaw cell to investigate the fundamental failure/flow mechanisms when dense granular media are invaded and displaced by a fluid and to verify the conceptual hypothesis on whether there is a transition from the solid-like to the fluid-like behaviors in the granular medium response. In particular, the effects of fluid viscosity and the injection velocity are examined.

In the literature, only a handful of injection tests have been conducted in the Hele-Shaw cells filled with dense granular media. Observations of "granular fingering" is first reported in air injection into dry powder in van Damme et al. [1993]. The pattern formation is remarkably similar to the morphology in viscous fingering in the fluid/fluid displacement in Hele-Shaw cell.

Johnsen et al. [2006] conducted a series of tests by injecting air into loose dry granular media, consisted of polydisperse spherical glass beads, in a radial Hele-Shaw cell. The experiments were conducted by applying constant pressure at the inlet. Depending on the applied pressure level, four types of behaviors were observed: (a) no particle displacement, (b) particles were displaced and a roughly circular cavity appeared near the inlet, (c) the displacement front lost its circular symmetry and branches started to develop, and (d) one main empty finger broke through the granular packing and created an eroded channel. It was observed that air flow compacted the grains around the inlet and the compaction zone front grew with time. Similar observations were also obtained in the injection experiments in a linear Hele-Shaw cell in Johnsen et al. [2008a,b]. Meanwhile Cheng et al. [2008] conducted injection

experiments using air to displace monosphere glass beads. They demonstrated that the particle-gas interface exhibited a fractal structure and sharp cusp predicted for the zero-surface-tension limit of viscous fingering analysis for the fluid-fluid invasion in Hele-Shaw cells in Bensimon et al. [1986]. The cusp shape predicted for the zero-surface-tension limit differed from the structures in Newtonian fluids where the finger tips were always round owing to the existence of surface tension.

Pinto et al. [2007] reported a solid-like to fluid-like transition in the patterns in grain/grain invasion experiments in a Hele-Shaw cell. The interface between the invading grains and the grains initially inside the domain changes from a circular shape to become fingered as the size ratio of the two species increases. In this case, the fingered pattern is mainly due to the influence of crystallization. The hexagonal packing allows the fingers to propagate in preferential directions where grains are lined up.

Lemaire et al. [1991] studied pattern formation in water injection into a clay suspension in a radial Hele-Shaw cell. The results show that there exists a transition from a viscous fingering regime producing fractal patterns of "fingers" to a viscoelastic fracturing regime producing fractal patterns of "cracks". The transition is controlled by several parameters including the Deborah number $De = t_r/t_{fl}$, where t_r is the internal relaxation time of the suspension and t_{fl} is the time scale of the flow event. The system behaves as a Newtonian fluid when $De \ll 1$ and an elastic solid when $De \gg 1$ [Macosko, 1994]. Similar transition from the fingering pattern to the fracturing pattern was also observed when water is injected into an associating-polymer solution [Zhao and Maher, 1993].

Hirata [1998] studied the pattern formation of air intrusion into an agar gel in a Hele-Shaw cell. By varying the concentration of agar and the injection pressure of air, the follow types of behaviors were observed: (a) viscous fingering, (b) viscoelastic fracturing, (c) single plane cracking, and (d) no growth. The pattern transition is attributed to the crossover of the agar gel from a viscous fluid to an elastic solid.

The experiments in Chevalier et al. [2009] were performed by injecting air into a granular suspension made by dispersing monosize polystyrene beads in silicon oils

in a confined linear Hele-Shaw cell. Effect of the grain fraction on the displacement patterns was investigated. When the grain fraction was lower than 50%, the suspension behaved as an apparent fluid and the displacement process can be quantitatively related to viscous fingering of Saffman-Taylor type. When the grain fraction was higher than 55% but slightly below 60%, the granular matrix behaved as a weak porous medium and thin air fingers breaking and reorganizing the jammed packing of grains were observed.

Injection experiments have also been performed in conventional triaxial cells for the purpose of studying hydraulic fracturing in unconsolidated materials. Comprehensive experiments were conducted in Khodaverdian and McElfresh [2000] and Bohloli and de Pater [2006], de Pater and Dong [2007], Dong and de Pater [2008], Dong [2010] to investigate the effects of fluid rheology, the leakoff characteristics and the confining stresses on the fracturing process in compacted sand.

It should be noted that X-ray CT (Computed Tomography) was employed in a series of injection experiments in Dong and de Pater [2008]. Two types of failure mechanisms for injection in water-saturated sands plus cement was observed. Due to the differences in the fluid rheology and the leakoff characteristics, while the observed feature resembled a brittle fracture in injection with a crosslinked gel, failure seemed to be associated with shear bands for injection with grout, a bentonite slurry with cement and sands.

Research on hydraulic fracturing in unconsolidated materials is also active in the group led by Prof. Leonid Germanovich in the GeoSystems group, Georgia Tech [Chang, 2004, Hurt, 2012]. Chang [2004] performed experiments by injecting solidifying fluids into dry particulate materials in triaxial cells while recording the injection pressure history and observing the fracture shape post-mortem after the solidification of the fracturing fluid. Extensive experiments were conducted by varying controlling parameters such as the properties of particulate materials and fracturing fluids, boundary conditions, initial stress states, and injection volumes and rates. The observed geometry of the hydraulic fractures and the injection pressure suggested that the hydraulic fracturing occurs in the following sequence: (a) cavity expansion, (b)

fracture initiation, and (c) fracture propagation. Three types of fracture footprints were observed: (a) beveled, (b) fingering, and (c) round. Accordingly, three physical mechanisms of fracture propagation corresponding to the three observed front types were suggested: (a) shear banding, (b) induced cohesion, and (c) "pile driving" or cavity expansion. Chang suggested that the compressive stress state would be an important characteristic of hydraulic fracturing in particulate materials with low or no cohesion. There was a threshold value of cohesion below which the materials can be considered to be effectively cohesionless. Hurt [2012] performed hydraulic fracturing experiments in saturated particulate materials in a triaxial cell. The main conclusion of his work was that toughness (resistance) to fracture propagation is an inherent characteristic of cohesionless particulate materials. A theoretical model of toughness-dominated hydraulic fracturing was applied to match the experimental pressure-time curve with only one fitting parameter. The experimental results showed that the fracture initiation pressure is mainly governed by the confining stress while the morphology of the fracture and leakoff zone changes not only with stresses but also with other parameters such as flow rate, fluid rheology and permeability. Multiple small branches and blunt fracture tip were typical feature of the fractures.

Golovin et al. [2010] and Jasarevic et al. [2010] carried out hydraulic fracturing experiments in cohesionless sand using gel with different solid concentrations. Sand was compacted in a stiff chamber with three dimensional stress control. The effects of injection rate, solid concentration and confining stress magnitude and anisotropy on the created hydraulic fractures were explored. Results show that depending on the values of these parameters, four different mechanisms can be defined: matrix flooding, cavity formation, single fracture formation and multiple branching stochastic fracturing. Increasing the injection rate or lowering the filter cake building solids concentration can have similar effects. Both cases display a transition from a roughly planar fracture to a more chaotic or diffuse fracture network and possible cavity formation.

Besides using unconsolidated sand as the injection media, hydraulic fracturing experiments were also studied in fine grain soils such as silt and clay. Murdoch

[1993a,b,c] carried out laboratory hydraulic fracturing experiments by injecting dyed glycerin into silty clay confined with in a triaxial loading cell. A fluid lag zone at the fracture tip, typical of a fluid driven fracture in brittle rocks, was observed. With the material toughness as the fitting parameter, the pressure history in this case can be very well matched by a linear elastic fracturing model. Soga et al. [2004, 2006] performed multiple epoxy injection tests in the laboratory on clay specimens prepared at different overconsolidation ratios to investigate the fracturing mechanism involved in grouting in soils. The grout efficiency, defined as the ratio of the volume of heave achieved to the injected grout volume, was close to 1 for highly overconsolidated clay, irrespective of grout spacing and injection sequence. However for normally consolidated and lightly overconsolidated clays, the grout efficiency increased when the separation in space and time between the injections was reduced.

Shin and Santamarina [2010] investigated hydraulic fracturing in a particulate material consolidated from a Ca-montmorillonite slurry based on the particle-scale mechanisms. Their work focused on the effective stress compatible mechanisms for fracture formation and propagation in unconsolidated/uncemented sediments caused by the forced invasion of either immiscible or miscible fluids. The miscibility of the invading fluid with the host fluid leads to distinct localization processes that depend on the balance between particle-level skeletal forces, capillary forces, and seepage drag forces. Each of the particle level forces is based on surface tension (T_s), contact angle (θ), particle size (d_s), viscosity (η), effective stress ($\sigma^{'}$), flow velocity (v), and can be expressed as: capillary force $F_c = \pi d_s T_s \cos\theta$; skeletal force $F_{sk} = \sigma^{'} d_s^2$; seepage force $F_s = 3\pi\eta d_s v$. Since weight and skeletal forces decrease faster than capillary and drag forces with decreasing particle size, fine-grained soils are more susceptible to fluid driven fracture formation.

2.2 Experimental Setup

2.2.1 Properties of F110 sand

Ottawa F-110 sand from U.S. Silica is selected as the granular media for the injection experiments in this study. Figure 2.1 shows the microscopic image of Ottawa F110

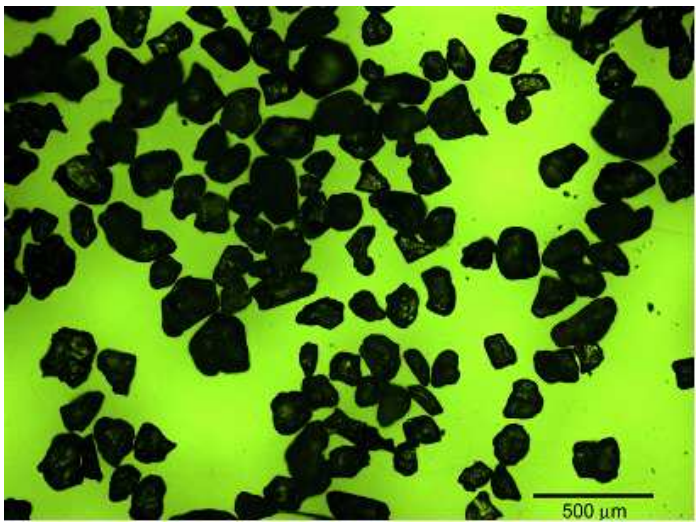

Figure 2.1: Microscopic image of Ottawa F110 sand.

Table 2.1: Index properties of F110 sand [Chang, 2004, Hurt, 2012].

Mineral		Quartz
Color		White
Angularity		Subrounded
Median particle size	D_{50} (μm)	110
Porosity	n_{max}	0.46
	n_{min}	0.35
Specific gravity	G_s	2.65
Void ratio	e_{max}	0.85
	e_{min}	0.54

sand and Figure 2.2 shows the grain size distribution curve. The index properties of F110 sand are summarized in Table 2.1.

Two sets of drained triaxial compression tests are performed following ASTM Standard at effective confining stresses of 103.42 kPa (15 psi) and 206.84 kPa (30 psi). The initial small strain elastic modulus at the effective confining stress of 103.42 kPa is around $E = 66.2$ MPa and the peak internal friction angle of the F110 sand is around $\phi = 43°$.

The permeability of the dense F110 sand is measured using a flexible wall permeameter according to ASTM standard D5084 at three different stress levels. As shown

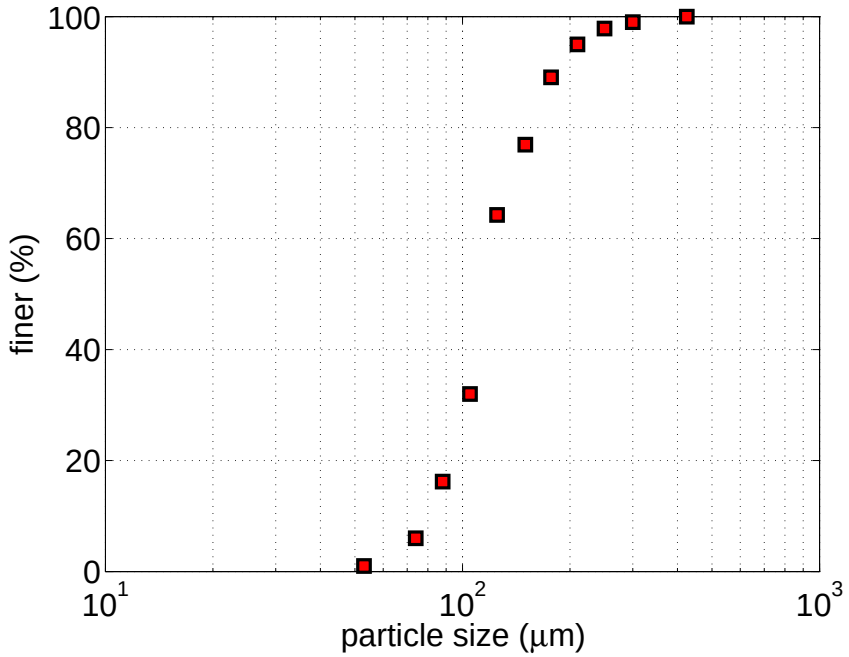

Figure 2.2: Particle size distribution curve for Ottawa F110 sand.

Table 2.2: Permeability of F110 sand at different stress levels.

Confining stress MPa (psi)	34.47 (5)	68.95 (10)	137.90 (20)
Permeability (Darcy)	1.077	0.870	0.739

in Table 2.2, the permeability of F110 sand is stress-dependent and decreases as the confining stress increases.

2.2.2 Properties of aqueous glycerin solutions

Aqueous glycerin solution is selected as the injection fluid since it is a Newtonian fluid and the viscosity can be adjusted by the glycerin weight concentration. The physical properties of glycerin are summarized in Table 2.3. Three concentrations of aqueous glycerin (50%, 90% and 100% by weight) are used and the viscosity measured at around $21°C$ is 5 cp, 176 cp and 942 cp, respectively, as shown in Figure 2.3. By changing the glycerin concentration, two orders of magnitude difference in viscosity can be achieved.

Table 2.3: Properties of glycerin [The Soap and Detergent Association, 1990].

Molecular formula	$C_3H_8O_4$
Molecular weight	92.09 g/mol
Specific gravity	1.2636(20°C); 1.2620(25°C)
Appearance	Clear
Odor	Odorless
Viscosity	1410 cp (20°C)
Boiling point	290°C (760 mm)

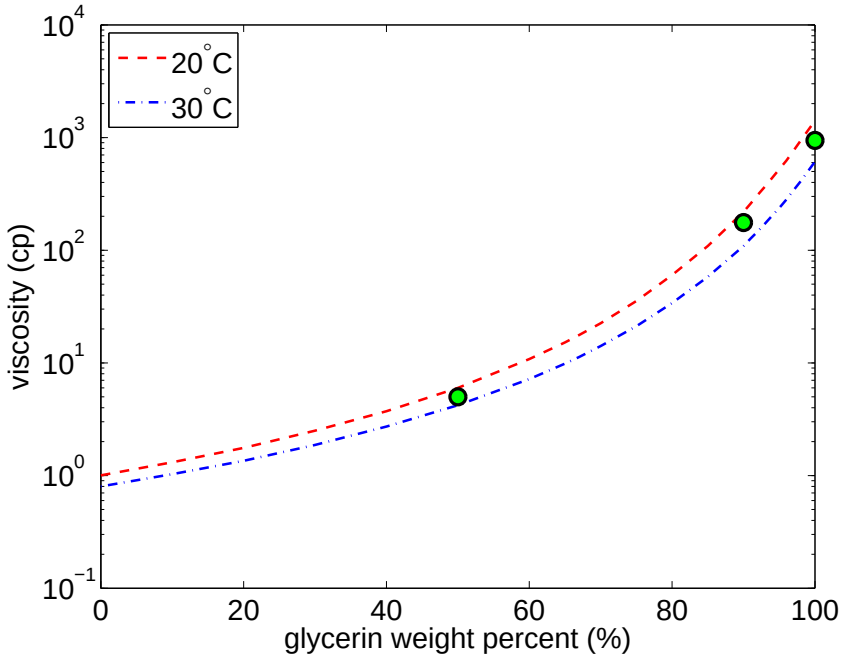

Figure 2.3: Viscosity of aqueous glycerin solutions at 20 ° C and 30 ° C [The Soap and Detergent Association, 1990]. The green dots are measured values, courtesy of Kyung Oh and Prof. Victor Breedveld.

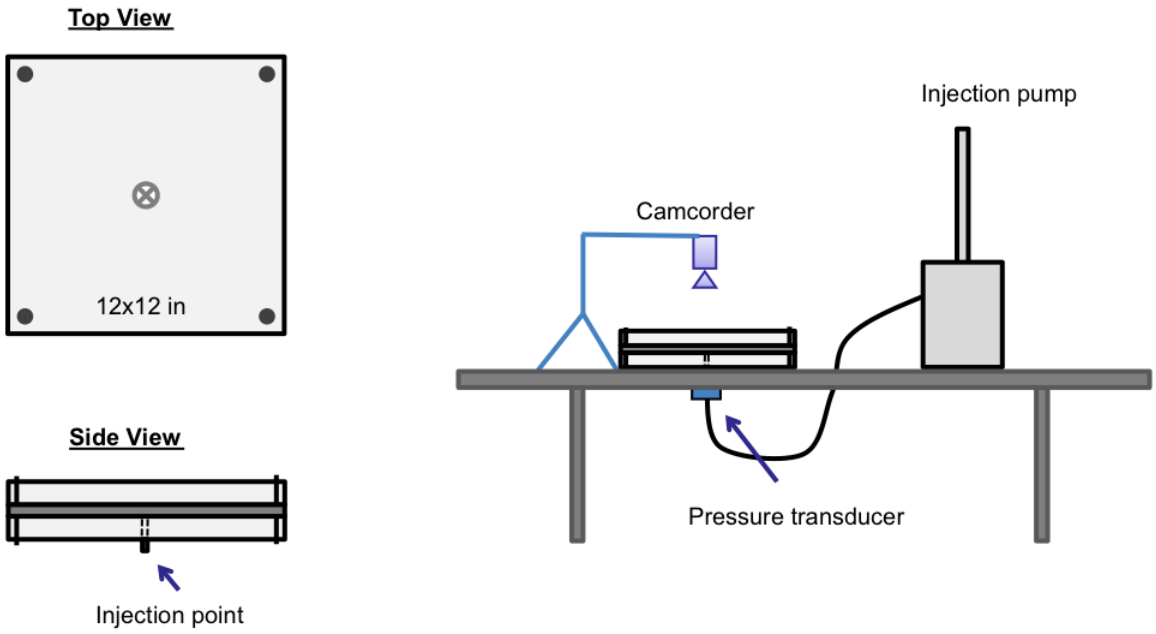

Figure 2.4: Schematic view of the experimental setup.

2.2.3 Hele-Shaw cell design

A radial Hele-Shaw cell is constructed by using two transparent polymethyl methacrylate (PMMA) plates bolted together at the four corners. The size of the square plates is 304.8×304.8 mm (12×12 in) and the thickness is 25.4 mm (1 in). The gap size between the two plates can be adjusted by adding different metal spacers in the range from 0.7874 mm to 3.175 mm. Dry sand is filled in between the two plates. The sample preparation procedure is described in the next section. Fluid can be injected from the center of the bottom plate through a drill hole of diameter $D_i = 1.016$ mm (0.04 in) using a syringe pump. The capacity of the pump in flow rate ranges from 1 ml/min to 200 ml/min. The inlet pressure history during the injection is recorded using a wireless sensor at a 50 Hz frequency. A Canon Vixia HFS100 high speed camcorder is positioned above the Hele-Shaw cell to take consecutive photos during the injection process. Schematic view of the experimental setup is shown in Figure 2.4.

2.2.4 Sample preparation procedure

A consistent procedure is implemented in order to obtain uniform dense packing within the Hele-Shaw cell. Sand is filled into the cell by rain fall from the top side in a series of successive lifts when the cell is held upright with the other three sides sealed by tape. The particles are packed by manual vibration after the placement of each lift to achieve a dense packing. After the cell is filled, it is placed on a vibration table for further compaction. Any excess voids after the vibration are filled afterward. The initial and final weight of the cell are recorded to calculate the net weight of granular material for each test. Then the porosity of each test can be calculated as the cell volume for each gap separation is pre-calibrated. The porosity obtained through such a process is around 0.35 ± 0.01. The corresponding void ratio is 0.538 which is close to the $e_{min} = 0.54$.

2.3 Experimental Observations

2.3.1 Displacement regimes

A total of 58 tests have been performed by varying three parameters: flow rate Q, gap separation b and invading fluid viscosity η. Parameters from a series of 12 representative tests are shown in Table 2.4. The normalized injection velocity v is defined according to $v = Q/(\pi b D_i)$ by assuming the injection resource is cylindrical. The series of 12 experiments is conducted at four normalized injection velocities, namely, $v = 8.22$, 82.89, 165.79 and 828.93 mm/s, while the rest of the experiments are performed at velocities in the range of $v = 8.22$ mm/s to 828.93 mm/s.

For these experiments, we may use the definition of the capillary number according to $Ca = v\eta/\gamma$, where γ is the surface tension of the glycerin solution against air. The capillary number measures the relative importance of the viscous effect over the capillary effect. For the 100%, 90% and 50% glycerin solution, the surface tension γ is set as 0.063 N/m, 0.064 N/m and 0.068 N/m, respectively. Table 2.5 gives the capillary numbers for the 12 tests. For all the tests, the capillary number Ca is larger than 10^{-5}. The Ca is the smallest in Tests A1 ($Ca = 6.04 \times 10^{-4}$) and A2 ($Ca = 6.10 \times 10^{-3}$). We may therefore assume that the capillary effect is negligible

Table 2.4: Experimental parameters for the series of 12 tests.

	50% c.w. ($\eta = 5$ cp)	90% c.w. ($\eta = 176$ cp)	100% c.w. ($\eta = 942$ cp)
$v = 8.22$ mm/s $Q = 5$ ml/min, $b = 3.175$ mm	A1	B1	C1
$v = 82.89$ mm/s $Q = 25$ ml/min, $b = 1.57$ mm	A2	B2	C2
$v = 165.79$ mm/s $Q = 50$ ml/min, $b = 1.57$ mm	A3	B3	C3
$v = 828.93$ mm/s $Q = 125$ ml/min, $b = 0.787$ mm	A4	B4	C4

Table 2.5: Capillary number for the series of 12 tests in Figure 2.5.

6.04×10^{-4}, (A1)	2.26×10^{-2}, (B1)	1.23×10^{-1}, (C1)
6.10×10^{-3}, (A2)	2.28×10^{-1}, (B2)	1.24, (C2)
1.22×10^{-2}, (A3)	4.56×10^{-1}, (B3)	2.48, (C3)
6.10×10^{-2}, (A4)	2.28, (B4)	12.39, (C4)

in all of these tests.

We may also define the Reynolds number according to $Re = \rho v b/\eta$, where ρ is the density of the aqueous glycerin solution. For the 100%, 90% and 50% glycerin solution, the density ρ is set as 1250 kg/m^3, 1225 kg/m^3 and 1125 kg/m^3, respectively. Table 2.6 gives the Reynolds number for the 12 tests. The Reynolds number is the largest in Tests A4 ($Re = 146.78$) and A3 ($Re = 58.57$). Though in these cases, fluid flow is in the creep regime, it can still be considered in the laminar regime. Viscous effect instead of the capillary effect or the inertia effect is therefore the dominant factor in this series of experiments.

Table 2.6: Reynolds number for the series of 12 tests in Figure 2.5.

5.87, (A1)	0.182, (B1)	0.035, (C1)
29.28, (A2)	0.906, (B2)	0.173, (C2)
58.57, (A3)	1.812, (B3)	0.345, (C3)
146.78, (A4)	4.541, (B4)	0.866, (C4)

Images from Tests A1 - C4 near the end of each test are summarized in Figure 2.5. The light-colored areas are occupied by dry sand only. The black areas indicate the fluid-only areas and the brown areas are the fluid infiltrated areas. While fluid permeates through the granular medium with a nearly circular front and no fluid channels are created in Test A1, in all other test cases, fluid flow results in significant grain displacements, which in turn creates channels occupied by fluid only. We may interpret the term "granular finger" in a broad sense and use it here to describe the fluid-only areas or channels. As the invading fluid viscosity and the injection velocity increases from Test A1 to C4, we can identify a transition in the fluid flow behaviors from infiltration-dominated to infiltration-limited. Meanwhile, the response of the granular media also changes from that of rigid porous media in Test A1 to fluid-like in Test C4 where the ramified finger morphology bears resemblance to the viscous fluid-fluid displacement pattern. In Tests A2, A3 and B1, the permeation fronts remain nearly circular and are affected very little by the development of the granular fingers. In Tests A4, B2, B3, C1 and C2, the permeation fronts reflect the propagation of the granular fingers, but not yet the development of individual granular fingers. The fingers grow much wider than those in Tests A2, A3 and B1. In Test C4 where the fluid viscosity and the injection velocity are the largest, the permeation front now follows individual granular fingers closely.

Based on the images in Figure 2.5, we may classify the above tests into four displacement regimes, namely, (i) a simple radial flow regime (Test A1), ii) an infiltration-dominated regime (Tests A2, A3 and B1), iii) a grain displacement-dominated regime (Tests A4, B2, B3, C1 and C2), and iv) a viscous fingering-dominated regime (Test C4). Tests B4 and C3 appear to be in the transition from the grain displacement-dominated regime to the viscous fingering-dominated regime. The term "viscous fingering" is used here due to the facts that the granular finger morphology in Test C4 is similar with the viscous fingering morphology in the fluid-fluid invasion in a radial Hele-Shaw cell. Meanwhile, the fractal dimension of the finger shape in Test C4 is about $D = 1.64$ which is close to the theoretical value $D = 1.70 \pm 0.02$ for a diffusion-limited-aggregation (DLA) pattern [Witten and Sander, 1981]. The details

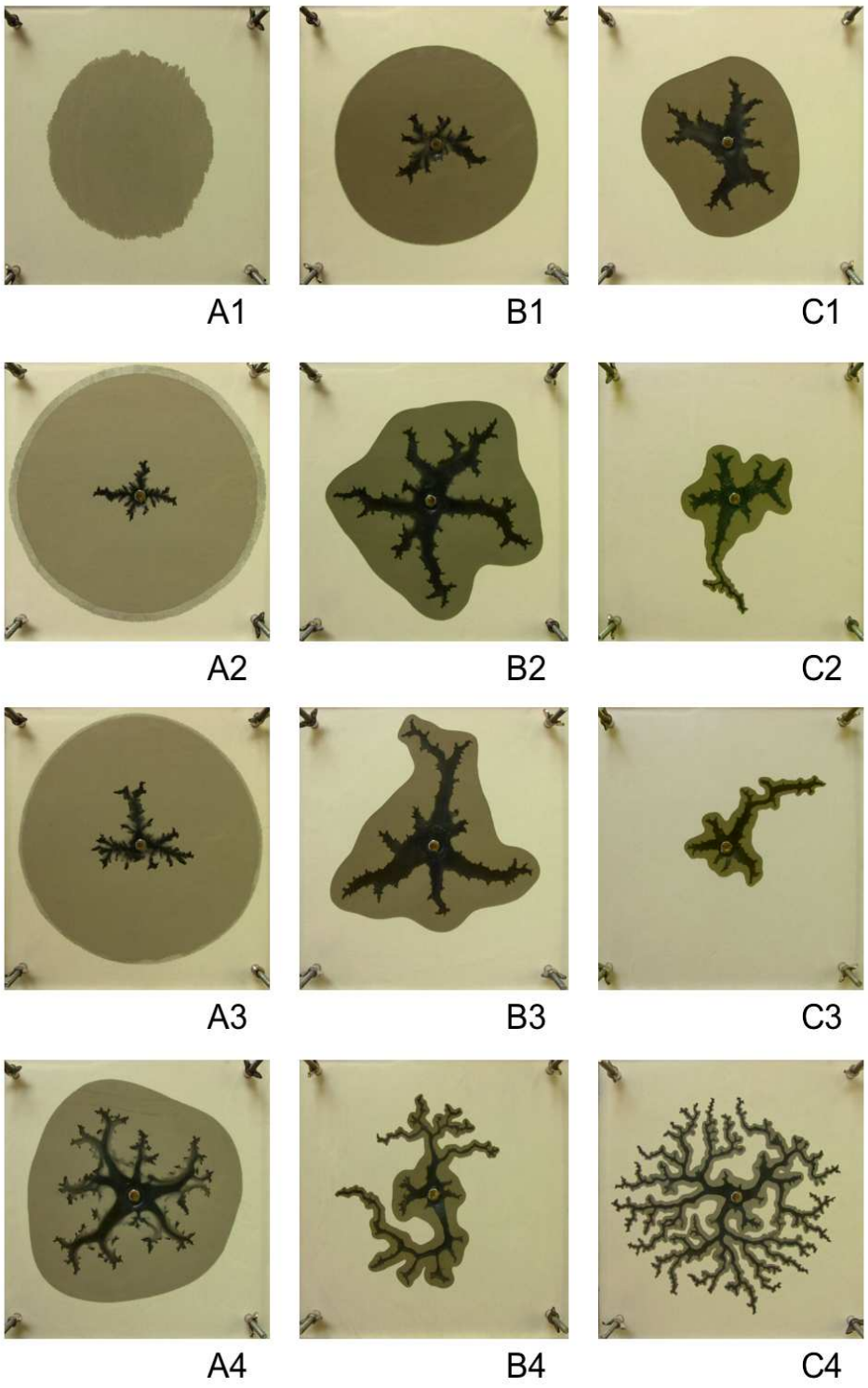

Figure 2.5: Displacement patterns from the injection of experiments with dry Ottawa F110 sand and aqueous glycerin solutions in a radial Hele-Shaw cell by varying the normalized injection velocity and invading fluid viscosity. The experimental parameters for the tests are listed in Table 2.4.

about the fractal dimension analysis will be introduced in the next chapter.

It should be noted that since the radial velocity in the domain decreases with the increase of radius, the effect of the relatively small capillary number is somewhat reflected by a narrow unsaturated outer zone at the infiltration front in Test A2 (see the image in Figure 2.5). However, the unsaturated zone can only be identified visually when the infiltration front grows close to the cell boundary. Therefore the capillary force has no effect to the propagation of the granular fingers. Due to the relatively large Reynolds number, the interface between the fluid-only area and the infiltration area in Test A4 shows evidences of erosion during the test while such interfaces remain distinctly sharp in all other tests.

2.3.2 Growth of the granular fingers and the infiltration fronts

Image analysis is conducted to identify both the granular finger area and the infiltration area at a given time during the injection tests. For each test, about 10 consecutive photos are selected and processed using a Matlab script. By overlaying the data obtained at consecutive times, time-lapse figures are created, from which evolution of the granular fingers and the infiltration patterns can be clearly identified.

Figure 2.6 shows the growth of granular fingers with time for Test A2. In this test, a small cavity forms and expands at the beginning of the injection. Later on, after the cavity has expanded to a certain size, four main fingers develop and form two nearly orthogonal sets. The finger profile is dendritic with side branches growing along the main branches. Figure 2.7 shows evolution of the infiltration area for Test A2. The infiltration front remains nearly circular during the injection process and is affected very little by the development of granular fingers. Therefore, in this test, infiltration of fluid in the porous media is the dominant process.

Figure 2.8 shows evolution of the granular finger area for Test B3 in the grain displacement-dominated regime. In this test, three main branches develop at the later stage of injection. At the perimeter of each main branch, there are short side branches which form the dendritic structure. Figure 2.9 shows evolution of the infiltration area for Test B3. The infiltration front at the early stage is nearly circular. However, as

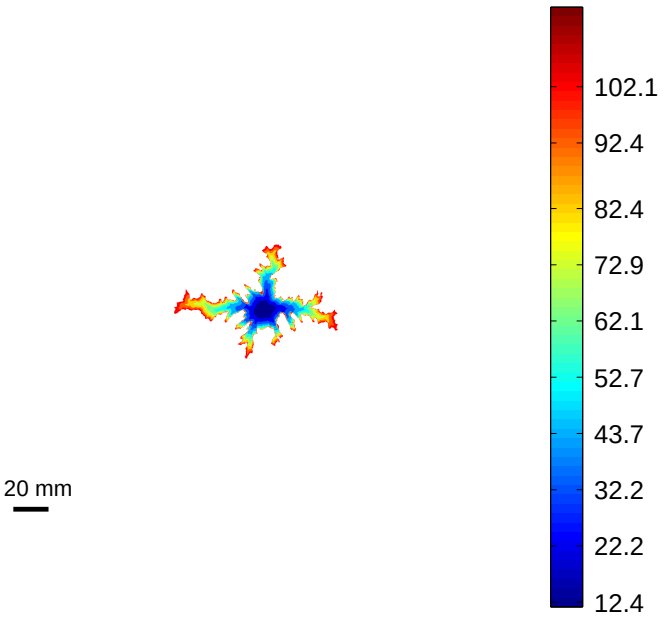

Figure 2.6: Evolution of the granular finger area for Test A2; unit in the color bar: second.

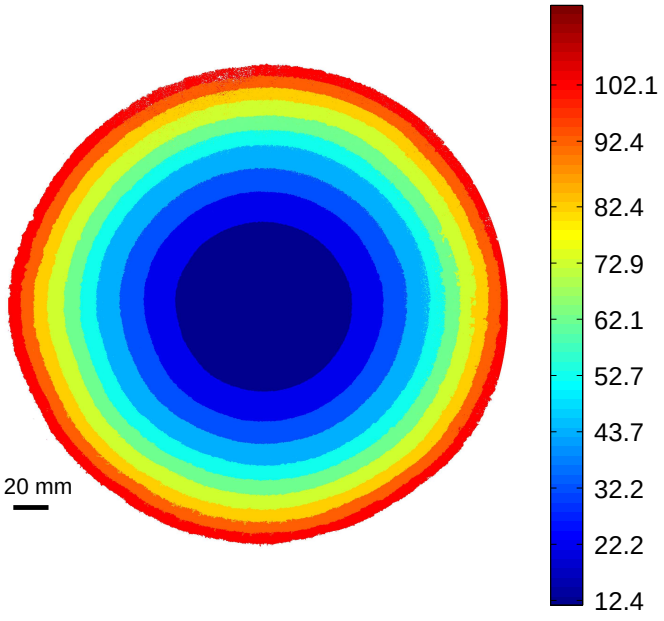

Figure 2.7: Evolution of the infiltration area for Test A2; unit in the color bar: second.

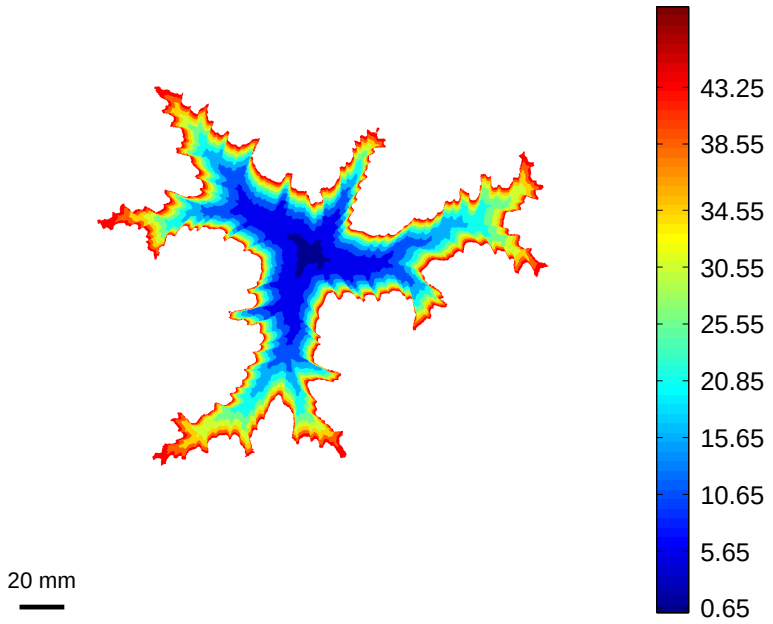

Figure 2.8: Evolution of the granular finger area for Test B3; unit in the color bar: second.

the localization of the finger branches start, the shape of the infiltration front becomes distorted to reflect the growth of the granular fingers.

Figures 2.10 and 2.11 show respectively evolution of the granular finger area and the infiltration area for Test C4 in the viscous fingering-dominated regime. This regime is characterized by the ramified morphology and very limited infiltration area. The shapes of the granular finger and the infiltration front are very similar. The width of the finger is about half of the width of infiltration area. For both the granular finger and the infiltration pattern, growth mainly takes place in the tip areas.

We argue that the formation of the displacement patterns to the competition among various forms of energy dissipation, i.e., viscous dissipation through flow in porous media, dissipation through grain displacements, and viscous dissipation through flow in thin channels. The classification of the failure/flow regimes for the injection process based on the concept of energy dissipation partition is in the same spirit as the propagation regime classification, i.e., the leakoff-dominated, the toughness-dominated and the viscosity-dominated regime, for hydraulic fracturing in hard rocks [Detournay, 2004, Detournay et al., 2007] and the classification of dense

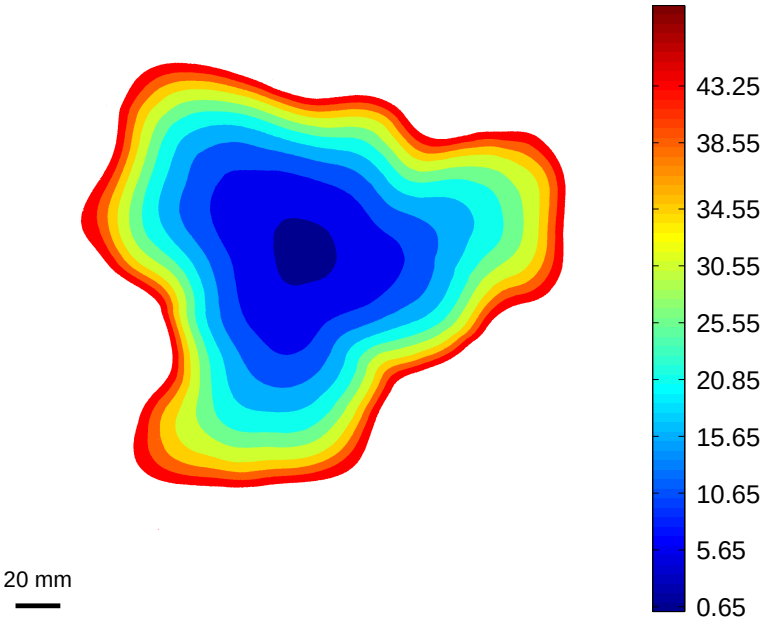

Figure 2.9: Evolution of the infiltration area for Test B3; unit in the color bar: second.

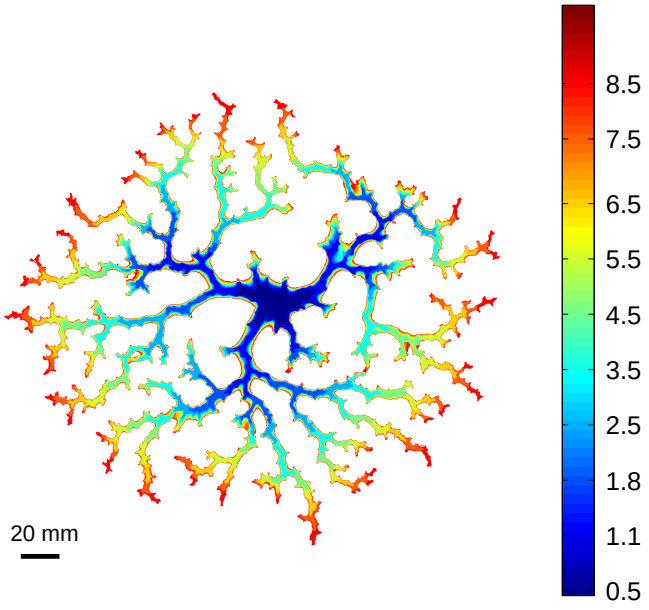

Figure 2.10: Evolution of the granular finger area for Test C4; unit in the color bar: second.

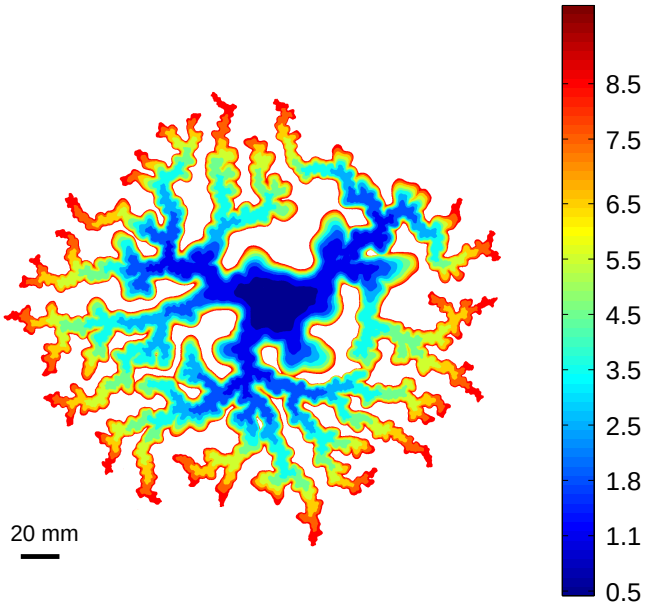

Figure 2.11: Evolution of the infiltration area for Test C4; unit in the color bar: second.

granular flow regime, i.e., frictional regime, lubrication regime and collisional regime [Coussot, 2002]. This concept of associating energy dissipation mechanisms with the displacement regimes will be verified through numerical analysis in Chapter 5.

Based on the images, global features such as the granular finger area, S_F, the area enclosed by the infiltration front, S_L, and the granular finger radius, R_F, defined as the radius of the minimal circle that contains the granular fingers, can be determined from the image analysis.

The results for Test A2 are shown in Figure 2.12. Both S_F and S_L increase nearly linearly with time in this test. The rate of increase in S_L is about two orders of magnitude higher than that in S_F. The area ratio S_F/S_L shows an initial increase and then reaches a plateau about 2.12%. We may express the variation in S_F according to

$$\Delta S \sim \Delta w \Delta R_F \tag{2.1}$$

where w is the characteristic width of the granular fingers. Therefore, if both S_F and R_F increase linearly with time as shown in Figure 2.12, we may conclude that growth of the granular fingers is mainly in one direction, in this case, in the length direction.

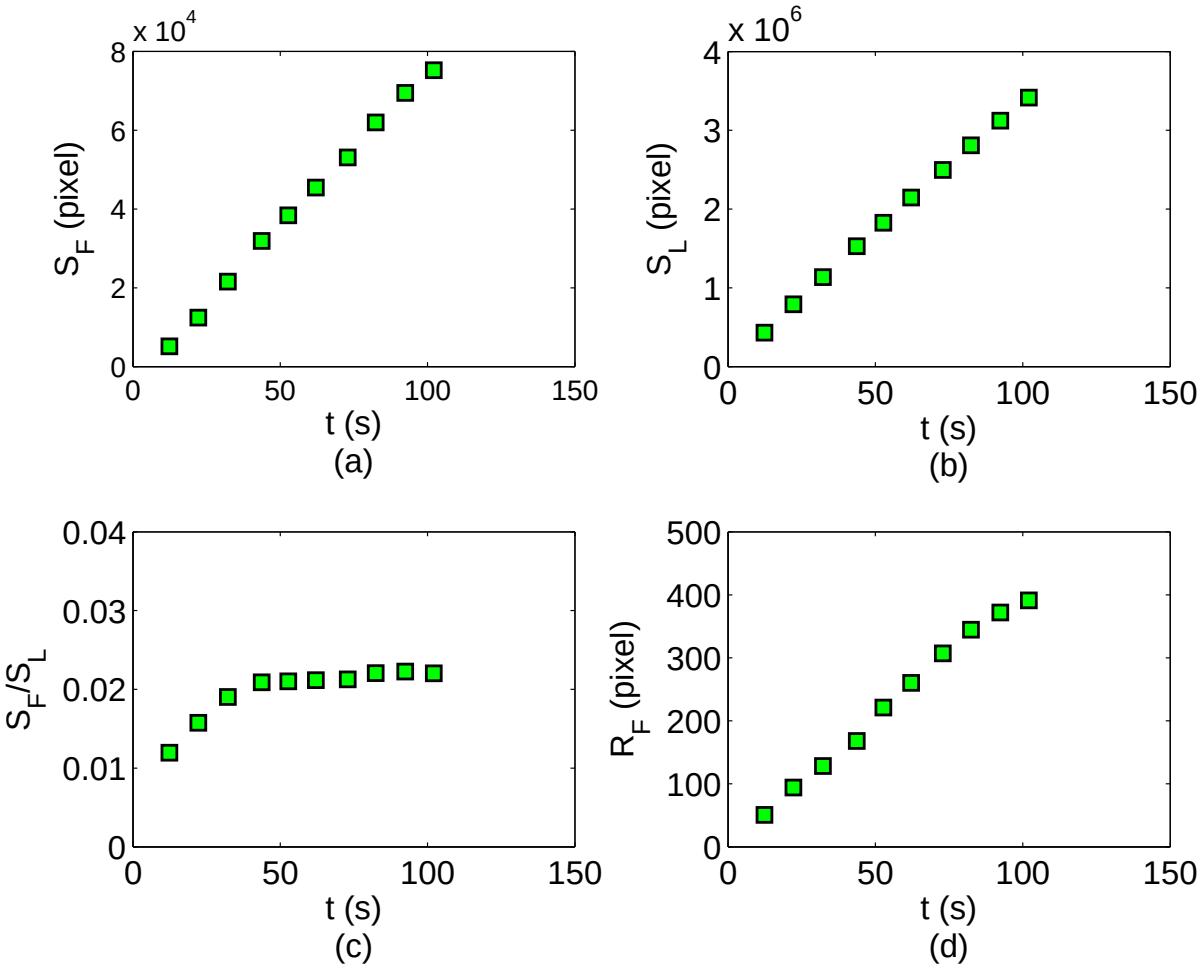

Figure 2.12: (a) Granular finger area S_F; (b) infiltration area S_L; (c) the ratio of finger area to infiltration area S_F/S_L and (d) finger area radius R_F for Test A2.

Now if S_F increases linearly while R_F increases nonlinearly as in the case of Test B3 shown in Figure 2.13, it is an indication that the granular fingers grow in both the length and width directions.

In Test B3, the rate of increase in S_L is about three times that in S_F. The area ratio S_F/S_L still shows an initial increase before it reaches a plateau around 33%. But the increasing stage (about 10 s) is relatively shorter than the one in Test A2 (about 40 s).

Figure 2.14 plots the evolution of the granular finger area S_F, and the infiltration area S_L, the area ratio S_F/S_L, and the granular finger radius R_F for Test C4. Both S_F and S_L still increase nearly linearly with time in this test. Now the rate of increase in

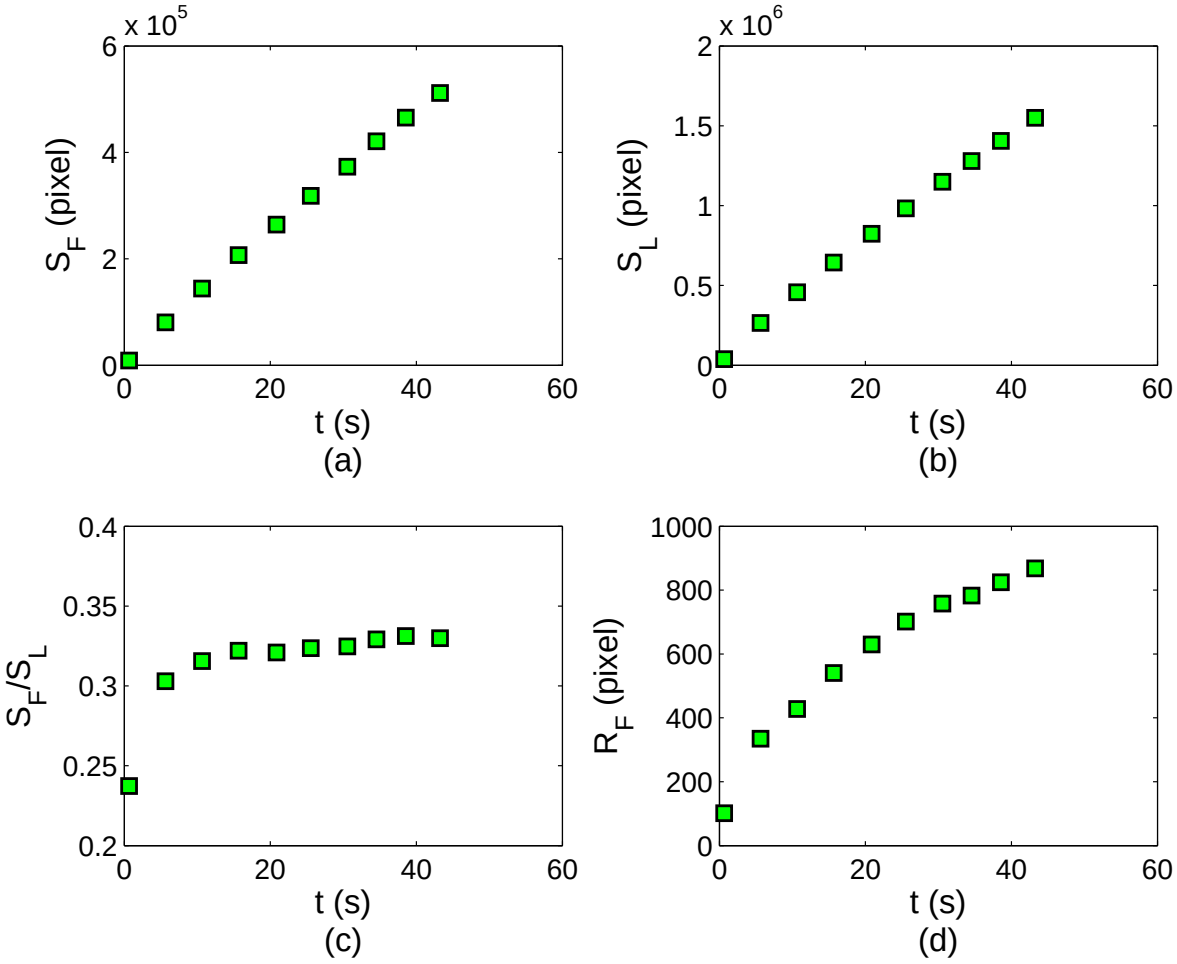

Figure 2.13: (a) Granular finger area S_F; (b) infiltration area S_L; (c) the ratio of finger area to infiltration area S_F/S_L and (d) finger area radius R_F for Test B3.

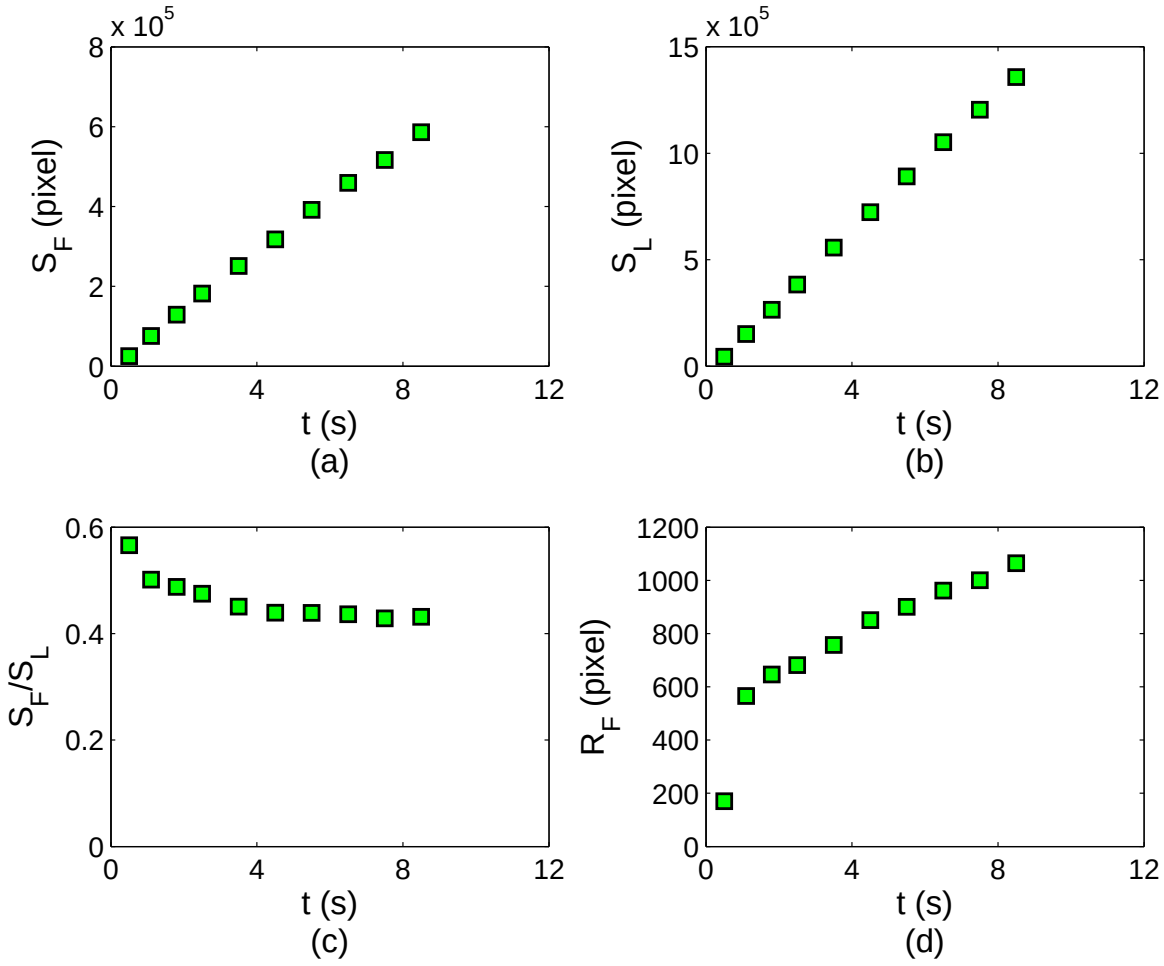

Figure 2.14: (a) Granular finger area S_F; (b) infiltration area S_L; (c) the ratio of finger area to infiltration area S_F/S_L and (d) maximum radius of the finger area to the injection point for Test C4.

S_L is about two times that of S_F. The area ratio S_F/S_L displays a trend different from Tests A2 and B3. Instead of an initial increasing stage, it gradually decreases from a large value to the steady state value. The reason is that the very high injection rate and viscosity will generate a cavity shape area of finger with an initial large S_F/S_L ratio at the beginning of the injection. The S_F/S_L reaches the steady state value after the granular fingers are well developed. The finger area radius R_F for Test C4 shows an initial jump due to the initial break through in the sand body. The linear increase in R_F after the initial jump concurs with the image analysis results in Figure 2.10 in that growth of the granular fingers are mainly in the length direction.

Denote $\lambda = S_F/S_L$ in the steady stage, e.g., the plateau value in Figure 2.12(c).

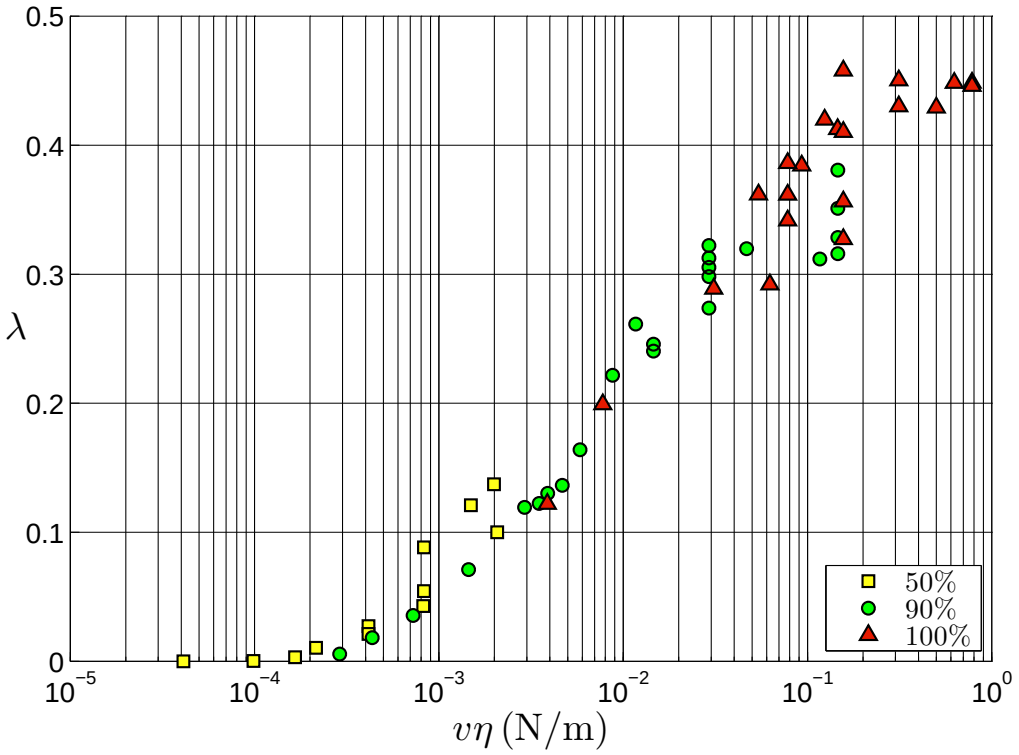

Figure 2.15: Average S_F/S_L versus $v\eta$ for all 57 tests; the tests are categorized by fluid viscosity.

This area ratio λ represents the efficiency of granular fingering, in other words, how much finger area is created given the amount of fluid injected. Figure 2.15 plot the area ratio λ versus $v\eta$ which is the combination term of the normalized injection velocity and viscosity for 57 tests. Only the result from Test A4 is not reported due to the uncertainty in determining the fluid-grain interfaces as a result of erosion. The results show an increasing trend and can be divided into four zones corresponding to the four defined displacement regimes. The condition when λ is close to zero corresponds to the simple radial flow regime. The plateau when λ is close to 0.45 represents the viscous fingering-dominated regime. If the figure is plotted in the linear scales instead of the semi-log scale, the transition zone between the two plateaus can be divided into an initial asymptotically linear region and a nonlinear region. These two regions then correspond to the infiltration-dominated regime and the grain displacement-dominated regime. As can be seen from Figure 2.15, the above classification is consistent with the observations from the images for Tests A1-C4.

2.3.3 Propagation pressure

For each test, the inlet pressure history during the injection is recorded using a wireless sensor at a 50 Hz frequency. The pressure records for Tests A1, A2, B3 and C4 are shown in Figure 2.16. In Test A1, the inlet pressure increases with time and the history can be matched by the radial flow equation assuming permeability around $k = 324$ mD, which is relatively smaller than the value ($k = 739$ mD) obtained from the measurement using the flexible wall permeameter with confining stress of 20 psi. This discrepancy in the permeability can be attributed to the slight difference in the grain fractions in the two tests as well as the entry loss at the inlet. Note also the permeability value is much smaller than the prediction from the Kozeny-Carman correlation [Bear, 1988], $k = 8.19$ D, assuming mean particle size $d_p = 110$ μm and porosity $n = 0.35$. The difference could be attributed to sphericity and angularity of the sand grains.

In all other tests, the injection pressures first increase to reach a sharp peak. When the granular fingers develop, pressure starts to decline, indicating unstable propagation. Though the pressure history is the most important piece of information in engineering practices, we have been focusing mostly on the kinematic aspect of the problem in this study and have not made an attempt to model the pressure histories. Future work is needed in modeling the pressure response in the injection process.

2.3.4 Effect of plate deformation

For each test plate deflection is expected due to the fluid pressurization. The degree of deflection can be quantitatively measured through the difference between two volumes: the actual injection volume from the syringe pump and the calculated fluid volume from image processing. The actual injection volume is obtained by simply multiplying the injection time with the injection flow rate. Based on the images, the fluid volume may be estimated from Eq. 2.2,

$$V_{image} = [S_F + (S_L - S_F)n]b\psi \tag{2.2}$$

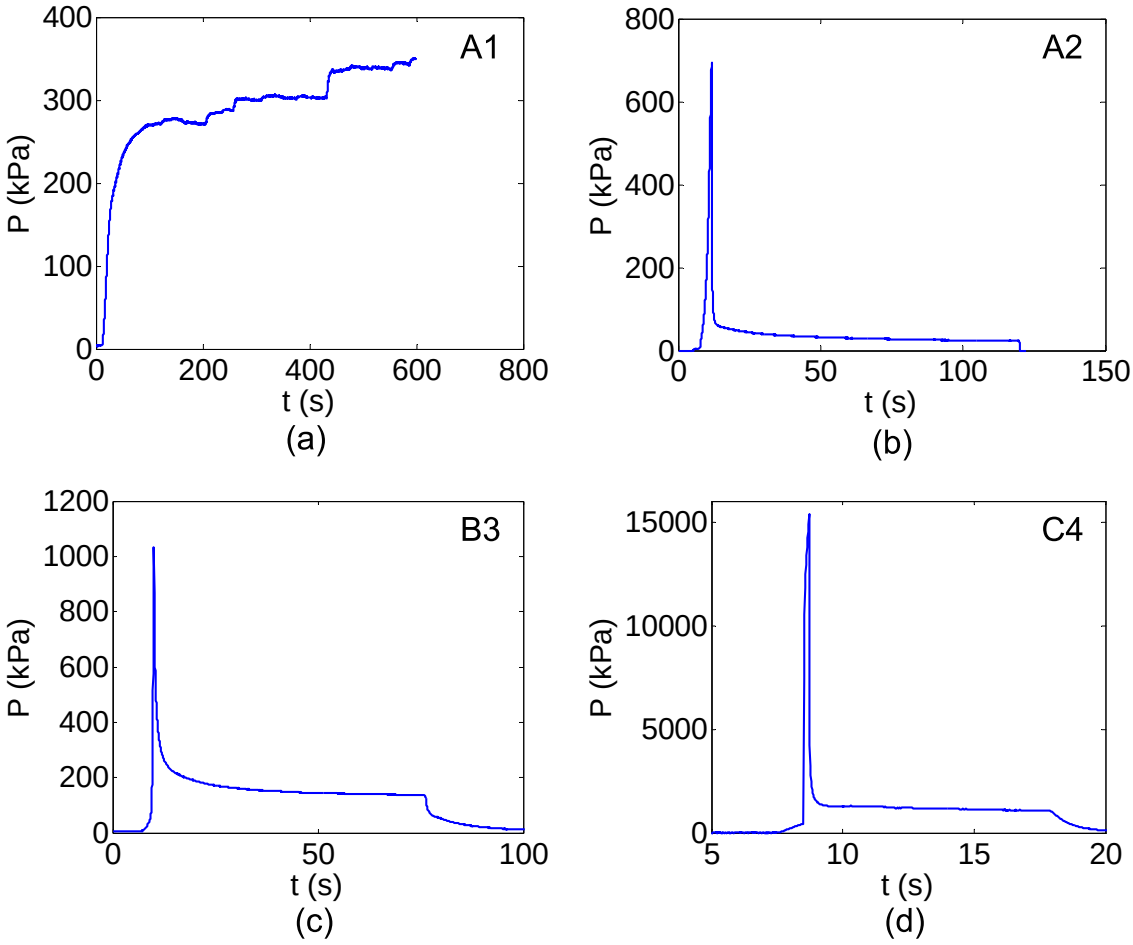

Figure 2.16: Pressure histories of (a) Test A1, (b) Test A2, (c) Test B3, and (d) Test C4.

where n is the porosity of the granular media filled in the Hele-Shaw cell and ψ is the ratio between the total number of pixel and the actual area. Porosity $n = 0.42$ is used here to reflect the fact that fluidization may occur at the fluid-grain interface. The discrepancy between the total injection volume and the fluid volume determined from the image may be attributed to the effect of plate deflection.

For each test, the actual injection volume and the fluid volume obtained from image processing can be calculated by using the S_F and S_L data from image analysis. An invading area ratio, defined as the current infiltration area to the Hele-Shaw plate area, can also be determined. The invading area ratio is the index of the percentage of the plate area that is invaded and pressed by the injection fluid and therefore affects the degree of plate deflection. Figures 2.18, 2.19, and 2.20 plot variations of the actual injection volume, the fluid volume from image processing and the invading area ratio for the three tests A2, B3 and C4, respectively. For Test A2, although the final invading area ratio is large (65.9% of the plate area has been invaded), the fluid volume from image processing is only slightly smaller than the actual injection volume. It demonstrates that the plate deflection for Test A2 is limited. For Test B3 and C4, both cases have a relatively small final invading area ratio (29.5% and 26.1% of the plate area for B3 and C4) , but the volume difference seems to indicate finite amount of plate deflection during the injection process.

Note however determination of the fluid volume from the images has large uncertainty and can only be interpreted for quality control purposes. The fluid volume determined through Eq. 2.2 depends strongly on several factors, e.g., the threshold that defines the perimeters of the granular fingers and the infiltration front as well as the local porosity inside the cell.

Compared with the fluid injection volume, the area ratio S_F/S_L is a much reliable measure of the global features. As shown in Figure 2.17, among the experiments conducted with different gap sizes but the same $v\eta$, the results are in good agreement, an indication that in the range of gap size and thickness used in our experiments, these effects may be negligible.

From the point of view of understanding the displacement regimes, if we view

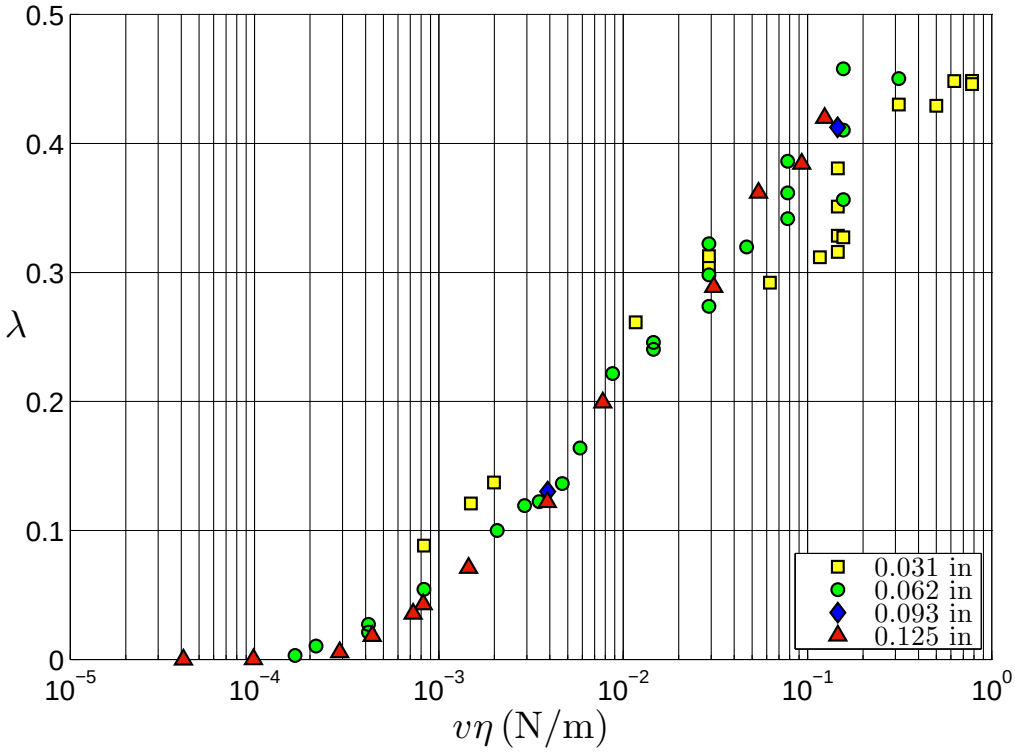

Figure 2.17: Average S_F/S_L versus $v\eta$ for all 57 tests; the tests are categorized by cell gap separation.

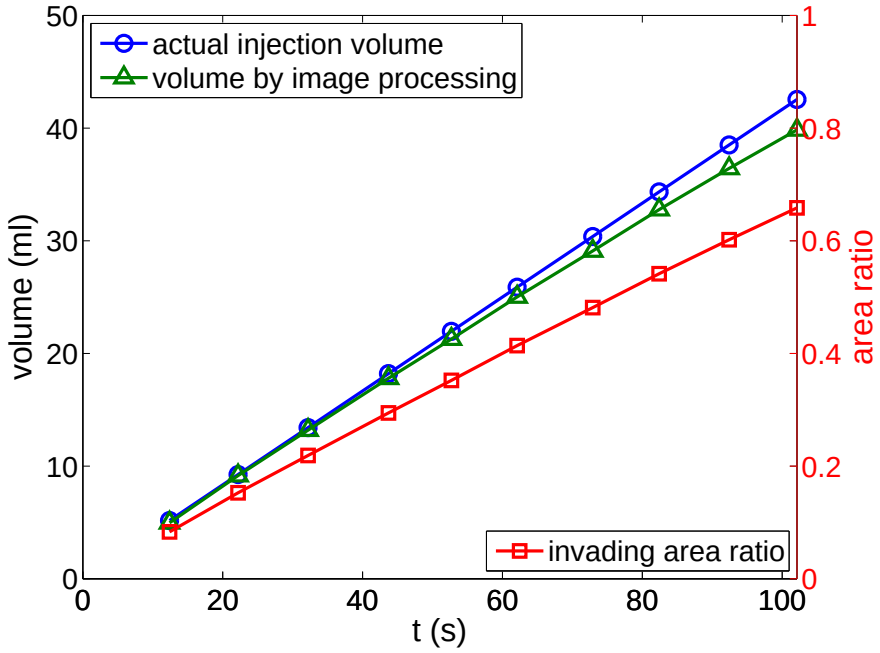

Figure 2.18: The actual injection volume, fluid volume from image analysis and the invading area ratio for Test A2.

these displacement regimes as "phases", though the boundaries between the phases may be affected by the plate deflection, the existence of the phases is not. Similar arguments can also be applied to the effect of interfacial friction between the plates and the granular media or the effect of confining stress. In addition, it is noted that the interfacial friction is a stabilizing mechanism. The effect of the interfacial friction is ignored here as similarly argued in Johnsen et al. [2006].

2.4 Conclusions

A series of injection tests with aqueous glycerin solution injected into dense dry sand are conducted in a radial Hele-Shaw cell. The experimental findings suggest that, given the same granular media properties, as the injection velocity and the fluid viscosity increase, there is a transition from the solid-like to the fluid-like behaviors in the granular media response, while fluid flow behavior shows a transition from infiltration-governed to infiltration-limited. Based on the patterns of grain displacements and fluid flow, four distinct displacement regimes can be identified from the experiments, namely, 1) a simple radial flow regime, 2) an infiltration- or

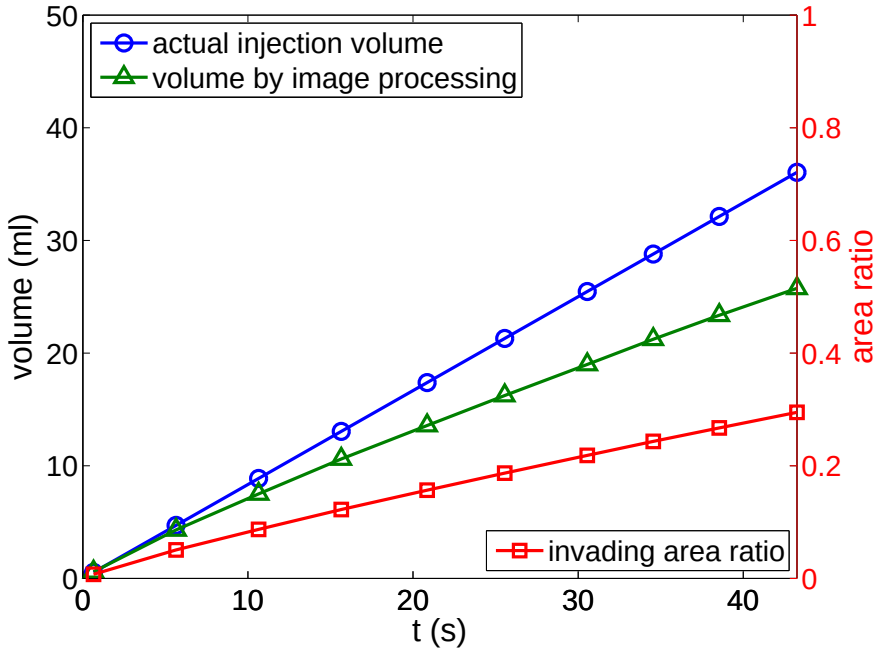

Figure 2.19: The actual injection volume, fluid volume from image analysis and the invading area ratio for Test B3.

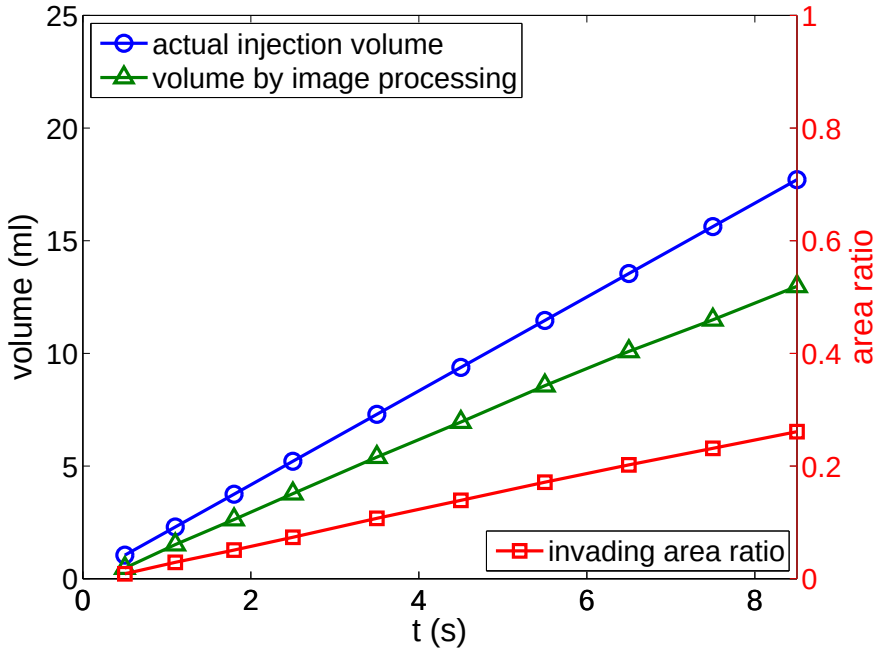

Figure 2.20: The actual injection volume, fluid volume from image analysis and the invading area ratio for Test C4.

leakoff-dominated regime, 3) a grain displacement-dominated regime, and 4) a viscous fingering-dominated regime. We argue that the formation of these displacement patterns to the competition among various forms of energy dissipation, i.e., viscous dissipation through flow in porous media, dissipation through grain displacements, and viscous dissipation through flow in thin channels. The existence of the four displacement regimes is also reflected in the variation of the area ratio λ with $v\eta$.

The Hele-Shaw cell, though limited in its capability in exploring effects such as the confining stresses, has proven to be a useful tool for understanding the fundamental failure/flow mechanisms in the injection processes. A path forward would be to first model these experiments numerically and phenomenologically and then generalize the numerical and phenomenological models to investigate the parameters of practical relevance.

Chapter III

CLASSIFICATION OF DISPLACEMENT REGIMES AND GROWTH MECHANISMS

3.1 Introduction

This chapter introduces the classification of the displacement regimes based on the global features characterizing pattern formation and on the considerations of the characteristic times associated with fluid injection, hydromechanical coupling and viscoelastoplasticity. Image analysis on the dynamics of tip growth mechanisms is also discussed.

3.2 Classification of Displacement Regimes Based on Characteristic Times

The existence of these displacement regimes may be explained by considering three characteristic times involved in the injection process. The injection time scale may be expressed as,

$$t_i = \frac{\ell}{v} \tag{3.1}$$

where ℓ is a characteristic length of the injection process and v is the normalized injection velocity. The diffusion time scale from hydromechanical coupling may be expressed as,

$$t_d = \frac{\eta \ell^2}{Ek} \tag{3.2}$$

where E is the Young's modulus, η is the fluid viscosity and k is the intrinsic permeability. The granular medium may be treated as a nonlinear viscoelastoplastic solid under certain conditions, say, at large rates of deformation. A retardation time may then be written as,

$$t_r = \frac{\eta'}{E} \tag{3.3}$$

where η' is the apparent viscosity of the granular medium. Two dimensionless times can therefore be defined for this coupled displacement process, i.e.,

$$\tau_1 = \frac{t_d}{t_i} = \frac{\eta v \ell}{Ek} \tag{3.4}$$

and

$$\tau_2 = \frac{t_r}{t_i} = \frac{\eta' v}{\ell E} \tag{3.5}$$

While the dimensionless time τ_1 determines whether the granular media response is diffusion-governed or deformation-governed, the time τ_2 characterizes the viscoelastic response of the granular media. As τ_2 increases, the material behavior shows a transition from solid-like to fluid-like. The definition of τ_2 is similar to the Deborah number for a viscoelastic fluid.

The displacement regimes can then be classified based on these two dimensionless times τ_1 and τ_2. Since the experiments in Figure 2.5 show that the fluid-like response occurs when $v\eta$ is the largest, it is reasonable to assume $t_d < t_r$ or $\tau_1 < \tau_2$. We may denote the critical values τ_d and τ_r ($\tau_d < \tau_r$) as the dimensionless times corresponding to the transitions in the granular medium response from diffusion-governed to deformation-governed and from solid-like to fluid-like, respectively. The injection process is therefore grain displacement-dominated if $\tau_d \ll \tau_1 < \tau_2 \ll \tau_r$, and viscous fingering-dominated if $\tau_2 \gg \tau_r$. When $\tau_1 \ll \tau_d$, the injection process is governed by diffusion. The experiments shown in Figure 2.5 suggest that there exists a threshold value τ_0 ($\tau_0 < \tau_d$) associated with the growth condition. When $\tau_1 < \tau_0$, given the observation time scale and experimental settings, e.g., the boundary conditions, the growth condition is either not yet met or the growth of the fingers is negligible, i.e., $d_f \ll d_p$, where d_f is the initial cavity size or the diameter of the minimal circle that contains the granular fingers. The condition, $\tau_1 < \tau_0$, therefore corresponds to the simple radial flow regime and $\tau_0 < \tau_1 \ll \tau_d$ the infiltration-dominated regime. The growth scenario in Figure 2.6, showing expansion of a circular cavity prior to the development of granular fingers, suggests that the growth condition at $\tau_1 = \tau_0$ depends on not only the local pore pressure as shown in Johnsen et al. [2006] but also the pore pressure gradient. A schematic for the classification of the displacement

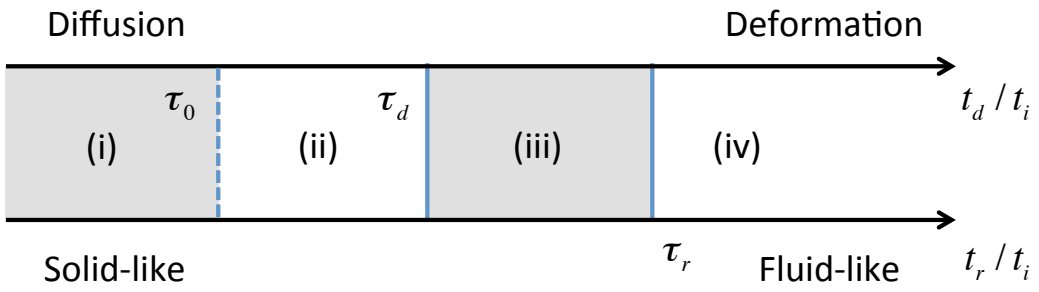

Figure 3.1: Classification of the displacement regimes based on the characteristic times involved in the injection process.

regimes based on the characteristic times is shown in Figure 3.1.

3.3 Classification of Displacement Regimes Based on Global Features

We examine here whether the "phase" boundaries or the transition between the displacement regimes can be identified from the variations of the global features as a function of the dimensionless time. We may assume that given the material properties and the characteristic process length, the diffusion time t_d and the retardation time t_r are constant. Since it is extremely challenging to determine the retardation time t_r experimentally, in the discussion below, the diffusion time t_d or the dimensionless time τ_1 will be used. In the scaling of τ_1, the inlet diameter D_i is chosen as the characteristic length ℓ.

We have shown in Figure 2.15 that variations of the area ratio λ as a function of $v\eta$ reflects the existence of the distinct displacement regimes. Variation of the area ratio λ can also be plotted as a function of the dimensionless time τ_1 for all the tests, see Figure 3.2. The results suggest that when $\tau_1 < 6 \times 10^{-3}$, growth of granular fingers is negligible. When $\tau_1 > 3$, the area ratio remains approximately constant at about 45%. In Figure 2.15 where the same results are plotted in linear scales, we can observe that at relatively small τ_1 ($\tau_1 < 0.1$), the area ratio increases nearly linearly with τ_1. The threshold values defining the transitions of displacement regimes may therefore be determined as follows: $\tau_0 = 6 \times 10^{-3}$, $\tau_d = 0.1$ and $\tau_r = 3\eta' k/\eta l^2$ (or $\tau_d = 3$). Since fluid invades ahead of the granular fingers in all the tests here, the

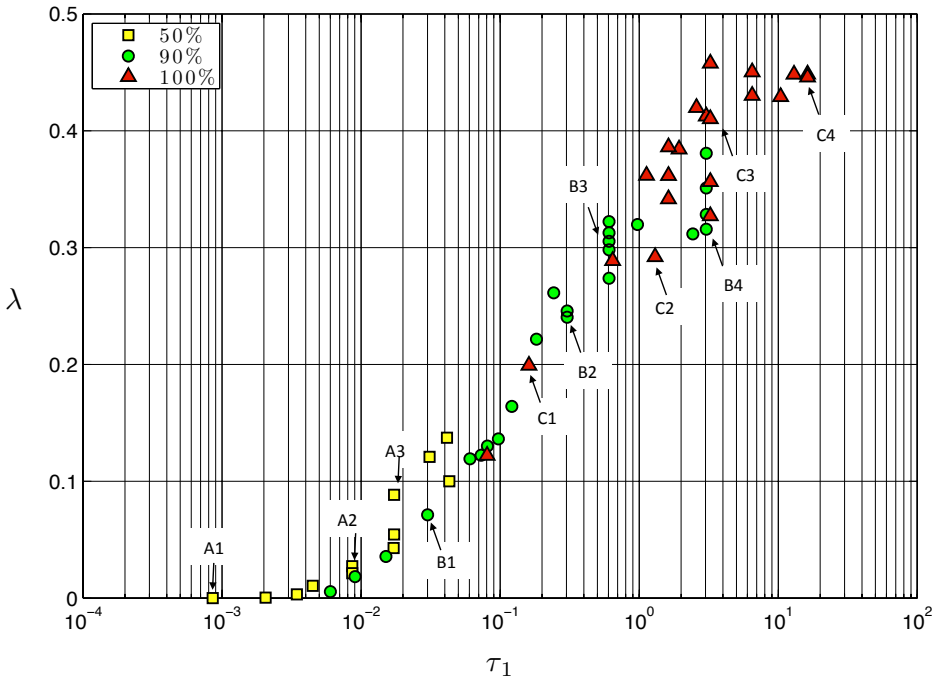

Figure 3.2: The area ratio λ vs. time ratio τ_1 for all the 57 tests. The points for the 12 tests in Figure 2.5 are marked in the plot.

apparent viscosity for a fluid and grain mixture may be expressed as $\eta' = \eta_0 f(\phi)$, where $f(\phi)$ is a function of the grain volume fraction of the mixture and $f(\phi) > 1$ for dense granular packing. Consequently, the critical time τ_r reduces to $\tau_r = 3f(\phi)\, k/l^2$.

In addition, the transitions between the displacement regimes can also be identified from the variations of the fractal dimension of the granular fingers and the infiltration front with respect to τ_1. Fractal dimension D is a statistical index indicating how completely a fractal geometry fills the space [Vicsek, 1992, Turcotte, 1997]. There are many specific definitions of fractal dimension. Box-counting fractal dimension or the Minkowski–Bouligand dimension is one of the most popular ones [Schroeder, 1991]. To calculate the fractal dimension using box-counting method, the fractal domain is discretized by square boxes and the total number of boxes which covers the fractal area is counted. The box-counting dimension is calculated based on how the box number varies with the size of the boxes. Suppose that $N(r)$ is the number of boxes of side length r required to cover the fractal, then the box-counting dimension can be defined as,

$$D = \lim_{r \to 0} \frac{\log N(r)}{\log(\frac{1}{r})} \tag{3.6}$$

For each injection test, the fractal dimensions of the infiltration area and the finger area are calculated, respectively. Figure 3.3 shows the box covering of the finger area for the Test C4 in Figure 2.5. The total number of blue boxes is counted corresponding to the selected box size. Then the total number of boxes $N(r)$ vs. the box size r is plotted in Figure 3.4. The plot shows that the total number of boxes $N(r)$ to cover the fractal area has a power relationship with the box size r. Ideally, if the fractal pattern has a large size and fine resolution, the fractal dimension could be obtained directly from the slope of the log-log plot in Figure 3.4. However the pictures from the real experiments always have a finite size and a finite resolution. When the box size r approaches the size of the entire pattern on one end or approaches the resolution of the images on the other end, $N(r)$ will deviate from the pure power law dependence. Therefore the local slope $D = -d \log N(r)/d \log r$ is analyzed as shown in Figure 3.5. By averaging the local fractal dimension in the range of box sizes bounded by the image resolution and the characteristic dimension of the image, the fractal dimension of the pattern can be estimated.

Figure 3.6 plots the fractal dimension of the granular finger and infiltration areas for all 57 tests versus the dimensionless time ratio τ_1. The fractal dimension for the granular finger area has three distinct zones. The first zone shows a nearly linear decreasing trend. When $6 \times 10^{-3} < \tau_1 < 3$, the fractal dimension is then more or less scattered in the range between 1.70 and 1.80 with an overall gradual decreasing trend. However, when $\tau_1 > 3$, the results show a distinct plateau around 1.64. The transition from the nearly linear decreasing trend to the scattered distribution marks the transition in the shape of the granular finger areas from small circular shapes near the inlet to fractal shapes propagating from the inlet. Meanwhile the results around $\tau_1 \sim 3$ indicate the transition from the grain-displacement dominated regime to the viscous fingering-dominated regime. Fractal dimension $D = 1.64$ at $\tau_1 > 3$ agrees very well with the theoretical value of $D = 1.70$ for patterns generated due to diffusion-limited-aggregation (DLA) [Witten and Sander, 1981]. The slight

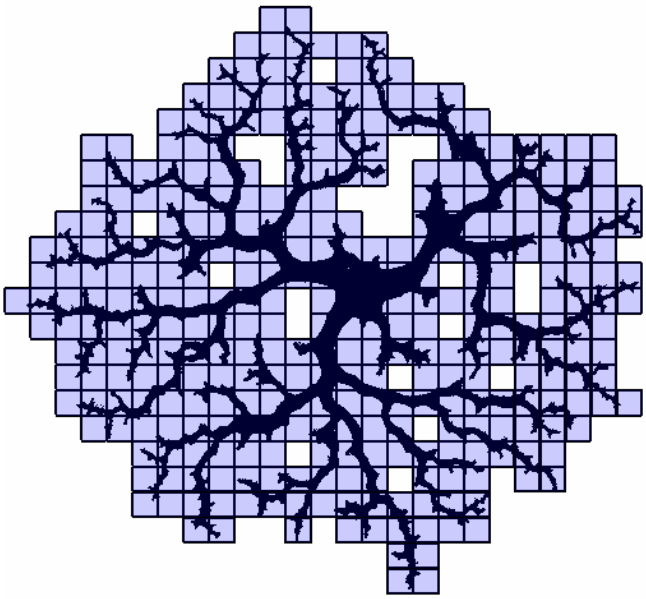

Figure 3.3: Schematic of box covering of fractal area for Test C4 in Figure 2.5.

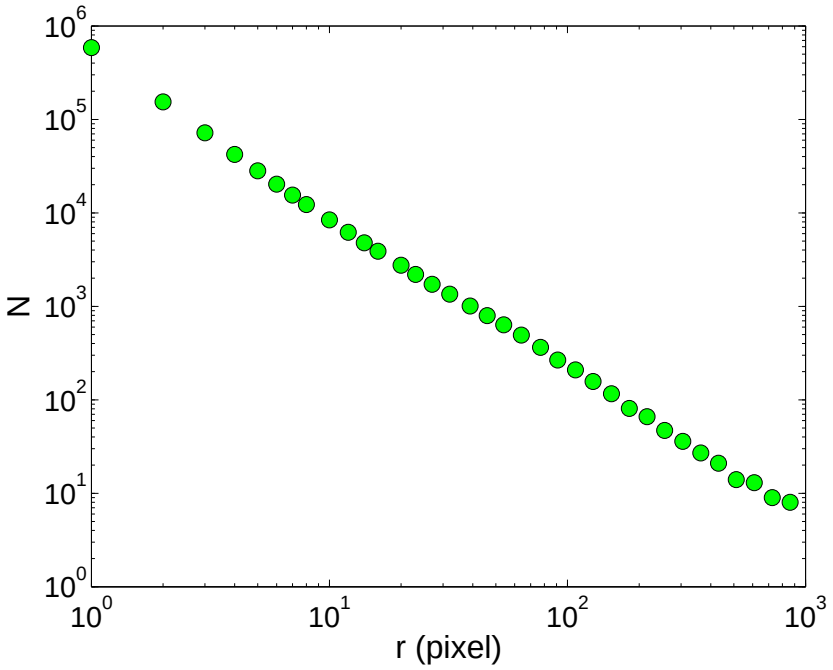

Figure 3.4: The number of boxes $N(r)$ vs. the box size r for Test C4 in Figure 2.5.

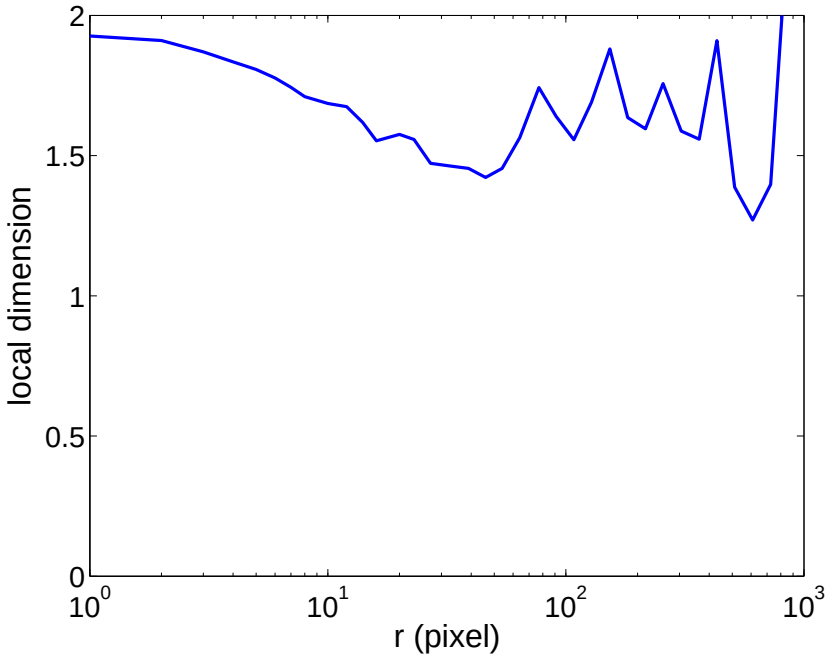

Figure 3.5: Local fractal dimension from the number of boxes $N(r)$ vs. the box size r plot in Figure 3.4.

discrepancy between the two values is likely due to the finite size and resolution of the image. The fractal dimension for the infiltration area gradually decreases from about 1.95 to about 1.8. It illustrates the gradual transition of infiltration area from a nearly circular shape to a ramified morphology. The initial plateau zone for the fractal dimension of the infiltration area represents the nearly circular infiltration zone. The crossover point from the plateau at small τ_1 to the decreasing trend could be viewed as the transition point from infiltration-dominated regime to the grain-displacement dominated regime. Then all the four displacement regimes defined in the Hele-Shaw cell experiments can be identified from Figure 3.6 and the threshold values are consistent with those identified from Figure 3.2.

3.4 Growth Mechanisms

3.4.1 Tip propagation

The capability of real-time visualization provided by the Hele-Shaw cell allows us to investigate the mechanisms of granular tip propagation. Detailed views of the propagation sequence of a granular finger tip from Test A2 are shown in Figure 3.7.

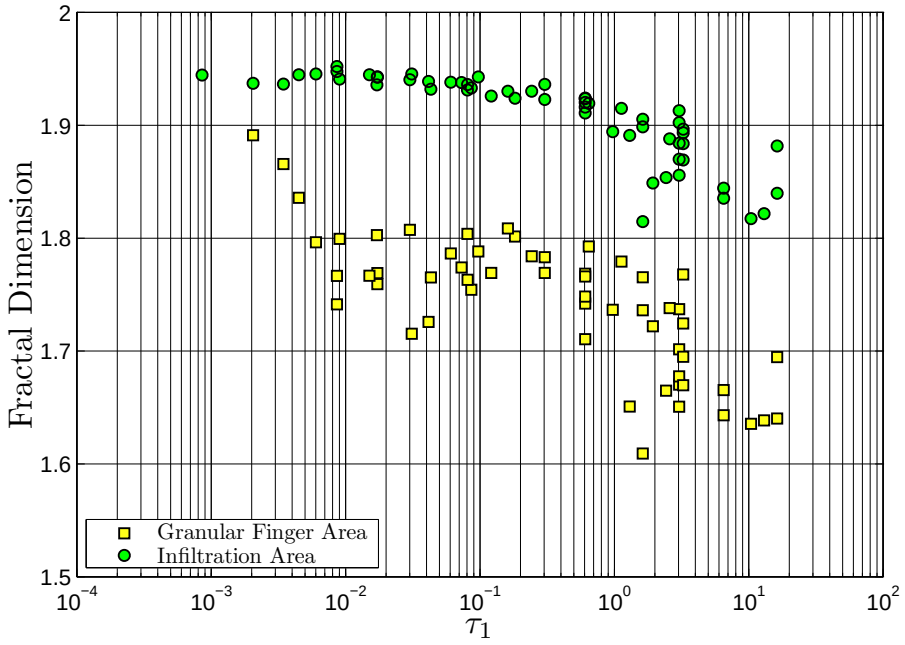

Figure 3.6: Fractal dimension of the finger and infiltration areas for all the 57 tests.

The differences between two consecutive images are shown in Figure 3.7. The white color indicates the growth area during a time interval. Initially the finger tip shape is sharp, as shown in Figure 3.7 at $t = 70.4$ s. At $t = 73.8$ s, the sharp tip becomes blunt. The blunt tip is splitted at $t = 76.2$ s with a new sharp tip at the left corner continuing to propagate. The tip propagation mechanism shown here indicates that granular fingers grow through tip blunting and splitting instead of side branching.

Images of granular finger tip growth sequence in Test B4 are shown in Figure 3.8. Test B4 is in the transition from the grain displacement-dominated regime to the viscous fingering-dominated regime. The images indicate that a sequence of tip extension, fluid infiltration and further extension. Such a sequence of events suggests that propagation of the granular tip is intertwined with fluid infiltration. Both the local pore pressure and the gradient are involved in the growth condition.

This tip splitting and blunting process is intriguing in the sense that the newly developed tip is angled around 45° with respect to the main branch, an indication that tip propagation may be a result of shear failure. In addition, blunting of the tip may be associated with local cavity expansion. Only when the local stress and the

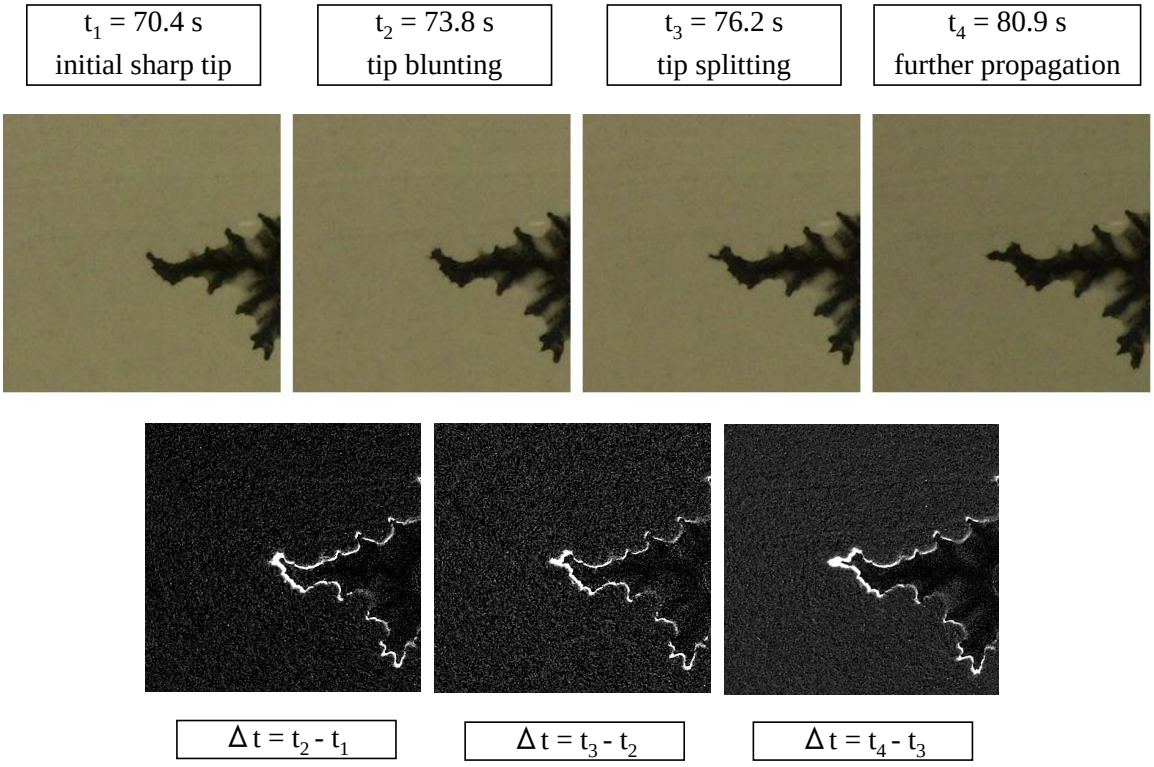

Figure 3.7: Top row: sequences of the granular finger tip propagation in Test A2; bottom row: differential images

pressure field reach certain conditions, the tip propagates again. The evidences of tip propagation due to shear failure and cavity expansion have also been observed in injection experiments in the triaxial cells [Khodaverdian and McElfresh, 2000, Chang, 2004, Bohloli and de Pater, 2006, Dong and de Pater, 2008, Golovin et al., 2010, Hurt, 2012].

3.4.2 Principles of PIV

The tip growth mechanism is also investigated by employing a novel image analysis technique PIV (Particle Image Velocimetry). PIV is an optical and non-destructive method providing quantitative measurement of instantaneous velocity and related properties [Wesrerweel, 1993, Raffel et al., 2007]. In 2D PIV, the objective plane is illuminated twice with two separate frames recorded in a camera. To start the

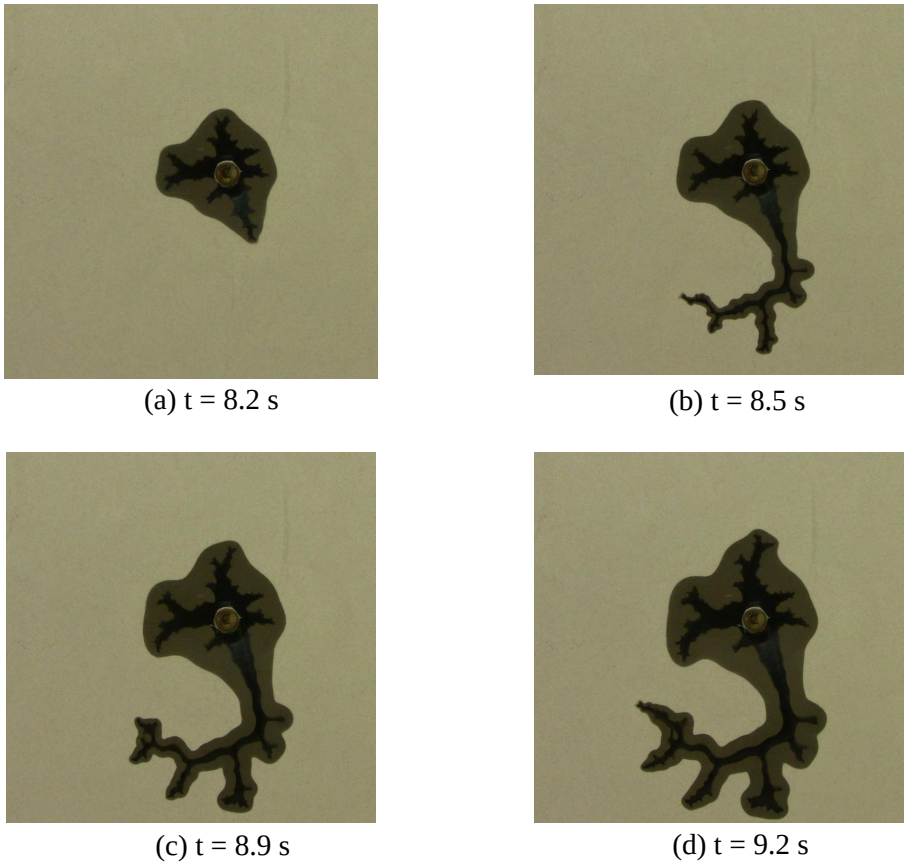

(a) t = 8.2 s (b) t = 8.5 s

(c) t = 8.9 s (d) t = 9.2 s

Figure 3.8: Images from Test B4 showing the extension-infiltration-extension sequence of granular tip growth.

evaluation, the digital data is divided into small interrogation windows. The local displacement vector of the two frames is determined for each interrogation window by applying a spatially statistical cross-correlation function. As the time interval between the two frames and the image magnification obtained from camera calibration are given, the velocity vector field attributed to the center of the interrogation window can then be obtained.

PIV technique has been widely used in fluid mechanics analysis to obtain the streamline with the fluid seeded with tracer particles. PIV can also be used to measure the velocity field of the free surface and basal boundary in a granular flow, which involves nontransparent materials [Rechenmacher and Finno, 2004, Chevalier et al., 2009, Hall et al., 2010]. The optical surface structure which is produced by illumination of the surface of the granular flow is sufficient to detect the motion.

In this work, an open source PIV software PIVlab [Thielicke and Stamhuis, 2012] is used to analyze the particle scale kinematics. The software is coded in Matlab with a graphical user interface.

3.4.3 Experimental setup

A special injection experiment is designed to apply the PIV technique. The Hele-Shaw cell with gap separation $b = 1.57$ mm is filled with a mixture of 98% F110 sand and 2% red sand of the same particle size. The red sand serves as tracer particles to enhance the visual effects. In this PIV analysis, we mainly focus on the finger tip behavior. Since the moving infiltration front could bring noise to the PIV analysis, we select the experimental conditions to ensure the displacement pattern is in the infiltration-dominated regime so that the infiltration front can be excluded from the picture frame. Fluid is first injected into the granular media at a rate of 5 ml/min to first saturate the granular media. After the majority part of the domain is saturated, the injection rate increases to 25 ml/min to create the fingers. The camera is set to zoom into the area of only one finger branch.

3.4.4 Tip kinematic analysis

A series of 9 consecutive pictures recording the development of one finger branch are analyzed by PIVlab. The length of one square interrogation window is 32 pixels and the space interval of interrogation windows is 16 pixels. The ratio between the interrogation window and the grain size is 4.63. The time interval between two pictures are 0.4 s. For any two consecutive pictures, the velocity vectors of each interrogation window can be extracted.

Figures 3.9 and 3.10 show the velocity vector plots and the velocity density plots for the finger tip propagation. The finger tip propagation process could be divided into the following stages:

1. (a) to (b): Extension of the finger is mainly in the length direction. The tip velocity in (a) is much larger than the rest of the domain. The finger expands only slightly in the transverse direction.

2. (c): The left part of the domain ceases to move. The right part moves in the horizontal direction to widen the whole finger.

3. (d) to (g): The finger propagation focuses on the tip area again. The tip behaves like a small cavity which is experiencing the radial expansion.

4. (h) to (i): After the cavity expands to a certain size, the finger tip starts to split and form a new tip. The new tip area has higher velocities than rest of the domain.

This finger propagation scenario also suggests the sequence of tip blunting prior to tip splitting as observed in Figure 3.7.

Figure 3.11 shows evolution of the maximum shear strain rate for the finger tip propagation. The shear strain rate is highly localized at the finger tip. Though no distinct long shear band can be identified from these images, the results in fact agree with the tip propagation scenarios in that initiation of a new tip may be of a few grain sizes only. As a result, such a localized shear band at the tip may be below the resolution of this analysis.

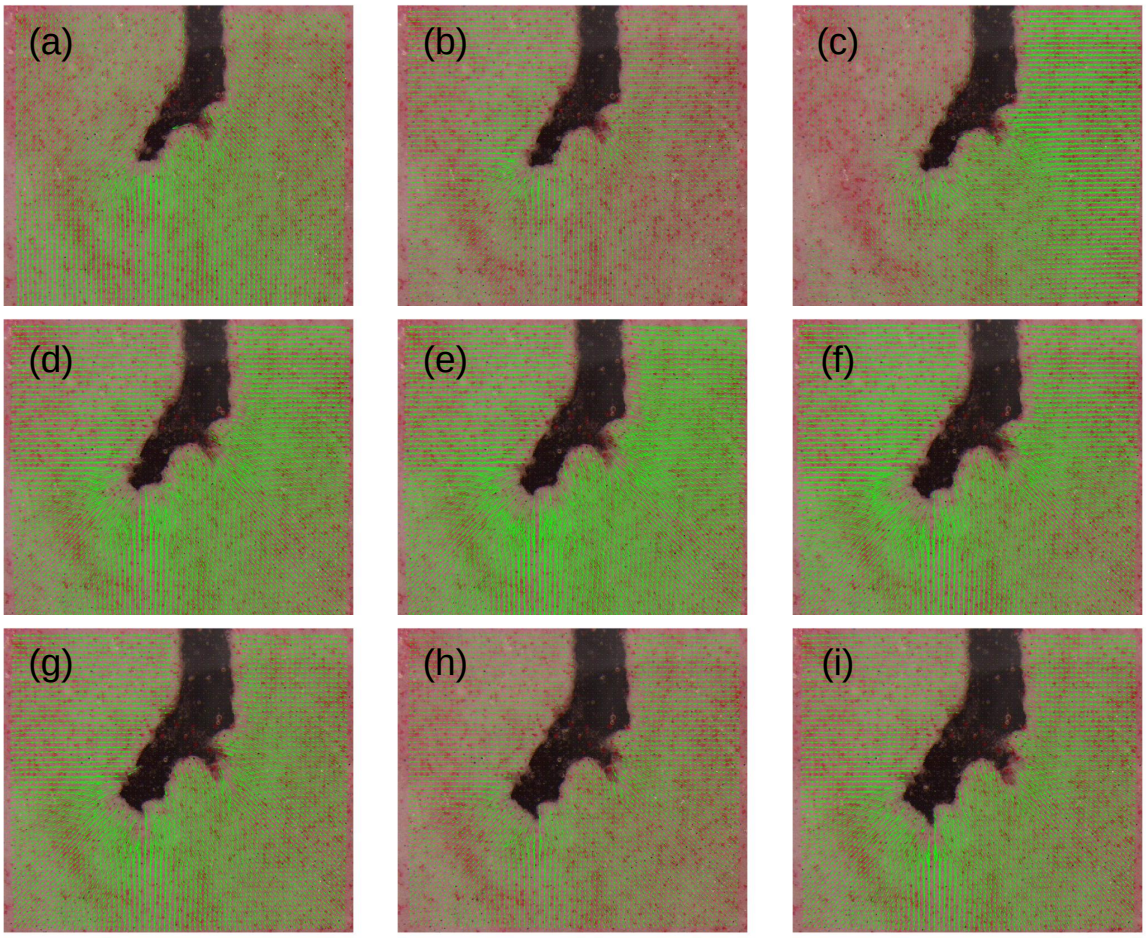

Figure 3.9: Velocity vector field from PIV analysis for the finger propagation.

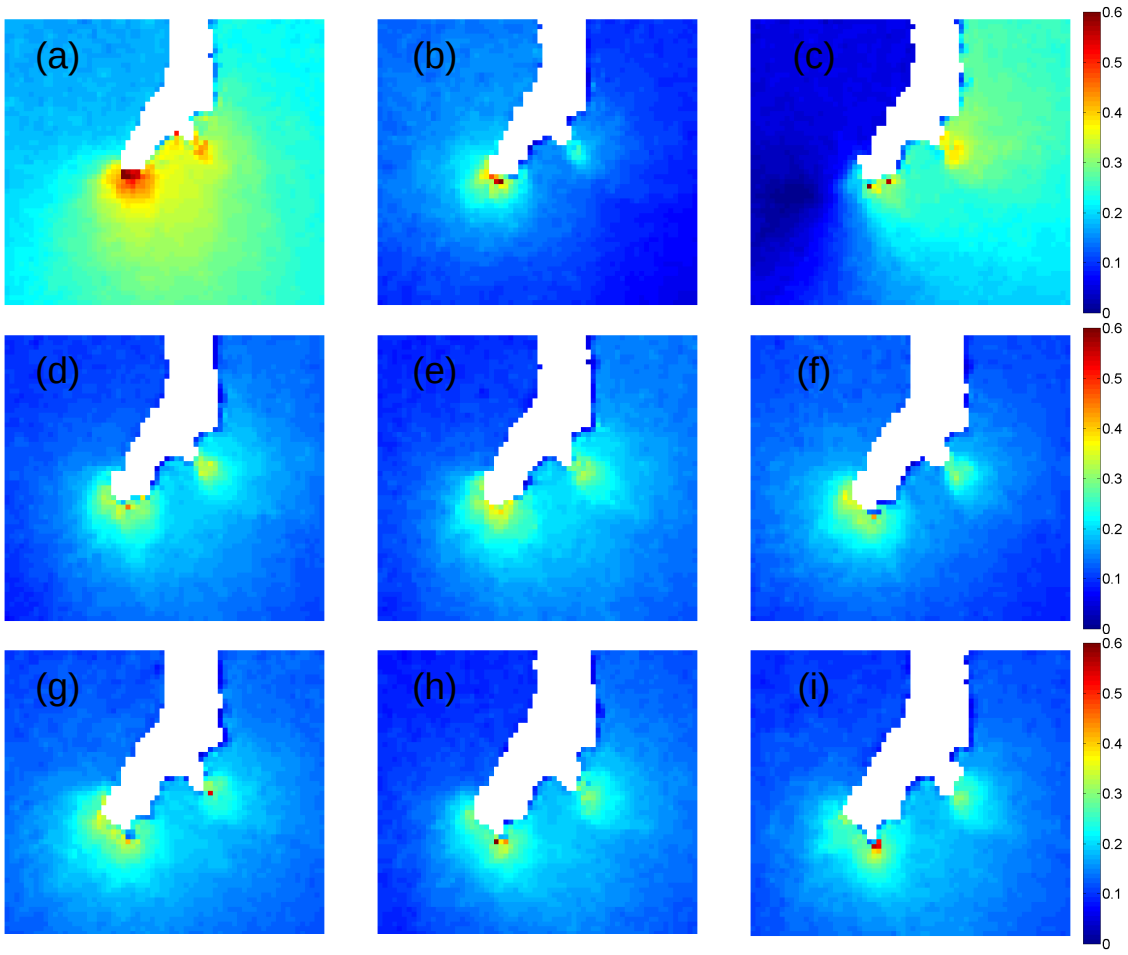

Figure 3.10: Density plot of the velocity field.

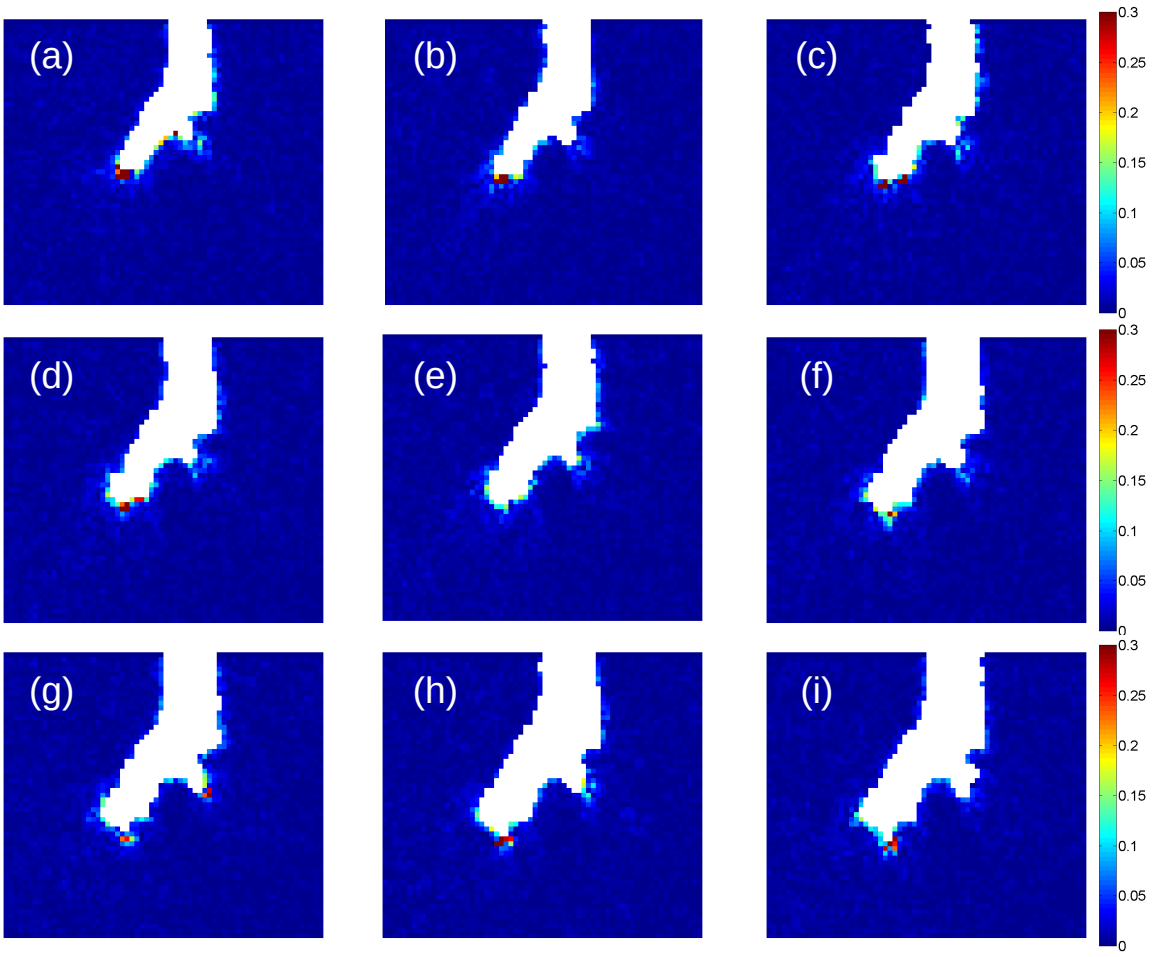

Figure 3.11: Maximum shear strain rate for the finger propagation.

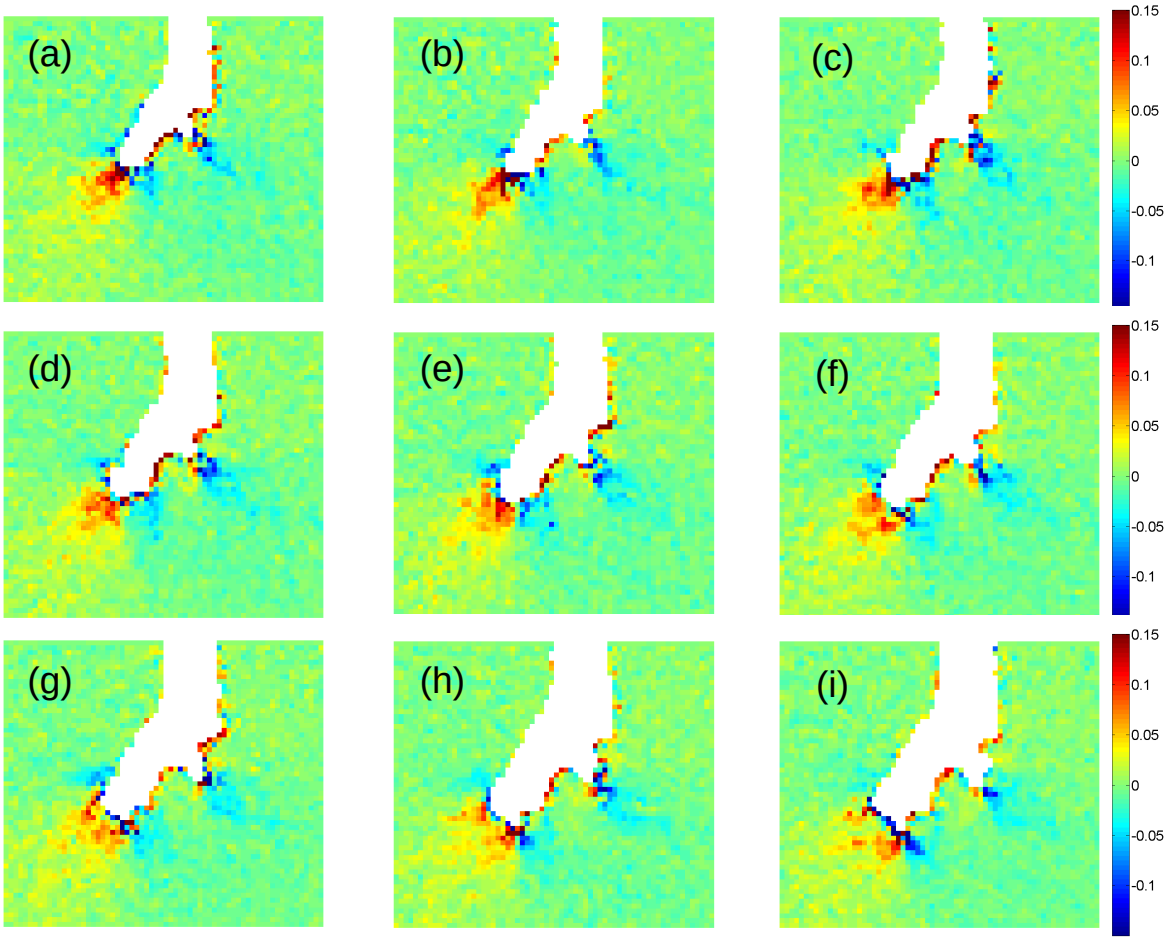

Figure 3.12: Volumetric strain rate for the finger propagation.

Evolution of the volumetric strain in Figure 3.12 shows intriguing features which in fact resemble fracture propagation in a cohesive and frictional material. The results indicate that the area ahead of the tip seems to dilate, possibly due to fluid pressurization while the granular media seem to be in compaction on the side of the fingers.

The results reported here are still preliminary since uncertainty exists in determining the granular finger perimeter. Though the granular fingers are masked in the calculation, fine details may be lost near the finger tip, especially for the quantities that exhibit large spatial gradients such as the maximum shear strain rate and the volumetric strain rate.

3.5 Conclusions

In this chapter, the displacement regimes for the injection process in the Hele-Shaw cell are classified based on the considerations of three characteristic times: the injection time, the diffusion time that characterizes the hydromechanical coupling and the retardation time that describes the viscoelastoplatic response of the granular media. Two dimensionless times can be defined to classify the displacement regimes. The threshold values that define the transitions between the displacement regimes can be determined from the variations of the global features such as the area ratio λ and the fractal dimensions of the finger and infiltration areas as functions of the dimensionless time τ_1.

The finger tip behavior is analyzed based on the images taken directly from the experiments and by using Particle Image Velocimetry technique. The evolution of the velocity field shows that the finger propagation has the sequence of tip blunting and splitting. The newly developed tip is at an angle of 45° with respect to the main branch, an indication that the tip propagates as a result of shear failure. The PIV results indicate that the shear strain rates are highly localized near the tip. Ahead of the finger tip, the material dilates while the material on the sides of the granular fingers compacts.

Chapter IV

DEM/CFD COUPLING ANALYSIS

4.1 Introduction

In this chapter, failure induced by fluid pressurization in a cylindrical wellbore in purely frictional media is investigated numerically using the discrete element method (DEM) code $PFC3D^{®}$ [Itasca Consulting Group, 2008] with the Coupled Computational Fluid Dynamics ($CCFD$) add-on option [ITOCHU Technology Solution Corporation, 2008]. For competent rocks, fluid pressurization in a cylindrical wellbore has been studied within the framework of poroelasticity and linear elastic fracture mechanics [Detournay and Cheng, 1988, Garagash and Detournay, 1997]. Meanwhile, wellbore expansion due to mechanical loading in granular media has been analyzed through elasto-plasticity models such as the cavity expansion models [Huang and Detournay, 2010] or via the bifurcation theory [Alsiny et al., 1992]. Theoretical models are yet to be developed for wellbore expansion in dense granular media when the loading mechanism is due to fluid injection.

DEM-CFD coupled fixed coarse grid schemes have been previously applied to investigate problems such as flow induced structures in a fluidized bed [Tsuji et al., 1993, Xu and Yu, 1997, Tsuji, 2007]. However, the shape of the fluid elements in those studies can only be rectilinear. In this work, the option of the hexahedral fluid element in the $CCFD$ scheme allows us to construct the domain in a cylindrical shape. A hollow cylindrical domain is employed in this work. The effects of fluid viscosity and the injection velocity on the failure mechanisms are examined.

4.2 Methodology

4.2.1 DEM-CFD coupling

The novelty in this numerical analysis is the use of the DEM-CFD coupling technique. In this technique, the mechanical deformation of the granular media is modeled using

the DEM code $PFC3D^{®}$ while fluid flow is modeled using the $CCFD$ add-on option. Coupling is initiated from a pre-processor GiD [International Center for Numerical Methods in Engineering (CIMNE), 2008]. GiD starts $CCFD$, $PFC3D^{®}$ and a proxy server which facilitates the data communications between $CCFD$ and $PFC3D^{®}$ at predetermined times. In this analysis, the critical time step required for stable mechanical calculation is much smaller than that in the fluid calculation. To reduce the computational cost, each coupling data exchange occurs only after certain cycles of mechanical calculation. Meanwhile, to properly resolve the coupling behavior, the data exchange intervals are chosen to be small enough to ensure that the exchange occurs several times as a particle moves across a fluid element.

The incompressible Navier-Stokes equation, modified to include the local porosity and a body force term to reflect the existence of the particles, is solved in $CCFD$,

$$\rho_f \frac{\partial(\phi\vec{v})}{\partial t} + \rho_f \vec{v} \cdot \bigtriangledown(\phi\vec{v}) = - \bigtriangledown p + \eta_f \bigtriangledown^2 (\phi\vec{v}) + \vec{f_d} \tag{4.1}$$

where $\vec{f_d}$ is the body force term; ϕ is the porosity of the fluid element; $\vec{v}$ is the fluid velocity; ρ_f is the fluid density; η_f is the fluid viscosity and p is the fluid pressure.

The body force term $\vec{f_d}$ in Eq. (4.1) accounts for the drag forces on the particles averaged over the volume of the fluid element. In the mechanical calculation, the unbalanced forces therefore have contributions from not only the contact forces (and possibly externally applied forces) but also the drag forces.

In this analysis, fluid flow is assumed to be in the laminar regime, i.e., no turbulent flow (though the turbulent flow option is available in $CCFD$). In the coupling scheme, the inertia effect in the laminar regime is reflected in the drag coefficient C_d for a single particle (without the consideration on the effect of particle concentration) [ITOCHU Technology Solution Corporation, 2008],

$$C_d = \left(0.63 + \frac{4.8}{\sqrt{Re_p}}\right)^2 \tag{4.2}$$

where Re_p is the particle Reynolds number defined by using the particle diameter d_p, fluid density ρ_f, fluid viscosity η_f and the slip velocity V between the fluid and

the particle, i.e. $Re_p = \rho_f V d_p/\eta_f$. Note that for Stokes' flow, i.e., the creeping flow regime at $Re_p \ll 1$, the drag coefficient is $C_d = 24/Re_p$. The corresponding drag force f_0 for a single particle can be expressed as

$$f_0 = \frac{\pi \rho_f V^2 d_p^2}{8} C_d \tag{4.3}$$

The effect of porosity (or the particle concentration) on the drag force is taken into account through,

$$f_{drag} = f_0 \phi^{-\chi} \tag{4.4}$$

where f_{drag} is the corrected drag force for one particle and χ is an empirical coefficient defined as,

$$\chi = 3.7 - 0.65 \exp\left[-\frac{(1.5 - \log Re_p)^2}{2}\right] \tag{4.5}$$

The drag force formulated in Eqs. (4.3), (4.4) and (4.5) is applicable for both fixed and fluidized beds for a large range of Reynolds number [de Felice, 1994]. It should be noted since field variables are locally averaged in the fluid calculation, for this type of coupling scheme, the flow structure resolved is at the scale of the fluid element, not at the pore scale.

4.2.2 Flowchart of the coupling cycle

A detailed coupling cycle is shown in the flowchart in Figure 4.1. The $PFC/CCFD$ coupling is implemented by exchanging data between PFC and $CCFD$ at prescribed time steps. After the coupling starts, PFC receives data from $CCFD$, including the fluid viscosity, density, velocity and pressure. Drag forces are then calculated and applied to the particles in the mechanical calculation. After the mechanical calculation, PFC sends the updated porosity and drag force for each fluid cell to $CCFD$ to modify the terms in the Navier-Stokes equations. $CCFD$ then proceeds to another time step t_e and starts another coupling cycle. Since fluid compressibility is not taken into account in this scheme, such coupling is only one-way in the sense of Biot [Biot, 1941].

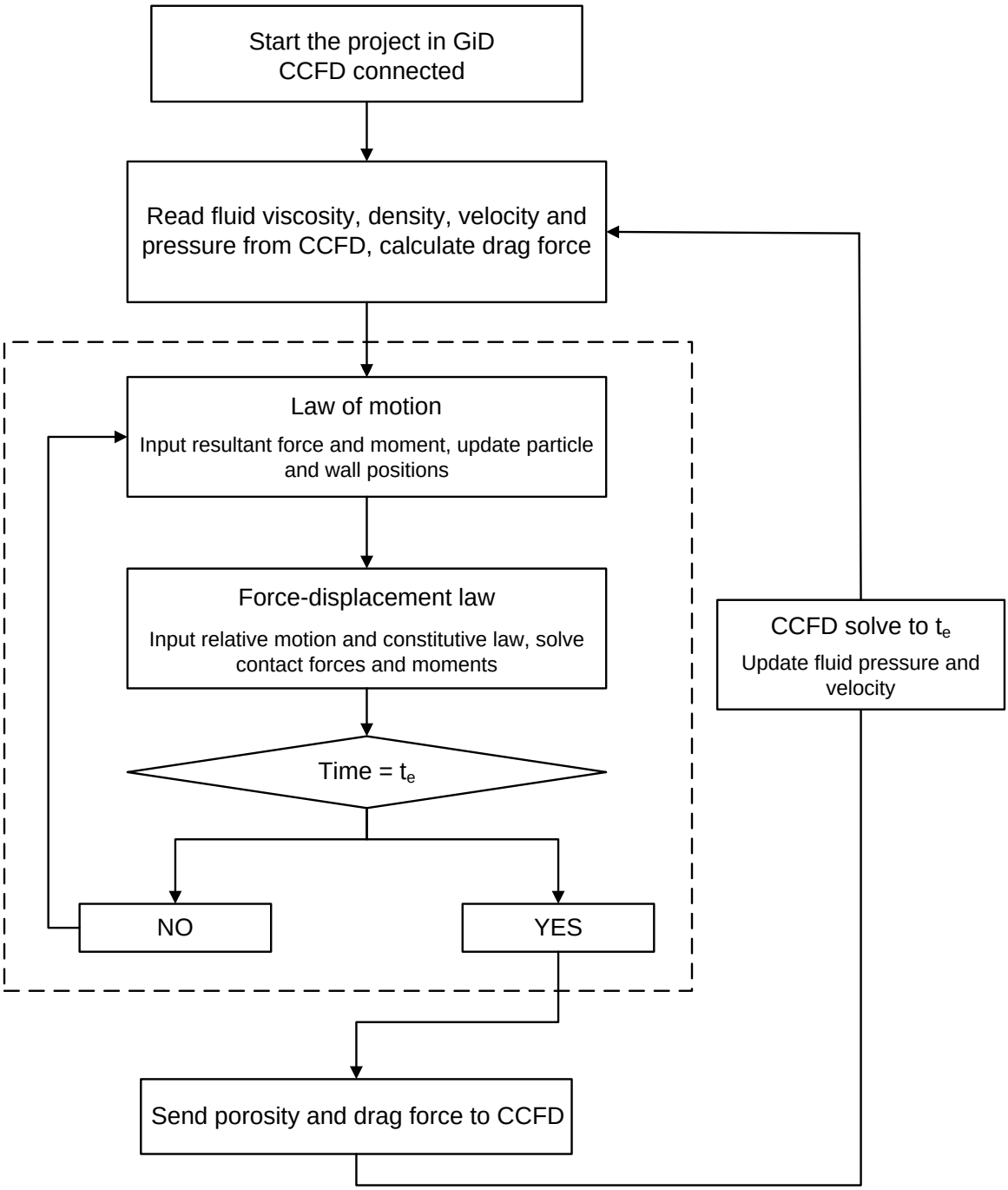

Figure 4.1: $PFC/CCFD$ coupling scheme.

4.2.3 Numerical model setup

The numerical analysis is carried out in a hollow cylindrical slab domain. The borehole diameter is $d_i = 30$ mm and the domain diameter is $d_o = 200$ mm. The thickness of the domain is $\delta = 5$ mm. The top and bottom boundaries are confined by two fixed walls. The simulations start from an initial isotropic stress state with $\sigma_0 = 0.1$ MPa. During the simulations, the far field mechanical stress is maintained constant at $\sigma_0 = 0.1$ MPa through a servo-controlled cylindrical wall. The confining stress acts as the effective stress to the particle assembly. The numerical domain is filled with 30405 randomly generated spherical particles of three different sizes, as can be seen in Figure 4.2. The radius of the particles near the wellbore in light orange is $r_1 = 0.6$ mm. The radii of the green and blue colored particles are $r_2 = 0.8$ mm and $r_3 = 1$ mm, respectively. The reason to use three species of particles in this analysis is to achieve a balance between the necessary resolution near the wellbore and the computational cost. The initial porosity of the near wellbore region is $\phi = 0.40$. The corresponding permeability is $k = 1.42 \times 10^{-9}$ m^2 according to the porosity-permeability correlation of Kozeny-Carman [Bear, 1988].

A linear contact model is employed to relate the contact forces and relative displacements through,

$$F_n = K_n U_n,\ F_s = -K_s \triangle U_s \tag{4.6}$$

where F_n and F_s are the normal and shear contact forces; K_n and K_s are the normal and shear contact stiffnesses; U_n and $\triangle U_s$ are the normal displacement and shear displacement increment.

The contacts between particles near the wellbore are characterized by the normal and shear stiffnesses $K_n = K_s = 10^5$ N/m. Throughout the domain, the ratios K_n/r and K_s/r are kept constant. All particles have a frictional coefficient $\mu = 0.577$ and density $\rho_p = 2650$ kg/m^3. All the walls are frictionless. Stiffnesses of the top and bottom walls are the same as those of the particles near the wellbore and the stiffnesses of the outer wall are the same as those of the particles in the far field.

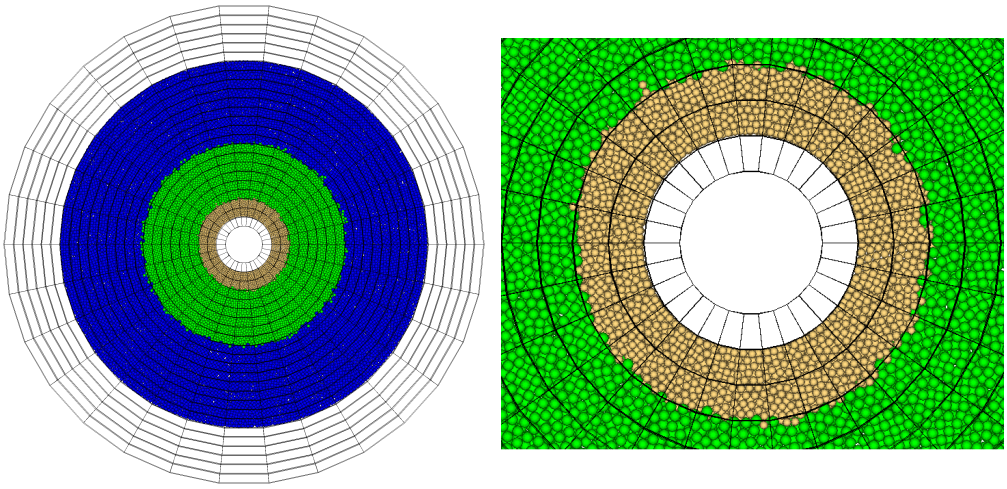

Figure 4.2: (a) Top view of the DEM-CFD numerical model; (b) the wellbore vicinity. Black lines show the fluid elements and the particle colors correspond to the three different particle sizes.

The fluid domain consists of 1440 mapped hexahedral fluid elements with 24 elements in the radial direction, 30 in the circumferential direction and 2 in the thickness direction. Each fluid element contains at least ten particles. In the fluid domain, there is one round of fluid elements at the inlet without particles, see the wellbore vicinity in Figure 4.2(b). The elements are placed there for the convenience of implementing of a constant superficial flow velocity condition at the inlet. In addition, several rounds of fluid elements are also created in the far field in order to accommodate the expansion of the particle assembly during the simulations. The far field fluid boundary is drained with the fluid pressure being set to zero. The numerical model described here is essentially pseudo-3D and corresponds to the case of injection in fully saturated media with the invading fluid and the pore fluid being the same. In the discussion below, the term "wellbore" refers to the inner boundary of the particle assembly, whereas the term "inlet" refers to the round of the fluid elements where the injection velocity is applied.

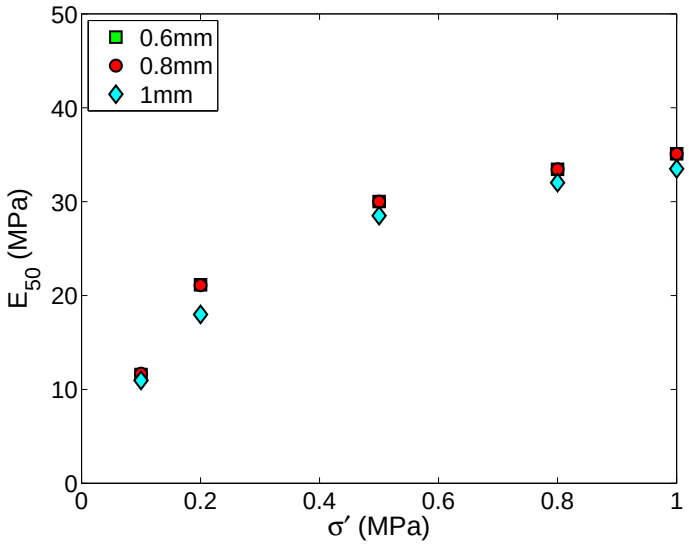

Figure 4.3: Variation of the elastic moduli of the particle assemblies, with $r = 0.6$ mm, 0.8 mm and 1 mm, as functions of the confining stress.

4.2.4 Material strength

The macro scale material strength parameters of three particle sizes, i.e. with radius $r_1 = 0.6$ mm, $r_2 = 0.8$ mm, and $r_3 = 1$ mm, are measured separately by triaxial tests under different confining stress from 0.1 MPa to 1 MPa. The triaxial specimen is cylindrical with an aspect ratio equal to 2. Since the strain-stress behaviors of the particle assembly are nonlinear, the elastic modulus and Poisson's ratio at the level of 50% peak stress are obtained as the index properties.

Figures 4.3, 4.4, and 4.5 plot the elastic modulus, Poisson's ratio and the peak friction angle of the three particle species at different confining stresses.

4.3 Effect of Injection Velocity

The effect of the injection velocity is explored by performing a series of fifteen simulations with the injection velocity V ranging from 0.5 m/s to 30 m/s. The fluid density and fluid viscosity is set as $\rho_f = 1000$ kg/m^3 and $\eta_f = 0.01$ Pa·s. Among the cases analyzed, the largest particle Reynolds number is $Re_p = 3600$ for $V = 30$ m/s, suggesting substantial inertia effect may be present in that case. Depending on the injection velocity, the responses of the particle assembly can be classified into three

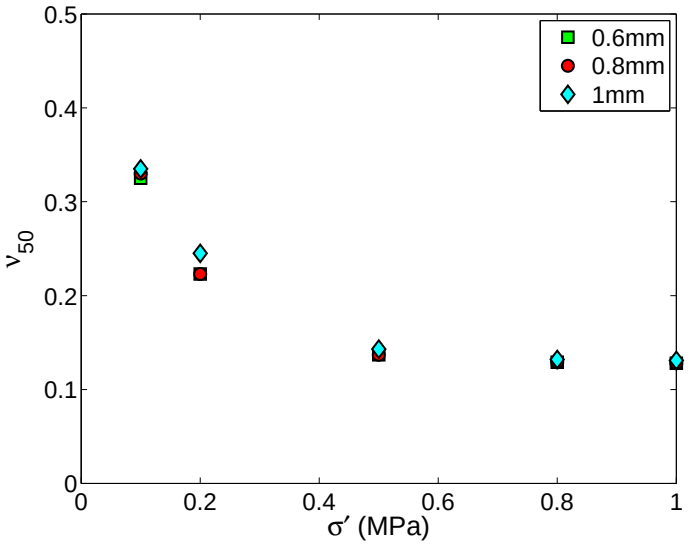

Figure 4.4: Variation of the Poisson's ratio of the particle assemblies, with $r = 0.6$ mm, 0.8 mm and 1 mm, as functions of the confining stress.

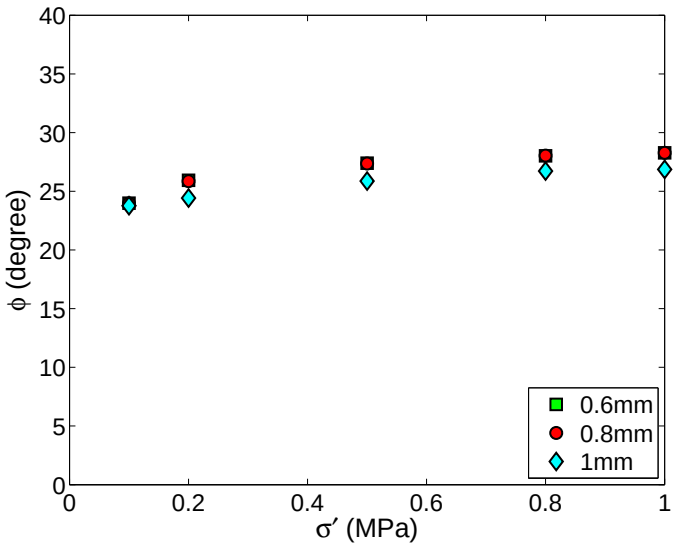

Figure 4.5: Variation of the peak friction angle of the particle assemblies, with $r = 0.6$ mm, 0.8 mm and 1 mm, as functions of the confining stress.

groups, namely, i) a fixed bed flow type of response at relatively low injection velocities, ii) localized failure at intermediate injection velocities, and iii) near wellbore fluidization at high injection velocities. Results from the four representative cases with $V = 1$, 3, 5 and 14 m/s are reported below.

4.3.1 Particle velocity field

Figure 4.6 plots the particle velocity field at the end of the injection process for the four representative cases. The post-processing procedure starts by discretizing the assembly domain using Delaunay triangulation based on the particle centroid positions. Particle velocity at each triangle element can be obtained by averaging the particle velocities at the three vertices. The density plots of the particle velocity field are obtained by filling each triangle with colors associated with its particle velocity value.

For the low injection velocity $V = 1$ m/s, magnitudes of the particle velocities, shown in the contour plot in Figure 4.6(a), are in the order of $O(10^{-3})$ of the injection velocity. The response of the particle assembly is similar to that in a fixed bed, where fluid simply permeates through the porous media and the particles in the domain remain nearly fixed.

For the intermediate injection velocity $V = 3$ m/s, in responding to fluid flow, the wellbore first expands nearly uniformly in the radial direction. The shape soon becomes distorted. As can be seen from the particle velocity field in Figure 4.6(b), a localized band of particles is moving at higher velocities than rest of the domain. Figure 4.7 shows the evolution of the particle velocity field for $V = 3$ m/s. It can be seen that a localized band of particles firstly appears in the right side of the domain then turns to the left side.

For the high injection velocity $V = 14$ m/s, the wellbore expands more or less uniformly, as shown in Figure 4.6(d). Nevertheless localized bands, much shorter than the ones in the case of $V = 3$ m/s, can be observed around the wellbore.

The case of $V = 5$ m/s appears to be in the transition from the localized failure behavior at intermediate injection velocities to the near uniform expanded wellbore

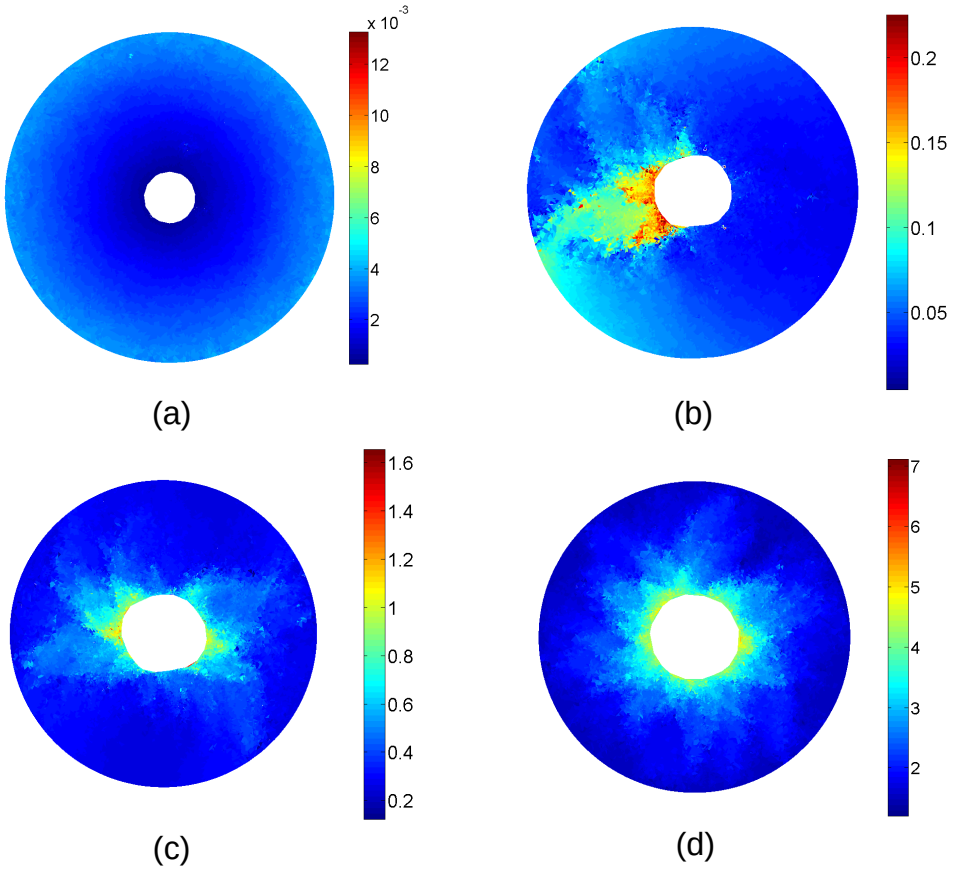

Figure 4.6: Particle velocity field for (a) $V = 1$ m/s at $t = 0.06$ s, (b) $V = 3$ m/s at $t = 0.04$ s, (c) $V = 5$ m/s at $t = 0.012$ s and (d) $V = 14$ m/s at $t = 0.003$ s. Unit in the color bar: m/s.

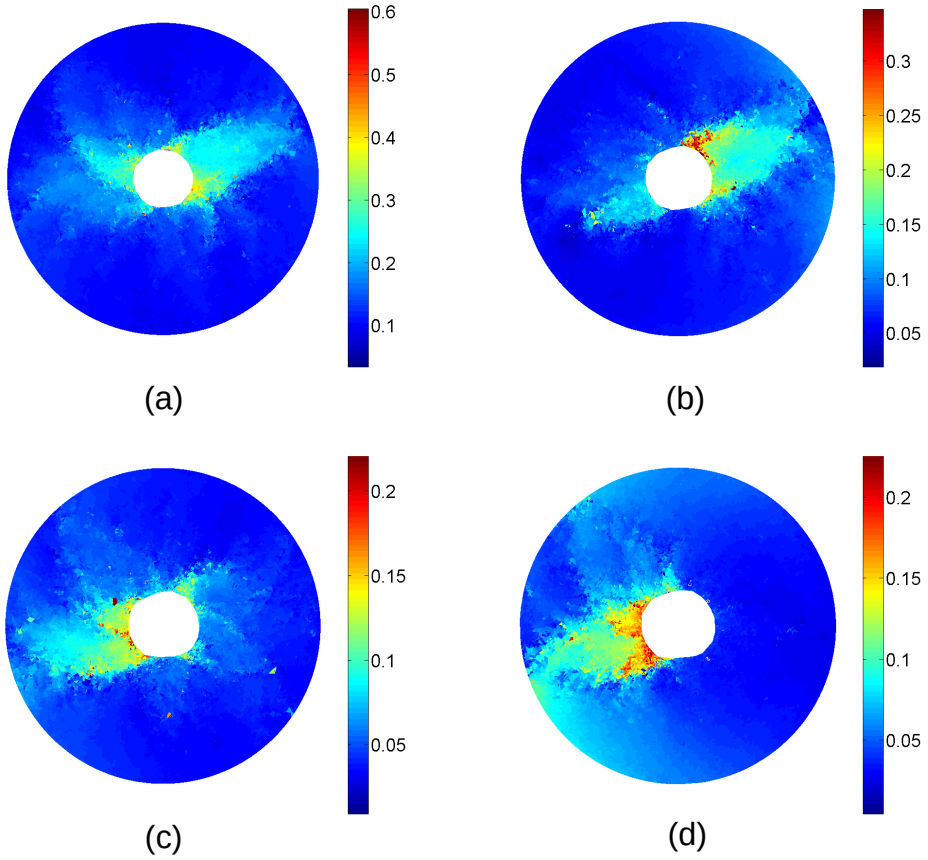

Figure 4.7: Particle velocity field at (a) $t = 0.01$ s, (b) $t = 0.02$ s, (c) $t = 0.03$ s and (d) $t = 0.04$ s for $V = 3$ m/s. Unit in the color bar: m/s.

behavior at high injection velocities.

4.3.2 Maximum shear strain rate

Figure 4.8 plots the maximum shear strain rate at the end of the injection process for the four representative cases. The maximum shear strain rate $\dot{\gamma}_{max}$ is determined from,

$$\dot{\gamma}_{max} = (\dot{\varepsilon}_1 - \dot{\varepsilon}_3)/2 \tag{4.7}$$

where $\dot{\varepsilon}_1$ and $\dot{\varepsilon}_3$ are the principal strain rates. To obtain the strain rate tensor, a preset measurement sphere matrix is laid out over the particle assembly. The measure sphere may be considered as equivalent to the representative elementary volume. The density plots of the strain rate field are then obtained from the discretized domain

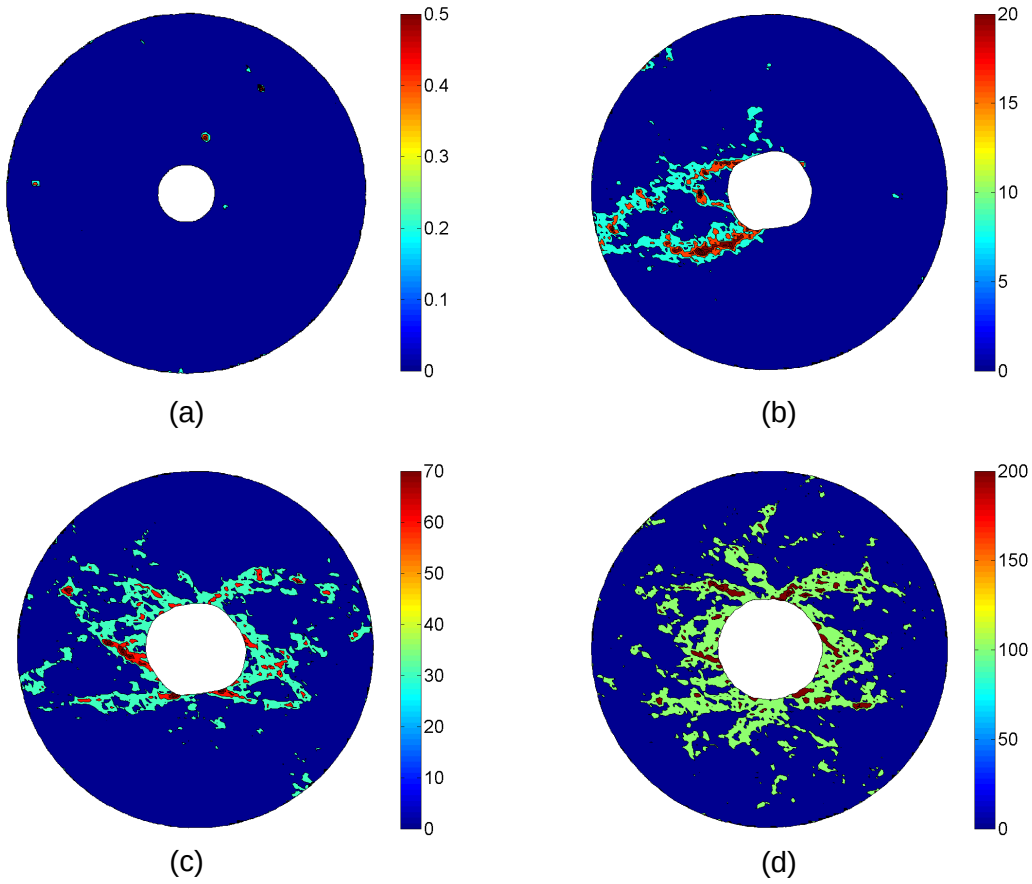

Figure 4.8: Maximum shear strain rate for (a) $V = 1$ m/s at $t = 0.06$ s, (b) $V = 3$ m/s at $t = 0.04$ s, (c) $V = 5$ m/s at $t = 0.012$ s and (d) $V = 14$ m/s at $t = 0.003$ s. Unit in the color bar: 1/s.

using Delaunay triangulation based on the measurement sphere centroid positions. The approach used here may be considered as equivalent to coarse graining.

For the low injection velocity $V = 1$ m/s, the maximum shear strain rate is nearly uniform in the whole domain with very small magnitudes. For the intermediate injection velocity $V = 3$ m/s, there are two long shear bands due to the localized moving band as shown in Figure 4.6(b). For a finite hollow cylindrical domain, full plastic failure may be described by the classical slip line theory [Hill, 1950], where the trajectories of the slip lines (or shear bands) are given by logarithmic spiral functions. Such a scenario of plastic failure seems to be consistent with the contour plot of the maximum shear strain rate in Figure 4.8(b). Figure 4.9 shows the evolution of the maximum shear strain rate at $V = 3$ m/s. The positions of the shear bands mark the

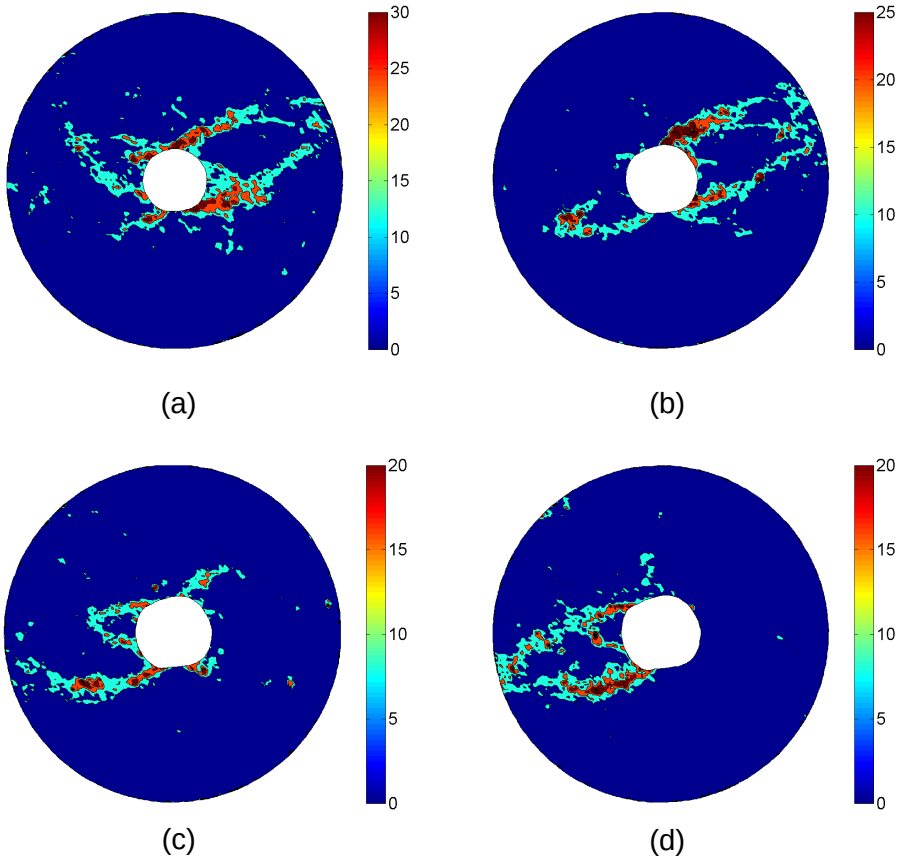

Figure 4.9: Maximum shear strain rate at (a) $t = 0.01$ s, (b) $t = 0.02$ s, (c) $t = 0.03$ s and (d) $t = 0.04$ s for $V = 3$ m/s. Unit in the color bar: 1/s.

boundary between the localized moving bands and the rest of the domain. At the early and later stages, there are always two long shear bands which become dominant because of the localized moving bands shown in Figure 4.6(b) and (d). For the high injection velocity $V = 14$ m/s, the shear deformation localizes not only in the shear bands extending from the wellbore to the outer boundary, but also in the patches of intensive shear zones near the wellbore region (see Figure 4.8(d)).

4.3.3 Assembly porosity field

Figure 4.10 plots the assembly porosity field at the end of the injection process for the four representative cases. The methodology to determine the porosity field is similar with the one used to determine the maximum shear strain rate. Evidences of shear-induced dilation and near wellbore fluidization can be observed in Figure 4.10.

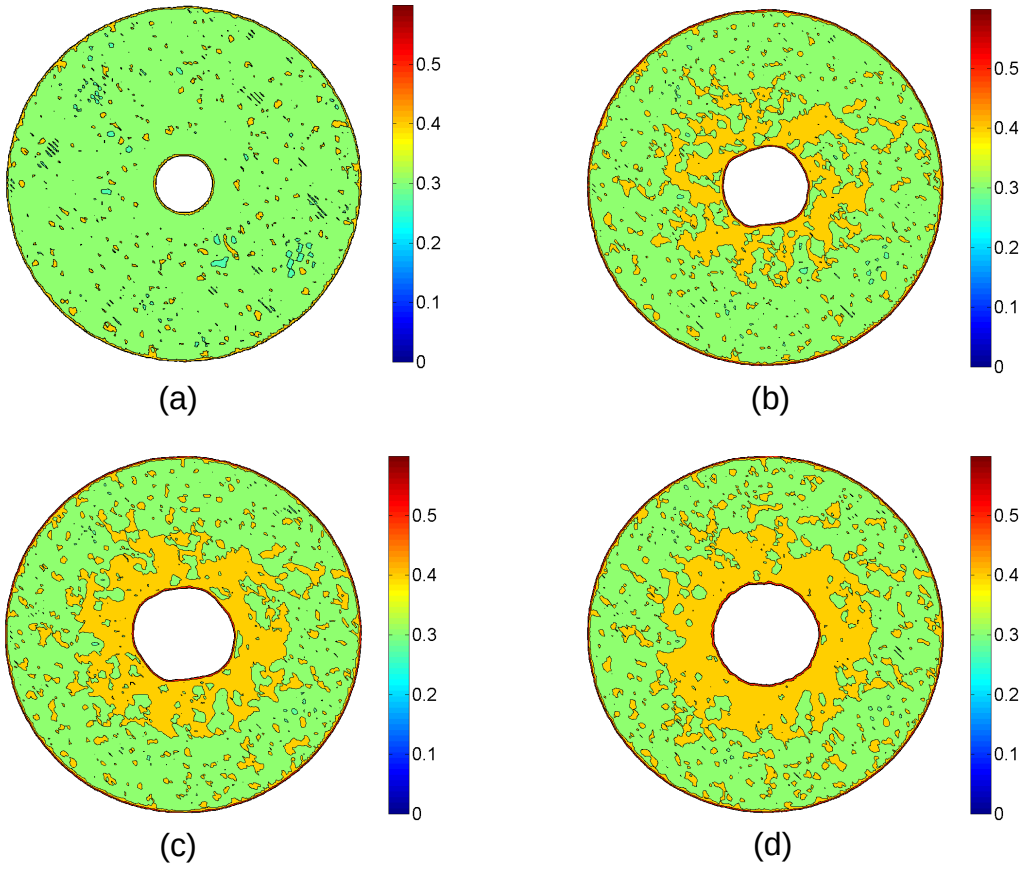

Figure 4.10: Assembly porosity field (a) $V = 1$ m/s at $t = 0.06$ s, (b) $V = 3$ m/s at $t = 0.04$ s, (c) $V = 5$ m/s at $t = 0.012$ s and (d) $V = 14$ m/s at $t = 0.003$ s.

4.3.4 Injection pressure history

Figure 4.11 shows the injection pressure history at the inlet for the four representative cases. As shown in Figure 4.11(a), the fixed bed flow type of behaviors can be deduced from the inlet pressure history for the low injection velocity $V = 1$ m/s. After an initial spike, associated with the sudden application of the velocity at the inlet, the inlet pressure remains nearly constant during the simulation time period, implying negligible change in the wellbore radius. For the intermediate injection velocity $V = 3$ m/s, after the spike, the pressure remains more or less constant initially, but declines after localization starts. Since in this simulation, the far field boundaries are subjected to a constant mechanical stress (or effective stress) and a constant fluid pressure, as the inlet pressure decreases to a threshold value, it is expected that a state of static equilibrium can be re-established. As a result, the inlet pressure tends to level off at late time as shown in Figure 4.11(d).

4.3.5 Wellbore evolution

By tracking the centroids of the particles at the cavity wall, evolution of the wellbore geometry in terms of shape and the rate of wellbore expansion can also be analyzed, see Figure 4.12. For low injection velocity $V = 1$ m/s, the wellbore remains circular and the rate of expansion is almost negligible. For the intermediate injection velocity, the wellbore expands uniformly prior to becoming distorted due to localization. For the large injection velocity, the wellbore experiences a uniform expansion although there are multiple short shear bands along the wellbore vicinity.

The wellbore profile can be approximated by a discrete Fourier series [Ehrlich and Weinberg, 1970],

$$R(\theta) = R_0 + \sum R_n \cos(n\theta - \varphi_n) \tag{4.8}$$

where θ is the polar angle; n is the harmonic order; R_0 is the average wellbore radius; R_n is the nth harmonic amplitude and φ_n is the phase angle. At $V = 3$ m/s, the largest amplitude is at the harmonic $n = 2$, which suggests that the wellbore shape is an elliptic shape. At $V = 1$ m/s, all the harmonics have very low amplitude which

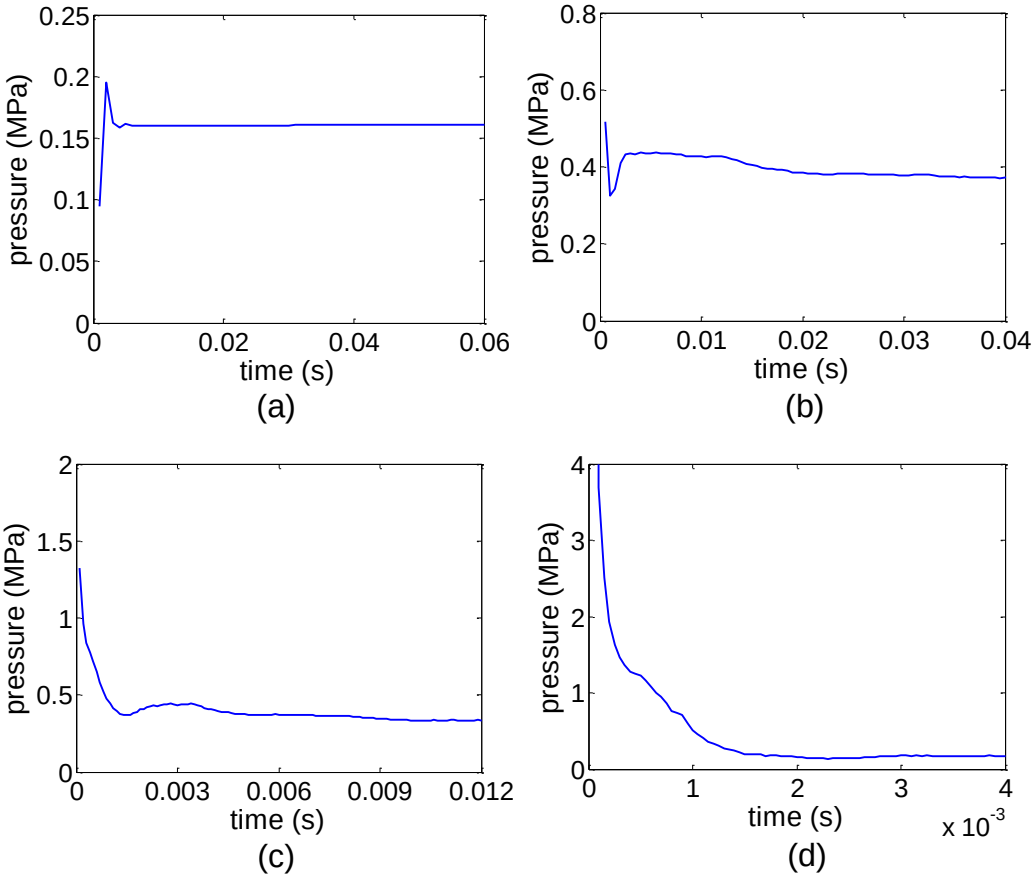

Figure 4.11: Wellbore pressure history for (a) $V = 1$ m/s, (b) $V = 3$ m/s, (c) $V = 5$ m/s and (d) $V = 14$ m/s.

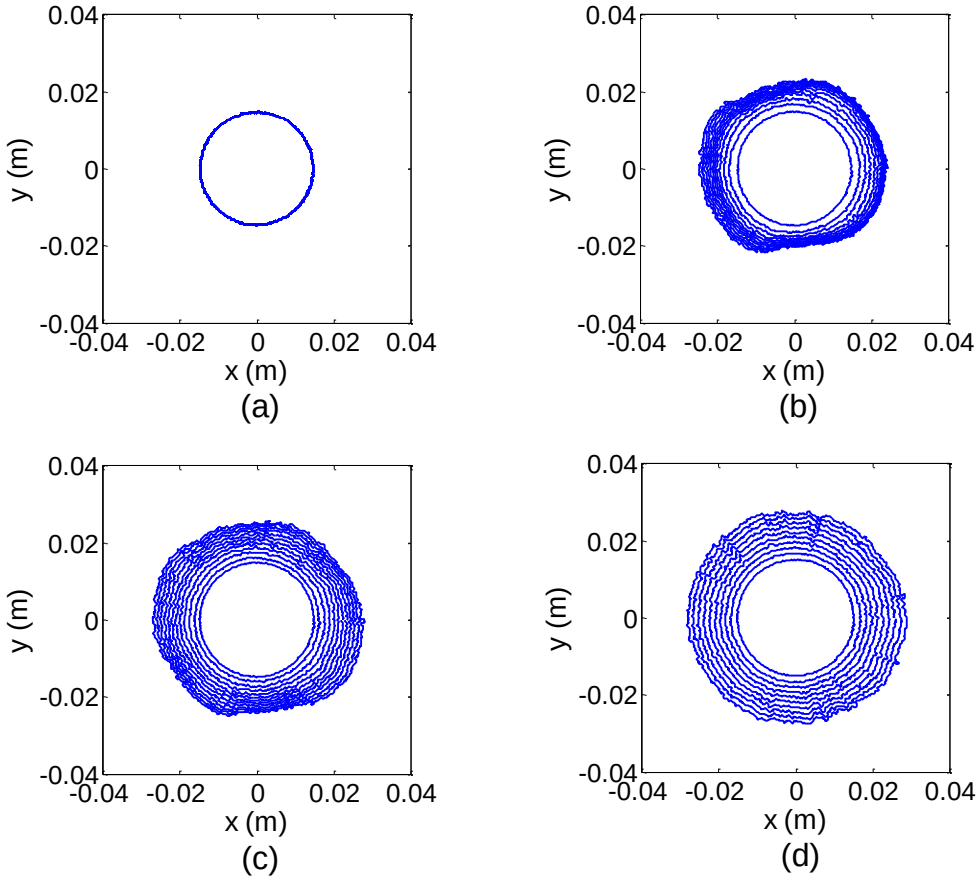

Figure 4.12: Evolution of the wellbore profiles for (a) $V = 1$ m/s, (b) $V = 3$ m/s, (c) $V = 5$ m/s and (d) $V = 14$ m/s.

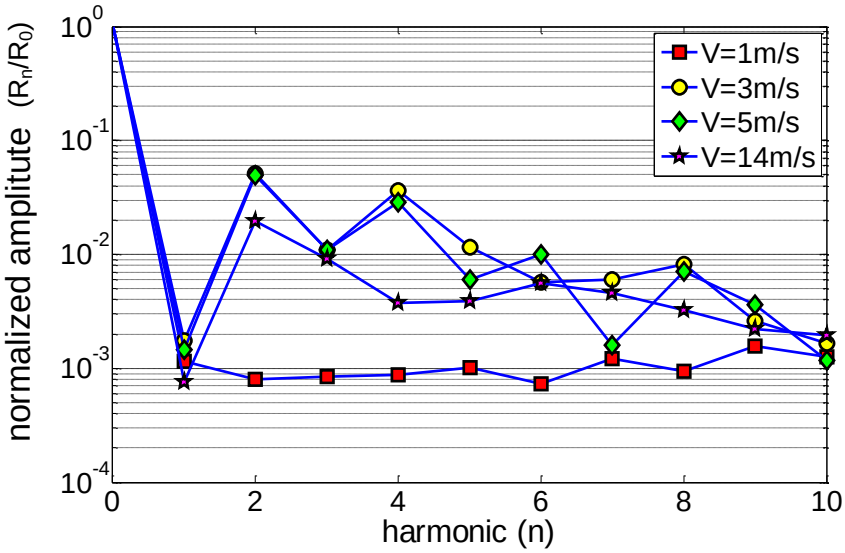

Figure 4.13: Normalized amplitude of the first ten harmonics for the four representative cases with $V = 1$, 3, 5 and 14 m/s.

means the wellbore shape is a perfect circle. At $V = 14$ m/s, although the largest amplitude is at the harmonic $n = 2$, but the amplitude is much lower than that of the intermediate injection velocity, which means the wellbore shape is only slightly distorted but remains close to a circle.

4.3.6 Critical injection velocity

In order to identify whether there is a critical injection velocity at which the granular media response deviates from that of a fixed bed, a normalized wellbore expansion rate ζ is defined for each simulation case, i.e.,

$$\zeta = \frac{dR_0/dt}{V} \tag{4.9}$$

where dR_0/dt is the rate of increase for the wellbore radius and V is the injection velocity.

As can be seen from the evolution of the wellbore profiles in Figure 4.12, for a given velocity, the wellbore expansion rate is not constant. In fact, it decreases with time. We therefore average the expansion rates within the time range of $2d_i/V$ so that the normalized rate ζ can be representative.

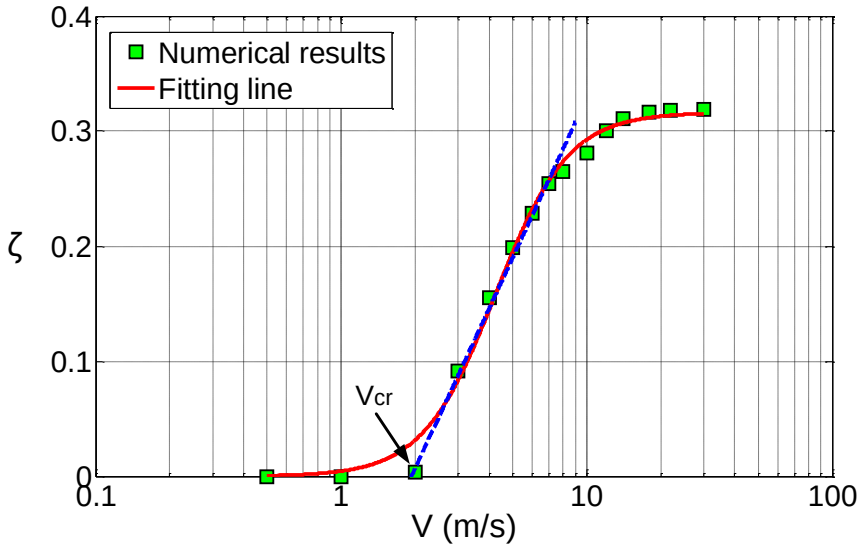

Figure 4.14: Normalized average wellbore expansion rate ζ vs. the injection velocity V for $\eta_f = 0.01$ Pa·s; the solid line is fitted based on all the data from the simulations while the dashed blue line is a linear fit for the data in the intermediate range.

The three scenarios of granular media behaviors are also reflected in the variation of the normalized wellbore expansion rate ζ with the injection velocity, as shown in Figure 4.14. When the injection velocity is relatively small and the response of the particle assembly is similar to that of a fixed bed, the normalized expansion rate is virtually zero. When the injection velocity is relatively large ($V > 10$ m/s) and the near wellbore region is fluidized, the normalized expansion rate is more or less constant, implying that the rate of wellbore expansion is roughly proportional to the injection velocity. In the intermediate velocity range when movement of the particles is localized, the normalized expansion rate increases almost linearly with the injection velocity. The relationship between the expansion rate ζ and the injection velocity V can be fitted by the following function,

$$\zeta = \frac{a}{1 + (bV)^c} \tag{4.10}$$

where $a = 0.3163$; $b = 0.2353$ and $c = -2.926$. The fitting function is plotted as the solid line in Figure 4.14.

If we fit the numerical results in the intermediate range in Figure 4.14 by a linear

equation, we may define the intercept on the horizontal axis as the critical injection velocity. In this series of simulations, $V_{cr} = 1.945$ m/s. This critical velocity can be interpreted as a measure for the transition from flow in a fixed bed type of behaviors to the localized failure scenario. Similarly, the transition from the localized failure to the fluidization scenario can also be defined through a critical velocity at which the linear fitting equation intercepts the plateau of the normalized expansion rate.

4.4 Effect of Fluid Viscosity

To investigate the effect of fluid viscosity, multiple series of simulations with different fluid viscosities have been carried out. For each viscosity, the critical injection velocity can be obtained from a plot similar to Figure 4.14. Figure 4.15 plots the critical injection velocities as a function of fluid viscosities (log scale) ranging from $\eta_f = 10^{-6}$ Pa·s to $\eta_f = 1$ Pa·s. The curves in Figure 4.15 suggests the existence of two different flow regimes: inertia-dominated regime when the fluid viscosity is low and viscosity-dominated regime when the fluid viscosity is high. In the inertia-dominated regime, the effect of viscosity is negligible and the critical injection velocity is nearly constant. In the viscosity-dominated regime, the critical injection velocity is nearly inversely proportional to the viscosity. The different fluid flow behavior could also be reflected by the magnitude Reynolds number: the Reynolds is large for the inertia-dominated regime and small for the viscosity-dominated regime.

4.5 Effect of Mesh Density

The DEM/CFD coupling technique in this work can only resolve fluid flow at the scale of the fluid element since all the particles inside one fluid cell share the same fluid properties. Rigorously speaking, the coupling scheme is mesh dependent. The results depend not only the fluid mesh density but also the ratio between the fluid element size and the particle radius.

To explore the effect of mesh density, results from two additional mesh configurations as shown in Figure 4.16 are compared with those from the baseline mesh configuration (24 elements in the radial direction, 30 in the circumferential direction

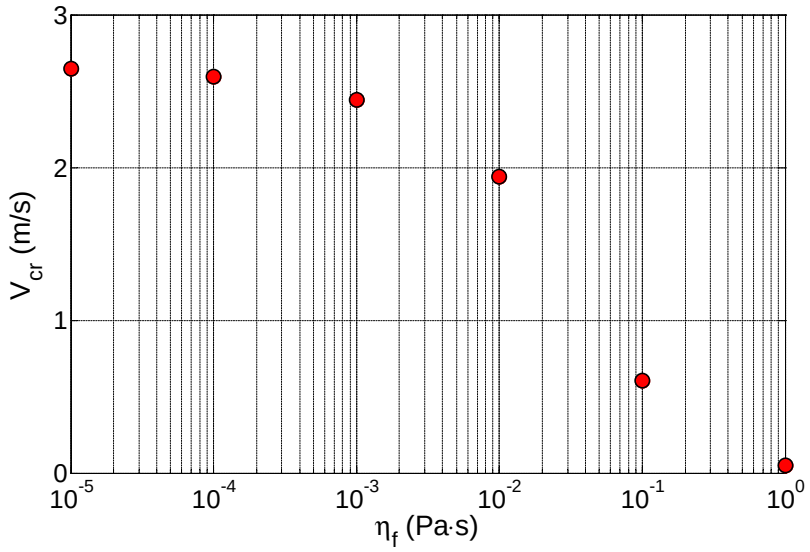

Figure 4.15: Critical injection velocity as a function of fluid viscosity (semi-log scale).

and 2 in the thickness direction). The coarse mesh configuration decreases the number of fluid elements in the circumferential direction from 30 to 24 and the dense mesh configuration increases the number of fluid elements in the circumferential direction from 30 to 36. The total numbers of fluid elements for the coarse and dense mesh configurations are 1152 and 1728, respectively, compared with 1440 for the baseline setup.

The coarse and dense mesh configurations are used to rerun the two tests of intermediate injection velocity $V = 3$ m/s and high injection velocity $V = 14$ m/s with the fluid viscosity $\eta_f = 0.01$ Pa·s. Evolution of the wellbore profiles for the injection velocity $V = 3$ m/s and $V = 14$ m/s are shown in Figure 4.17 and 4.18. The three wellbore profiles from the three cases show only slight discrepancy during the later stage for both $V = 3$ m/s and $V = 14$ m/s.

Figure 4.19 and 4.20 show the wellbore pressure histories for $V = 3$ m/s and $V = 14$ m/s for the coarse and dense mesh configurations. Again the results from all the three cases indicate excellent agreement. We may conclude that the effect of mesh dependency is negligible in our simulations.

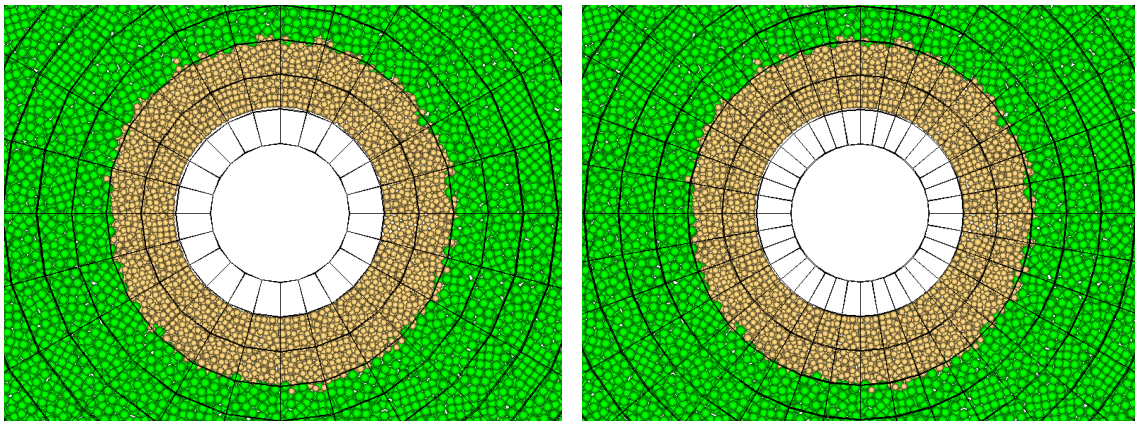

Figure 4.16: The wellbore vicinity view for (a) coarse mesh configuration; (b) dense mesh configuration.

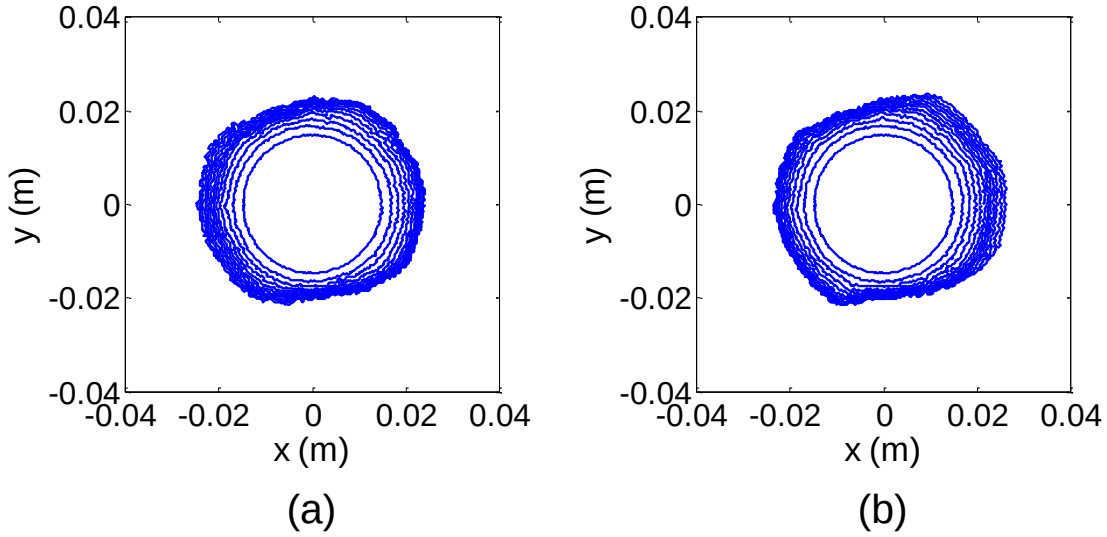

Figure 4.17: Evolution of the wellbore profiles when $V = 3$ m/s and $\eta_f = 0.01$ Pa·s for (a) coarse mesh configuration; (b) dense mesh configuration.

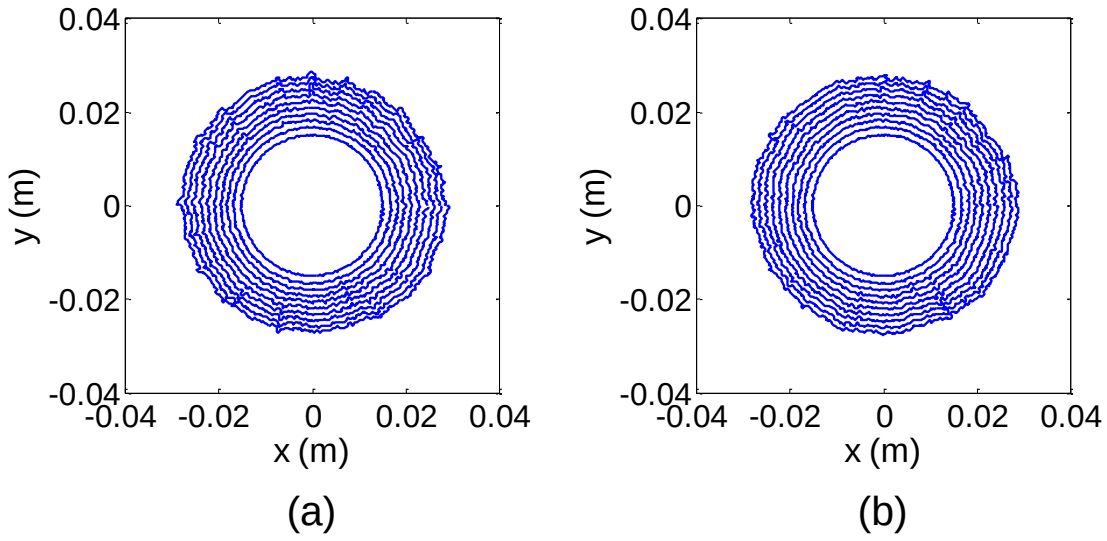

Figure 4.18: Evolution of the wellbore profiles when $V = 14$ m/s and $\eta_f = 0.01$ Pa·s for (a) coarse mesh configuration; (b) dense mesh configuration.

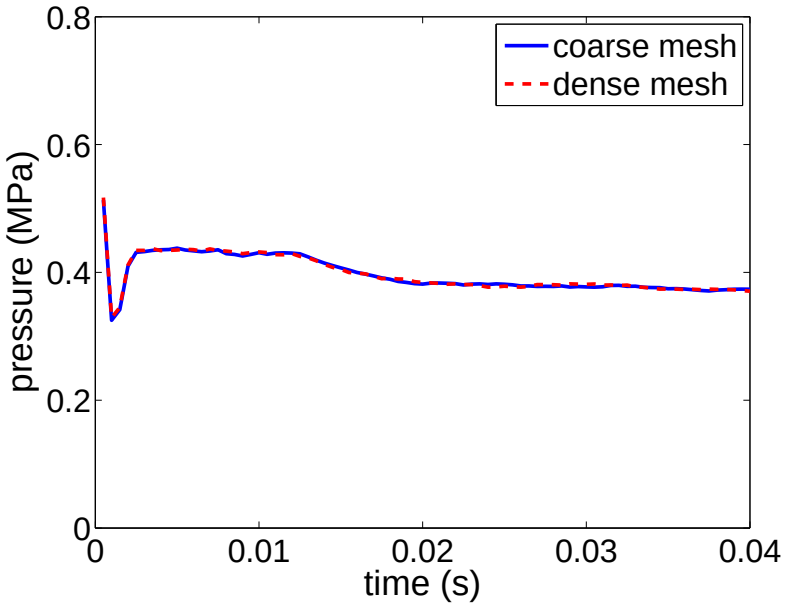

Figure 4.19: Wellbore pressure history when $V = 3$ m/s and $\eta_f = 0.01$ Pa·s for coarse mesh configuration and dense mesh configuration.

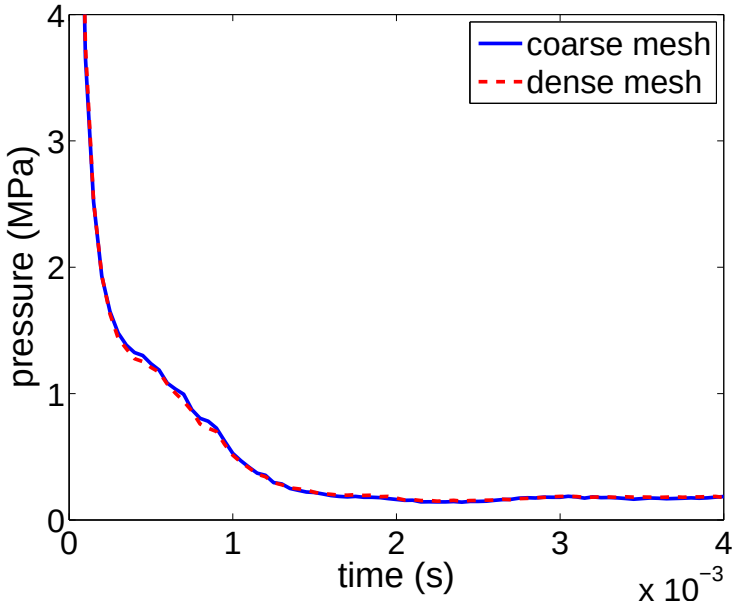

Figure 4.20: Evolution of the wellbore profiles when $V = 14$ m/s and $\eta_f = 0.01$ Pa·s for coarse mesh configuration and dense mesh configuration.

4.6 Discussion

The shear failure shown in the numerical simulations seems to agree with some of the experimental evidences in Bohloli and de Pater [2006]. We may speculate based on the numerical results that when the cylindrical domain is pressurized, initially the wellbore expands. Shear bands may develop from the wellbore. Since for dense granular media, the material dilates when sheared. The porosity inside the shear bands is higher than the porosity outside. The shear bands may therefore become the preferential flow paths for the fluid. For a finite hollow cylindrical domain, if a shear fracture was developed, the trajectory should be in a logarithmic spiral shape.

It should be noted however that many key aspects of the injection experiments in Chapter 2 are missing in the numerical simulations, for example, the displacement between the invading fluid and the fluid in the matrix. From the numerical modeling point of view, since the coupling technique used in this work can only resolve features at the scale of the fluid element, it has an inherent deficiency in modeling the lubrication flow in between particles. Nevertheless, such a coupling analysis has provided insights into the early time behavior of fluid injection. Alternative fluid flow schemes

such as the porescale network model can then provide a complementary view with its capability of modeling fluid flow at the pore scale.

4.7 Conclusions

In this work, failure induced by fluid pressurization in a cylindrical wellbore in purely frictional media is analyzed using the discrete element method code $PFC3D^{®}$ with the coupled computational fluid dynamics add-on option. The numerical model corresponds to the case of injection in fully saturated media with the injection fluid being the same as the pore fluid in the matrix. Main findings from this analysis can be summarized as follows.

Depending on the injection velocity, three types of responses can be identified for the behaviors of the particle assembly. When the flow velocity is relatively small, fluid simply permeates through the particle assembly and the response is similar to flow in a fixed bed. In the intermediate velocity range, the wellbore expands initially and then becomes distorted. Distortion of the wellbore leads to localized failure in form of shear bands. At large injection velocities, the wellbore experiences nearly uniform expansion and the near wellbore region is fluidized.

Critical velocities corresponding to the transitions from a fixed bed flow type of behavior, to localized failure, and to the fluidization scenario can be identified from the variation of the normalized wellbore expansion rate as a function of the injection velocity.

Variation of the critical velocity as a function of fluid viscosity indicates that when the fluid viscosity is small, the effect of viscosity is negligible and the critical injection velocity remains nearly constant. As the viscosity increases, the critical injection velocity becomes nearly inversely proportional to the viscosity when the viscosity becomes large.

The failure mechanisms observed in the numerical simulations show characteristics of the slip line field in classical plasticity theory. The shear band feature also resembles the shear fracture observed in the injection experiments a triaxial cell, e.g., Bohloli and de Pater [2006].

Chapter V

DEM/PORE NETWORK MODEL COUPLING ANALYSIS

5.1 Introduction

Numerical analysis using the DEM code $PFC2D^{®}$ coupled with a pore network model is conducted to model the fluid injection process in dense granular media. Modeling fluid flow in porous media with a pore network model has been widely implemented since 1950s [Fatt, 1956a,b,c]. In recent years, DEM coupled with the pore network model has been applied to investigate hydromechanically coupled problems [Cundall, Li and Holt, 2002, Li, 2002, Hazzard et al., 2002, GeoDelft, 2002, Al-Busaidi et al., 2005, de Pater and Dong, 2007, Zhao and Young, 2009, Damjanac et al., 2010] such as stress-dependent permeability and hydraulic fracturing induced microseismicity. Most of these studies deal with fully saturated conditions and bonded particles, where the solid skeleton is relatively stiff and the pore network structure does not need significant update during the simulations.

In this study, the injection process is modeled by implementing a pore network algorithm in $PFC2D^{®}$, which takes into account of the infiltration or pore filling process and updating the pore network to reflect the evolution of the particle structure. Effects of the injection flow rate, viscosity, permeability and assembly modulus on the failure/flow mechanisms are investigated. In addition, energy partition in the injection process is also analyzed.

5.2 Coupling Methodology

In this study, the coupled numerical simulations are performed in a two-dimensional hollow circular domain that consists of densely packed spherical particles. Fluid is injected at a constant velocity from the wellbore into an initially dry domain subjected to a constant far field stress. In the fluid flow scheme, the pore pressure and saturation are stored at the pore spaces or fluid domains enclosed by chains of particles

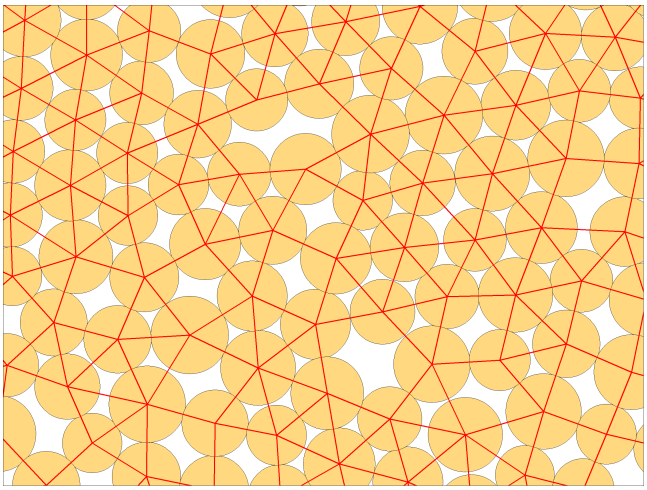

Figure 5.1: Schematic of the pore structure; red lines represent the fluid mesh and each triangle or polygon element forms a pore.

and contacts. Fluid flow between two adjacent pore spaces or domains takes place through the contacts according to the Hagen-Poiseuille equation with the width of the pore throats or flow paths determined by the openings between particles and the global permeability of the particle assembly. The coupling is realized by first solving the infiltration process at predetermined fluid time steps. The pressure gradients generated during the infiltration stage are then reflected in the drag forces exerted onto the particles in the subsequent mechanical calculation. After the particle positions are updated, the configuration of the pore structure is updated accordingly at every mechanical time step. A pore space can be splitted into two if a new contact is created in the fluid domain. Two pore spaces can also merge to form a new one if a contact in the fluid domain is deleted. A schematic of the particle assembly and the pore network is shown in Figure 5.1. The triangle or polygon elements enclosed by the red lines are the pore spaces. Note in this analysis the capillary effect is ignored. A flow chart for this DEM/pore network coupling scheme is shown in Figure 5.2.

5.2.1 Fluid flow model

Figure 5.3(a) shows the fluid flow model between two neighboring pores. The governing equation for slit flow, i.e., the Hagen–Poiseuille equation, is employed to describe flow in between the pore spaces,

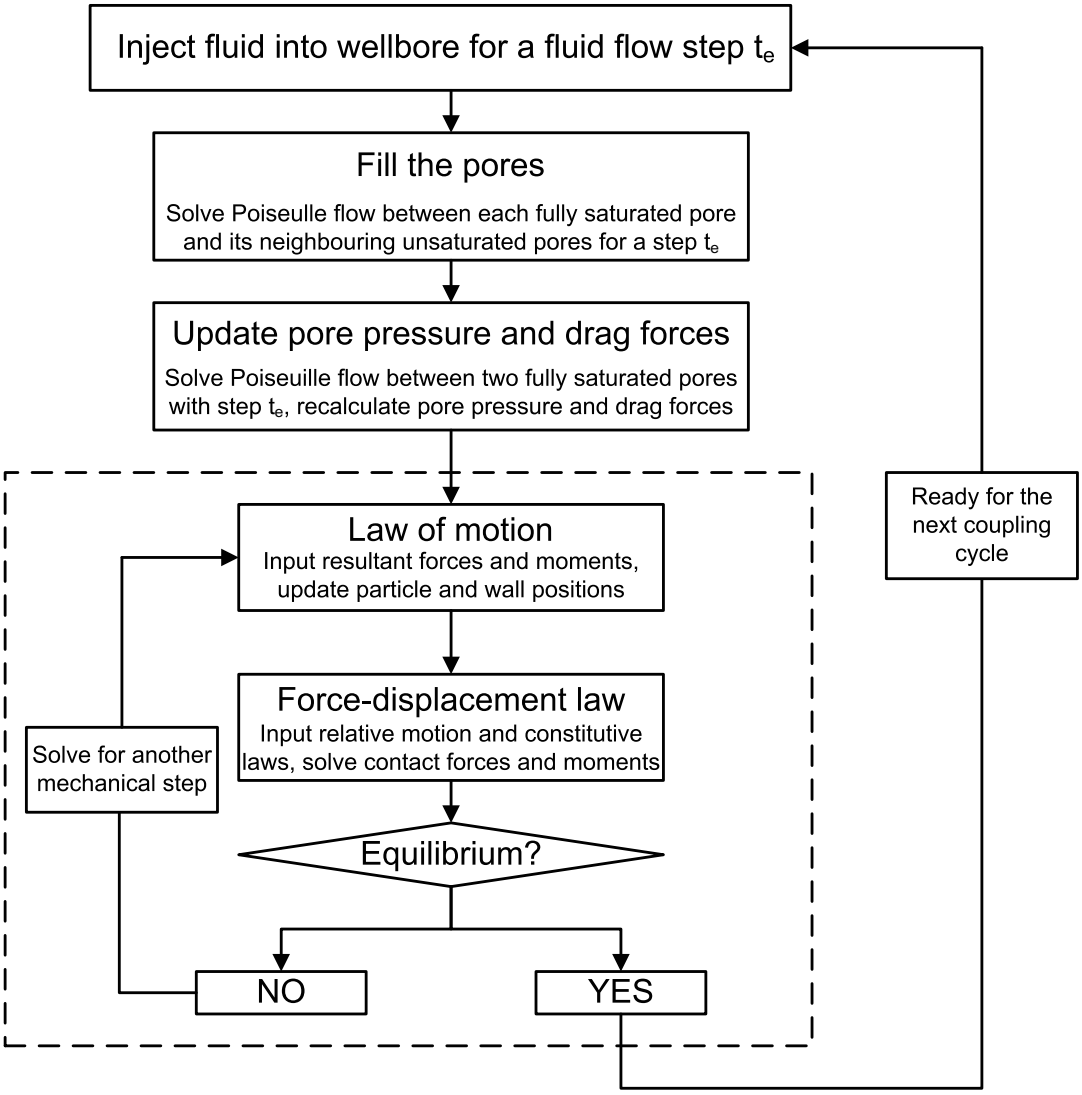

Figure 5.2: DEM/pore network modeling flowchart of coupling cycle.

$$q_p = \frac{k_p}{\eta}\frac{P_2 - P_1}{L_p}a \tag{5.1}$$

where q_p is the flow rate through the slit; η is the fluid viscosity; $P_2 - P_1$ is the pressure difference between the two pores; $L_p = r_1 + r_2$ is the length of the slit, where r_1, r_2 are the radii of the two particles forming the aperture; a is the slit aperture ; k_p may be considered as the apparent microscale permeability [Zimmerman and Bodvarsson, 1996],

$$k_p = \frac{a^2}{12} \tag{5.2}$$

After a fluid time step Δt, the volume change ΔV for each pore can be calculated by summing up the change in the pipe flow volume around this pore,

$$\Delta V = \Delta t \sum q_p \tag{5.3}$$

knowing the volume change, the pressure increment ΔP at each pore could be updated according to,

$$\Delta P = K_f \frac{\Delta V}{V_d} \tag{5.4}$$

where K_f is the fluid bulk modulus and V_d is the current pore volume.

Each particle will be subjected to a drag force as a result of its surrounding pore pressure as shown in Figure 5.3(b). The resultant drag force is obtained by integrating the fluid pressure along the surface of the particle located inside the pore domains. The resultant fluid force F_{fluid} is applied to each particle in addition to the mechanical contact forces between particles.

5.2.2 Pore filling

The pore spaces in the domain are assumed to be dry initially. In addition to the pore pressure, fluid saturation is also stored for each pore space, $S = 0$ for a dry pore space and $S = 1$ for a fully saturated one. A pore filling procedure is first executed before the fluid calculation for pressure diffusion. The filling process is only applied

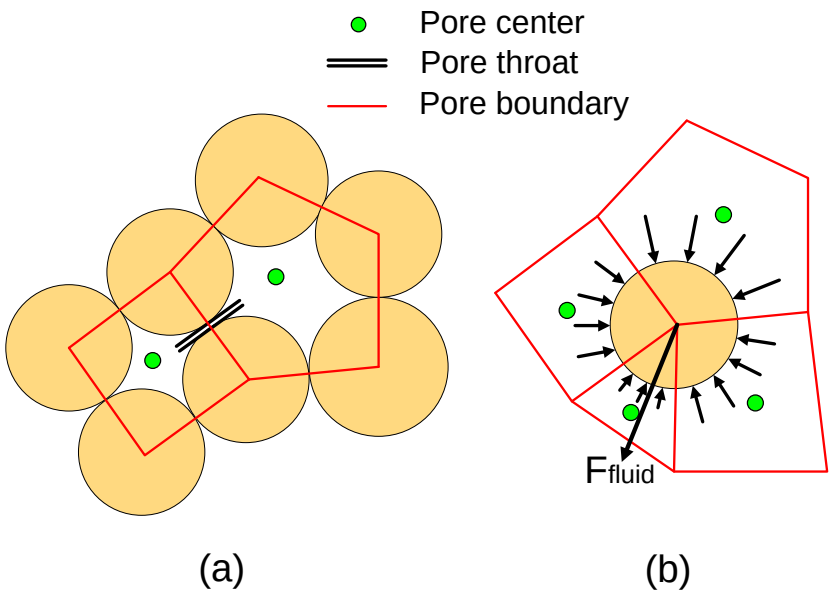

Figure 5.3: Schematic of (a) the pore network fluid flow model, and (b) pore pressure and the resultant fluid force applied to the particle.

between pores with saturation $S = 1$ and their neighboring pores with $S < 1$. Given an injection rate Q, the fluid volume to be distributed to the unsaturated pore spaces is $Q\Delta t$ at a given time step.

For the coupling calculation, two possible coupling schemes could be applied: one way coupling, and two ways coupling or full coupling. One way coupling means for one fluid injection step, fluid pressure results in additional forces to the particles for their movements while the movement of the particles will not affect the pore pressure. A full coupling scheme means, however, the movement of the particles changes the pore volume and further affects the pore pressure. It is computationally too expensive to apply full coupling to all pores. Therefore in this simulation, the fully coupling scheme is applied to borehole only. One way coupling scheme is used for all other pores.

In this simulation, three fluid bulk moduli are used for borehole calculation, pore pressure calculation and pore filling calculation, respectively. For the borehole calculation, the original fluid bulk modulus $K_f = 2 \times 10^9$ Pa is used which allows that the fluid injection in borehole controls all other processes. During the mechanical

calculation, at every 5 mechanical steps, borehole expansion is checked and the borehole pressure is adjusted according to the volume change. For the pore pressure calculation, since the one way coupling scheme is used, a reduced fluid bulk modulus $K_f^{'} = 0.75 \times 10^5$ Pa is used to avoid decreasing the fluid time step. The characteristic time scale in the pore filling process is much larger than that in the pressure diffusion, therefore the fluid bulk modulus for the filling process is further reduced to $K_f^{''} = 1 \times 10^3$ Pa to overcome the difficulty in dealing with vastly different time scales [Itasca Consulting Group, 2005].

5.3 Permeability Calibration

For the particle assembly described above, permeability at the macroscale depends on the particle configuration and the slit aperture a. The slit aperture a may be expressed as a function of local particle geometry and deformation, see Eq. (5.5),

$$a = \begin{cases} \frac{a_0 F_0}{F_n + F_0}, & \text{if } \delta > 0 \\ a_0 - \gamma\delta, & \text{if } \delta \leq 0 \end{cases} \tag{5.5}$$

where a_0 is the residual aperture; δ is the overlap between the two particles ($\delta \leq 0$ indicating a gap); F_n is the normal contact force and F_0 is the normal contact force when the overlap $\delta = \delta_0 = a_0/2$; and γ is a multiplier. Assuming a linear contact model where $F_n = K_n\delta$, Eq. (5.5) may be simplified into,

$$a = \begin{cases} \frac{a_0 \delta_0}{\delta + \delta_0}, & \text{if } \delta > 0 \\ a_0 - \gamma\delta, & \text{if } \delta \leq 0 \end{cases} \tag{5.6}$$

The residual aperture a_0 is introduced here to remove the paradox in simulating fluid flow in 2D so that fluid flow can occur when there is an overlap at the contact. The residual aperture a_0 and the overlap δ_0 can be related to the particle sizes through,

$$a_0 = \frac{\alpha\,(r_1 + r_2)}{2} \tag{5.7}$$

$$\delta_0 = \frac{\beta\,(r_1 + r_2)}{2} \tag{5.8}$$

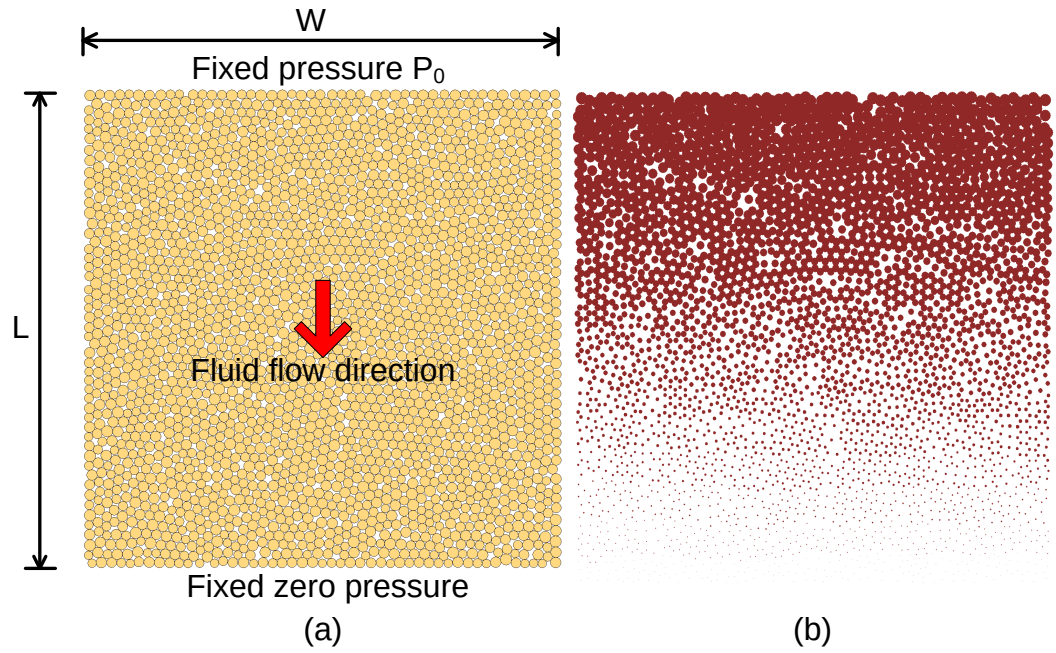

Figure 5.4: (a) Overview of the assembly for the permeability test; (b) pore pressure distribution at the steady state.

where α and β are the positive coefficients that need to be determined through permeability calibration. Given a particle assembly configuration, permeability is expected to increase with α, β and γ.

To determine the permeability of a particle assembly as a function of the microscale coefficients α, β and γ, numerical analysis of one dimensional flow through a rectilinear domain of length L and width W is performed. Initially all the pores are fully saturated, but have zero fluid pressure. As shown in Figure 5.4, a fixed constant fluid pressure $P_0 = 5$ kPa is applied at the top of the domain and zero fixed fluid pressure is applied at the bottom of the domain. In order to leave out the poroelastic effect, all the particle positions are fixed throughout the simulations.

The flow velocity and the pressure gradient P_0/L are then used to determine the permeability k via Darcy's law, after the steady state condition is reached,

$$k = \frac{\eta V L}{P_0} \tag{5.9}$$

The fluid velocity at any cross section of the domain is calculated from,

Table 5.1: Comparison of 2D and 3D porosities for mono-sized packing.

	2D porosity	3D porosity
Maximum packing density	0.0931	0.2595
Minimum packing density	0.2146	0.4760

$$V = \frac{1}{W} \sum q_p \mid_L \tag{5.10}$$

where q_p is the flow rate at each slit given by Eq. (5.1) and W is the width of the fluid domain. The subscript L means the flow direction along the length of the domain. By substituting Eq. (5.6) into Eq. (5.10), the permeability k can be determined from,

$$k = \frac{L}{12 P_0 W} \sum \frac{(P_2 - P_1)}{L_p} a^3 \tag{5.11}$$

The numerically measured permeability of the particle assembly is compared with the permeability predicted from the Kozeny-Carman correlation [Bear, 1988],

$$k = \frac{1}{180} \frac{d_p^2 \phi^3}{(1-\phi)^2} \tag{5.12}$$

where d_p is the average particle diameter and ϕ is the assembly porosity.

Since the porosity in Eq. (5.12) is based on a 3D porosity, the 2D porosity of the particle assembly is converted to a 3D porosity by utilizing the porosity relationship for mono-sized packing with disks (2D) and spheres (3D). Table 5.1 lists the porosities corresponding to the minimum packing density (square or cubic) and maximum packing density (hexagonal) [Borchardt-Ott, 2011]. A 3D effective porosity can be obtained from the 2D porosity through linear interpolation using Eq. (5.13). The 3D porosity obtained from Eq. (5.13) is then applied in Eq. (5.12) to obtain the predicted permeability for the particle assembly.

$$\phi_{3D} = 0.2595 + \frac{\phi_{2D} - 0.0931}{0.2146 - 0.0931}(0.476 - 0.2595) \tag{5.13}$$

A simple approach is developed here to determine the calibration constants α, β and γ. It can be seen from Eqs. (5.6)-(5.8) that the coefficients β and γ affect the

permeability when the particles overlap or have a gap, respectively. When the particles are just in contact, the most critical parameter is the coefficient α or the residual aperture α_0. The permeability of the particle assembly can therefore be calibrated through a three-step approach. The coefficient α is firstly determined by using a baseline particle configuration generated at a relatively low initial confining stress, i.e., the condition when both β and γ do not have significant roles. The coefficient β is then calibrated by matching the permeability when the baseline configuration is further compressed. The coefficient γ is lastly determined using particle configurations with substantial percentage of contacts in tension.

The baseline test numerical model of size $W = L = 75$ mm consisting of 4376 particles is generated with an initial confining stress $\sigma = 0.1$ MPa. The particle radius of the assembly is uniformly distributed, ranging from 0.5 to 0.7 mm. Porosity of this baseline configuration is $\phi_{2D} = 0.1646$. The frictional coefficient of the particles is set to $\mu_p = 0.577$ and density $\rho = 2650$ kg/m^3. The linear contact model is employed for the particle-particle contact. The contact normal stiffness K_n and the shear stiffness K_s are equal to 0.833×10^8 N/m. Though the contact model here is only elastic and frictional with no bond strength, when two particles are in close proximity, they are considered in contact with zero contact force. In the baseline configuration, 2975 out of 11009 total contacts have zero contact forces and 8034 (73%) contacts are in compression.

Tests A and B with $\alpha = 0.45$ and 0.55 are first performed with the baseline configuration. The parameter are set to $\beta = 20000$ and $\gamma = 1$ (see Table (5.2)). As shown in Figure 5.5, the results from Tests A and B bracket the analytical prediction from the Kozeny-Carman correlation. We therefore choose $\alpha = 0.5$ and attempt in the second step to determine the coefficient β by matching the permeability as a function of the initial confining stress σ.

Two series of tests, Series 2 and 3, are performed with $\beta = 0.12$ and $\beta = 0.16$, $\alpha = 0.5$ and $\gamma = 1$. In these series, two new particle configurations are obtained by compressing the baseline sample to initial stress levels $\sigma = 0.5$ and 1 MPa. As the confining stress increases, the pore network configurations are refined. At $\sigma = 1$

MPa, the porosity is now $\phi_{2D} = 0.1263$ and 9514 out of 11299 total contacts, i.e., 84%, are in compression. The numerical results from Series 2 and 3 agree well with the theoretical prediction. The discrepancies increase with the confining stress level. At $\sigma = 1$ MPa, the difference between the numerical results and analytical prediction are 6.9% and 13.7% for Series 2 and 3, respectively.

In order to determine the last parameter , three additional particle configurations are generated by uniformly stretching the particle assembly initially at the confining stress $\sigma = 0.5$ MPa. Large normal and shear bond strengths are assigned to all the contacts so that the total number of contacts remains more or less the same during the stretch. Porosity of the particle assembly increases from the initial value of $\phi_{2D} = 0.146$ at $\sigma = 0.5$ MPa to $\phi_{2D} = 0.148$, 0.152 and 0.1646. The case with $\phi_{2D} = 0.1646$ has the same porosity as the baseline configuration. However, the contact structures in these two cases are rather different. At $\phi_{2D} = 0.1646$, 7500 out of 11075 total contacts now have gaps ($\delta < 0$), i.e., 67.7% compared to 27% in the baseline configuration.

The results from Series $4 - 6$ with $\alpha = 0.5$ and $\beta = 0.136$, and $\gamma = 1$, 1.2 and 1.4 are shown in Figure 5.6. The discrepancy in the numerical results for the three values of γ increases only slightly as the porosity increases.

The calibration coefficients are therefore chosen to be $\alpha = 0.5$, $\beta = 0.136$ and $\gamma = 1.2$. Permeability for the particle configurations at various initial stresses ranging between the numerical results and the analytical prediction is shown in Figure 5.5. The difference is less than 2.6%.

It should be noted that this procedure to determine the calibration constant is indeed arbitrary to a certain degree. It nevertheless reflects the fact that the three coefficients play critical roles at different conditions. Though in principle it is possible to determine the three coefficients through inverse analysis, the effort is likely exhaustive. This three-step approach is a simple and straightforward alternative and requires much less computational effort. In addition, though only limited ranges of porosity are considered in calibrating the permeability, local porosity in the injection simulations is not expected to be greatly different. For the purpose of modeling the

Table 5.2: Parameters in Tests A and B and Series $1-6$ for permeability calibration.

	α	β	γ
Test A	0.45	20000	1.0
Test B	0.55	20000	1.0
Series 1	0.5	0.136	1.2
Series 2	0.5	0.12	1.0
Series 3	0.5	0.16	1.0
Series 4	0.5	0.136	1.4
Series 5	0.5	0.136	1.2
Series 6	0.5	0.136	1.0

injection process in this work, the calibration procedure described above is considered adequate.

5.4 Injection Model Setup

5.4.1 Model parameters

A 2D hollow-circular assembly is setup as the simulation domain, as shown in Figure 5.7. The hollow circular domain has outer diameter $d_o = 160$ mm and inner diameter $d_i = 8$ mm. The assembly has 15605 particles with radii ranging from 0.5 to 0.7 mm. The microscale parameters in the injection test are taken to be the same as those in the permeability tests. All particles have a frictional coefficient $\mu_p = 0.577$ and density $\rho = 2650$ kg/m^3.

The linear contact model is employed for the particle-particle contact. The contact normal stiffness K_n and the shear stiffness K_s are set as equal to 0.833×10^8 N/m. Both the inner and outer circular walls are frictionless and the stiffnesses of the walls are the same as the particles. The assembly for the baseline setup has a constant radial confining stress $\sigma^{'} = 0.5$ MPa.

5.4.2 Material strength

The macroscale material strength is measured by biaxial tests under different confining stresses from 0.1 to 1 MPa. The biaxial specimen is a rectangle of height 100 mm

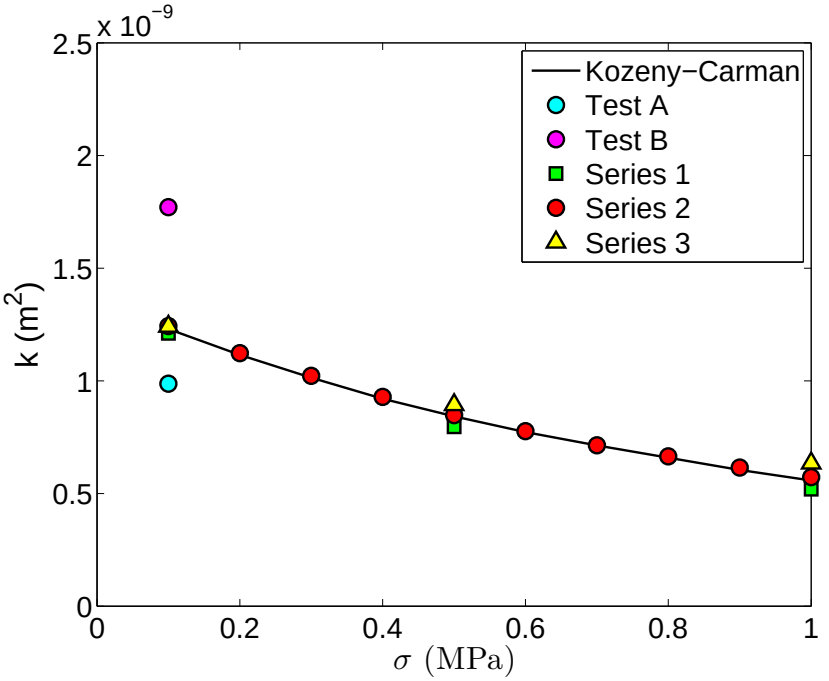

Figure 5.5: Comparison between the numerical results obtained from Tests A and B and Series $1-3$ and the analytical prediction from Kozeny-Carman correlation; the initial confining stress σ refers to the stress level before the fluid flow calculation.

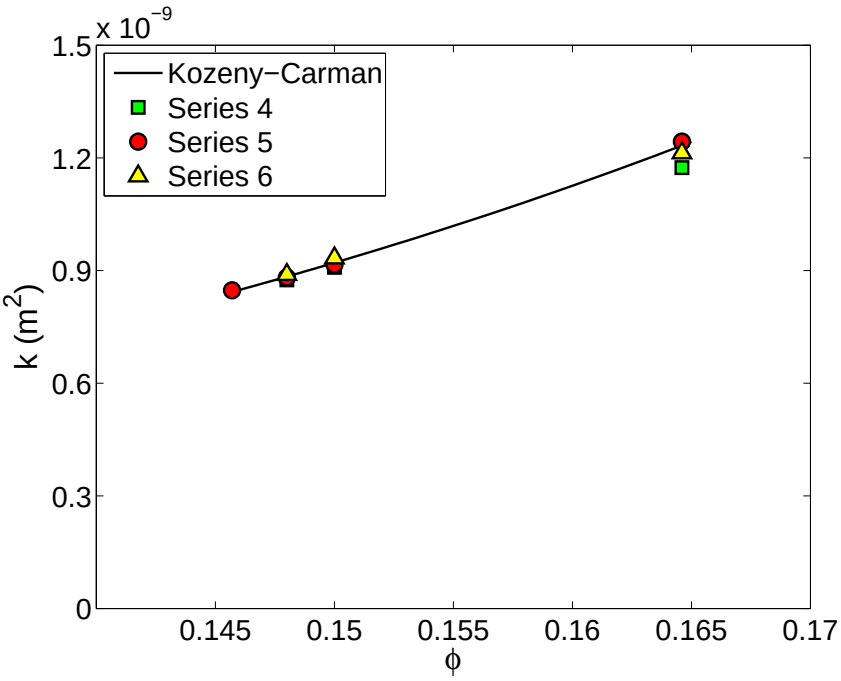

Figure 5.6: Comparison between the numerical results obtained from Series $4-6$ and the analytical prediction from the Kozeny-Carman correlation.

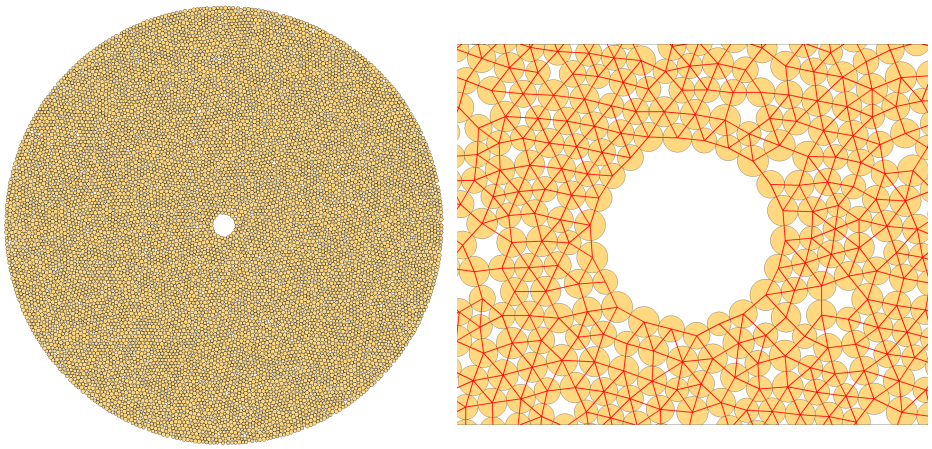

Figure 5.7: (a) Overview of the simulation domain; (b) borehole vicinity with the pore network added on.

and width 50 mm. The specimen has a uniform particle radius distribution ranging from 0.5 to 0.7 mm and the total number of particle is 3890. Since the strain-stress behavior of granular media is nonlinear, the elastic modulus and Poisson's ratio at the stress level of 50% peak stress are shown in Figures 5.8 and 5.9. Variation of the peak friction angle as a function of the confining stress is shown in Figure 5.10.

5.5 Effect of Injection Flow Rate

5.5.1 Displacement patterns

A series of eight tests are carried out by increasing the injection flow rate. The injection parameters for this series are summarized in Table 5.3. The fluid viscosity and the far field confining stress are $\eta = 1$ Pa·s and $\sigma^{'} = 0.5$ MPa for all tests. As the flow rate increases, both the fluid time step and total injection time decrease. Figure 5.11 shows the displacement patterns for the eight tests at the end of injection. The color in the disks indicates the fluid pressure. The fluid pressure at the location of a particle is obtained by averaging the pressure in the neighboring pores. The interface between the blue disks and the grey hollow circles can be interpreted as the infiltration front. The black circle indicates the initial borehole position.

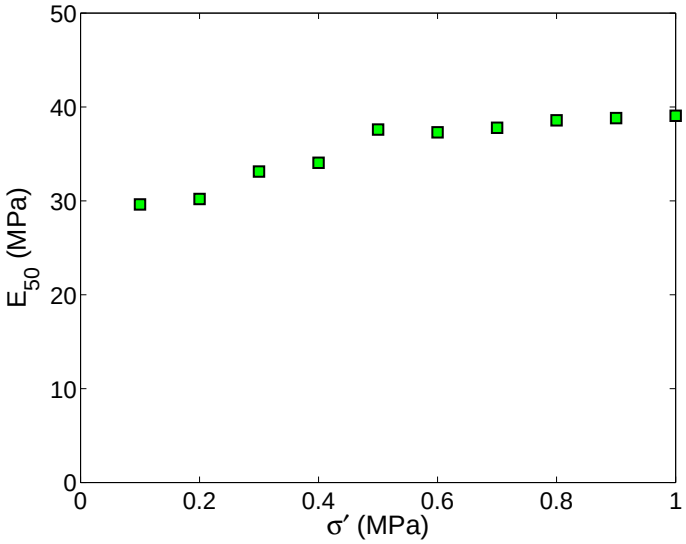

Figure 5.8: Elastic modulus of the material under different confining stress from 0.1 MPa to 1 MPa.

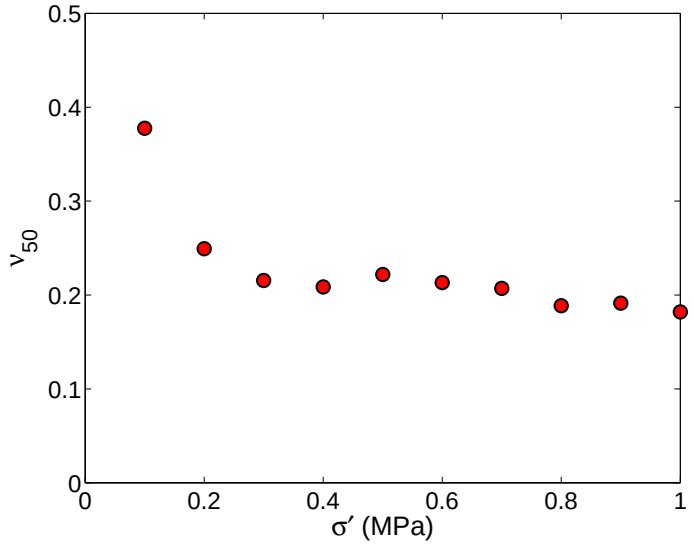

Figure 5.9: Poisson's ratio of the material under different confining stress from 0.1 MPa to 1 MPa.

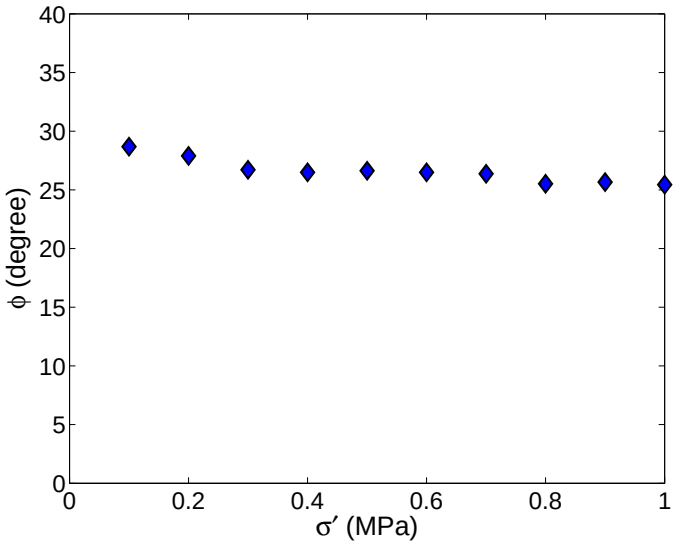

Figure 5.10: Peak friction angle of the material under different confining stress from 0.1 MPa to 1 MPa.

The results from these series of simulations shown in Figure 5.11 show behaviors similar to what we observed in the Hele-Shaw cell experiments. As the injection rate increases, fluid flow shows a transition from infiltration-governed to infiltration-limited. The granular media response also evolves from that of a fixed bed to localized failure or growth of granular fingers.

5.5.2 Injection rate 0.01 m^2/s

Figure 5.12 shows the evolution of the displacement patterns for the injection rate $Q = 0.01$ m^2/s. During the injection process, grain displacements are negligible and the particle assembly behaves as a rigid porous media. The injected fluid simply permeates through the porous media with a circular infiltration front.

Figure 5.13 shows the the contact force chain at different times. The contact force changes very little during the injection process. As the borehole pressure keeps increasing, the contact force at the end of the injection has the trend of aligning radially near the borehole area.

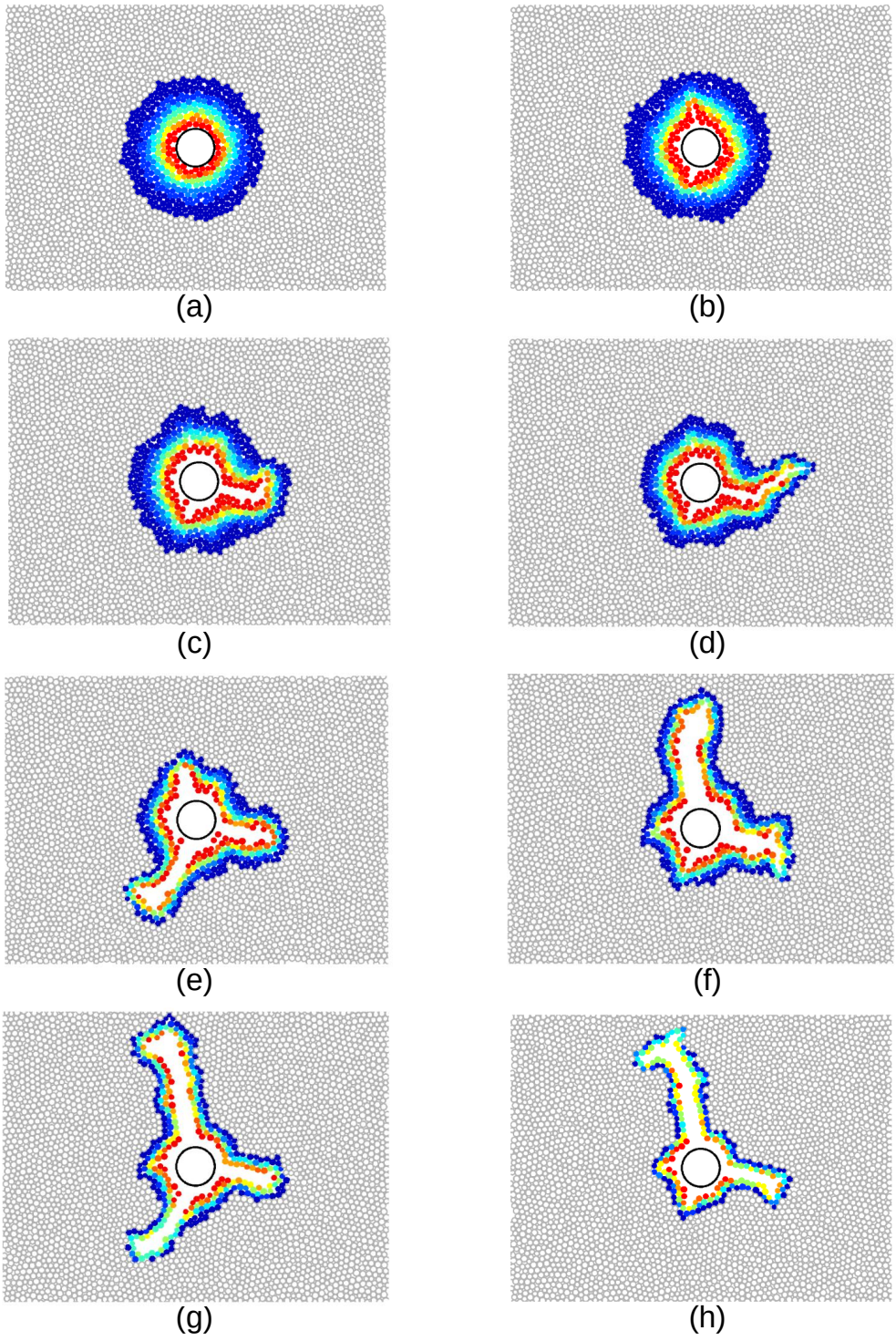

Figure 5.11: Displacement patterns for tests with different injection flow rate, (a) 0.01 m^2/s at $t = 0.048$ s; (b) 0.02 m^2/s at $t = 0.04$ s; (c) 0.04 m^2/s at $t = 0.024$ s; (d) 0.05 m^2/s at $t = 0.0144$ s; (e) 0.08 m^2/s at $t = 0.008$ s; (f) 0.1 m^2/s at $t = 0.0056$ s; (g) 0.12 m^2/s at $t = 0.0036$ s; (h) 0.016 m^2/s at $t = 0.0012$ s.

Table 5.3: Injection parameters for the effect of flow rate.

Test	Flow rate (m^2/s)	Fluid time step (s)	Injection time (s)
Test 1	0.01	1.2×10^{-7}	0.048
Test 2	0.02	1×10^{-7}	0.04
Test 3	0.04	5×10^{-8}	0.024
Test 4	0.05	4×10^{-8}	0.0144
Test 5	0.08	2×10^{-8}	0.008
Test 6	0.1	2×10^{-8}	0.0056
Test 7	0.12	1.5×10^{-8}	0.0036
Test 8	0.16	1×10^{-8}	0.0012

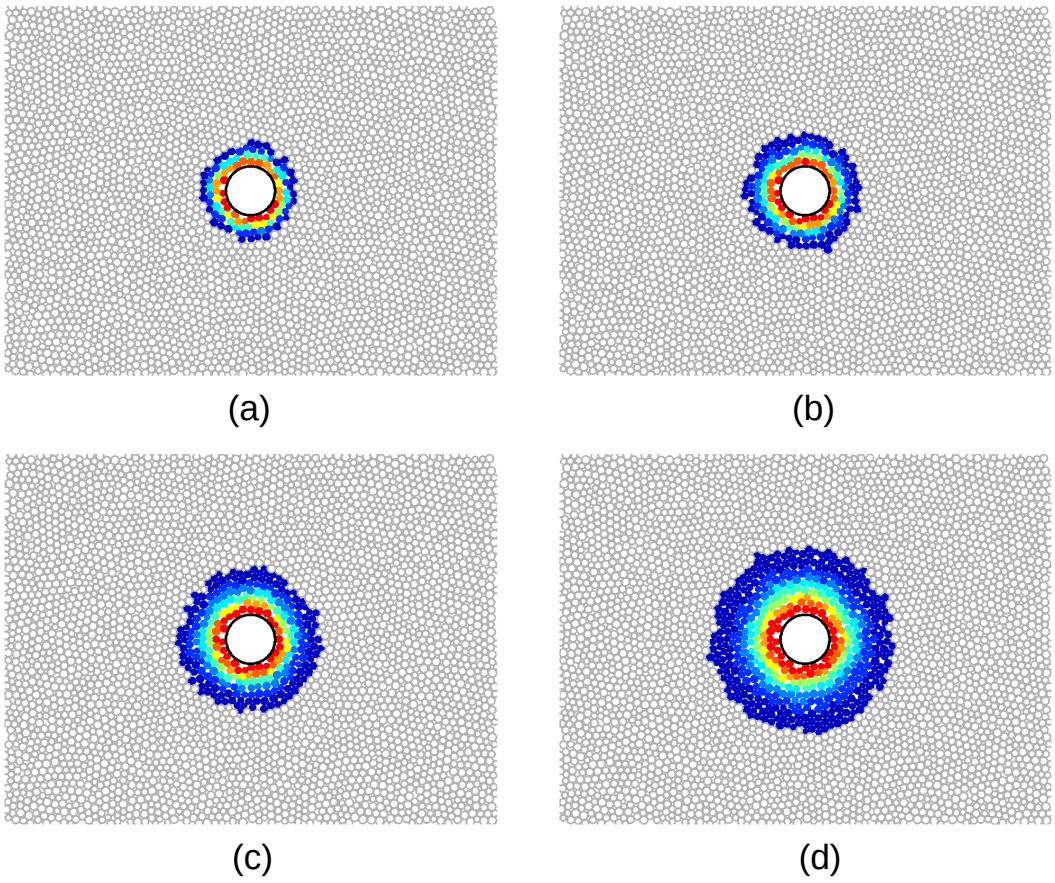

Figure 5.12: Displacement patterns for $Q = 0.01$ m^2/s at injection time (a) $t = 0.006$ s, (b) $t = 0.012$ s, (c) $t = 0.024$ s and (d) $t = 0.048$ s.

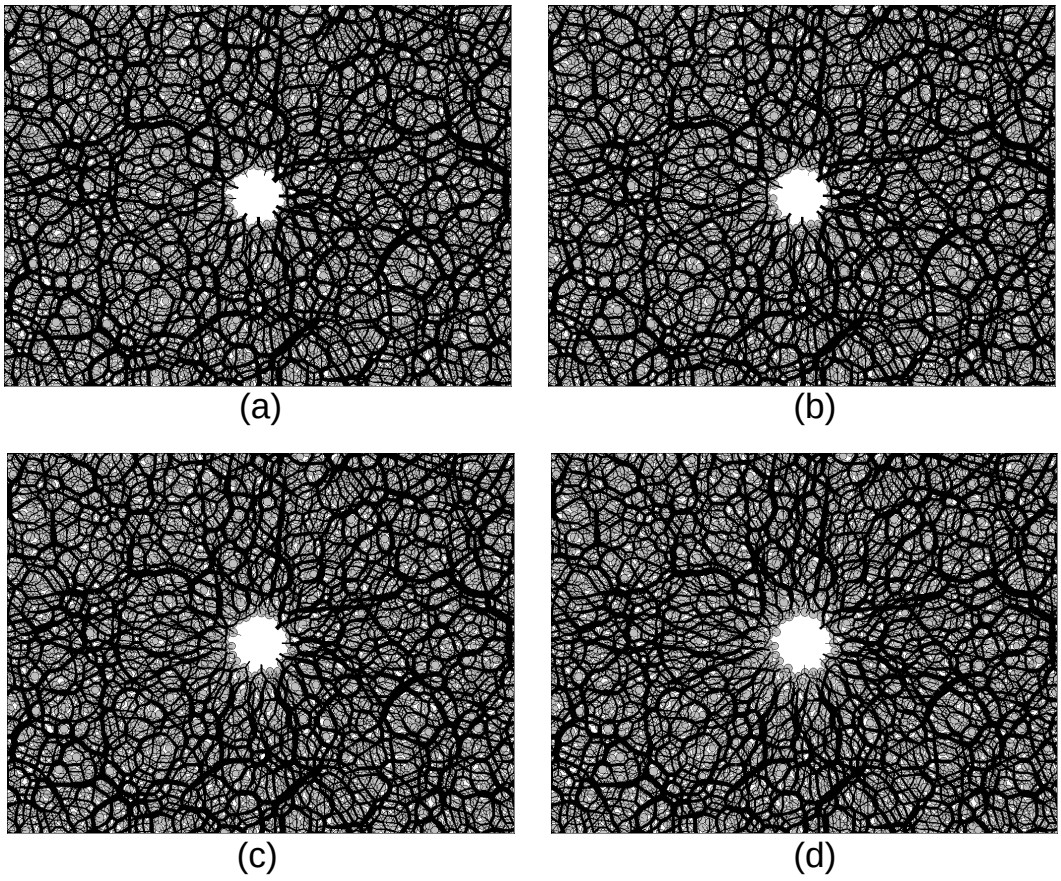

Figure 5.13: Contact force chains for $Q = 0.01$ m^2/s at injection time (a) $t = 0.006$ s, (b) $t = 0.012$ s, (c) $t = 0.024$ s and (d) $t = 0.048$ s.

5.5.3 Injection rate 0.04 m^2/s

Figure 5.14 shows the development of granular fingers for the injection rate $Q = 0.04$ m^2/s. As the injection starts, initially there is negligible particle movement for the assembly. Injected fluid permeates through the porous media with a circular infiltration front. Figure 5.14(b) show the borehole starts to have slight expansion with short fingers created around the borehole. One of the small fingers eventually develops to form a long and curved one, as shown in Figure 5.14(d). As a result, the infiltration front is no longer a circular shape at the end of the injection.

Figure 5.15 shows the evolution of the contact force chain for the injection rate 0.04 m^2/s. The contact force lines up along the radial direction initially. Once the fingering occurs, the contact force chain aligns perpendicular with respect to the finger walls, which indicates the granular media are compressed on the sides.

5.5.4 Injection rate 0.08 m^2/s

At the injection rate $Q = 0.08$ m^2/s, three main fingers are developed as a result of fluid injection, see Figure 5.16. It is interesting to note that the finger initiation locations in this case are similar to those at $Q = 0.04$ m^2/s. This suggests that the growth of the granular fingers from the wellbore is likely governed by the weakest links. Though the finger on the right side propagates first, Figure 5.16(d) suggests that the finger on the right side is arrested as the other two fingers start to propagate.

Figure 5.17 shows the evolution of the contact force chain for the injection rate 0.08 m^2/s. It shows the similar evolution process with the case in $Q = 0.04$ m^2/s.

5.5.5 Injection rate 0.16 m^2/s

As the injection rate increases to $Q = 0.16$ m^2/s, the depth of fluid infiltration is limited to about two times grain diameters, see Figure 5.18. Growth of the fingers seems to be alternating between the two main ones. In other words, when the main vertical finger propagates, the other ones are arrested. However, after the vertical finger grow to a certain length, the growth almost stops and the horizontal one takes over. As the horizontal finger grows to a certain length, it is then arrested while the

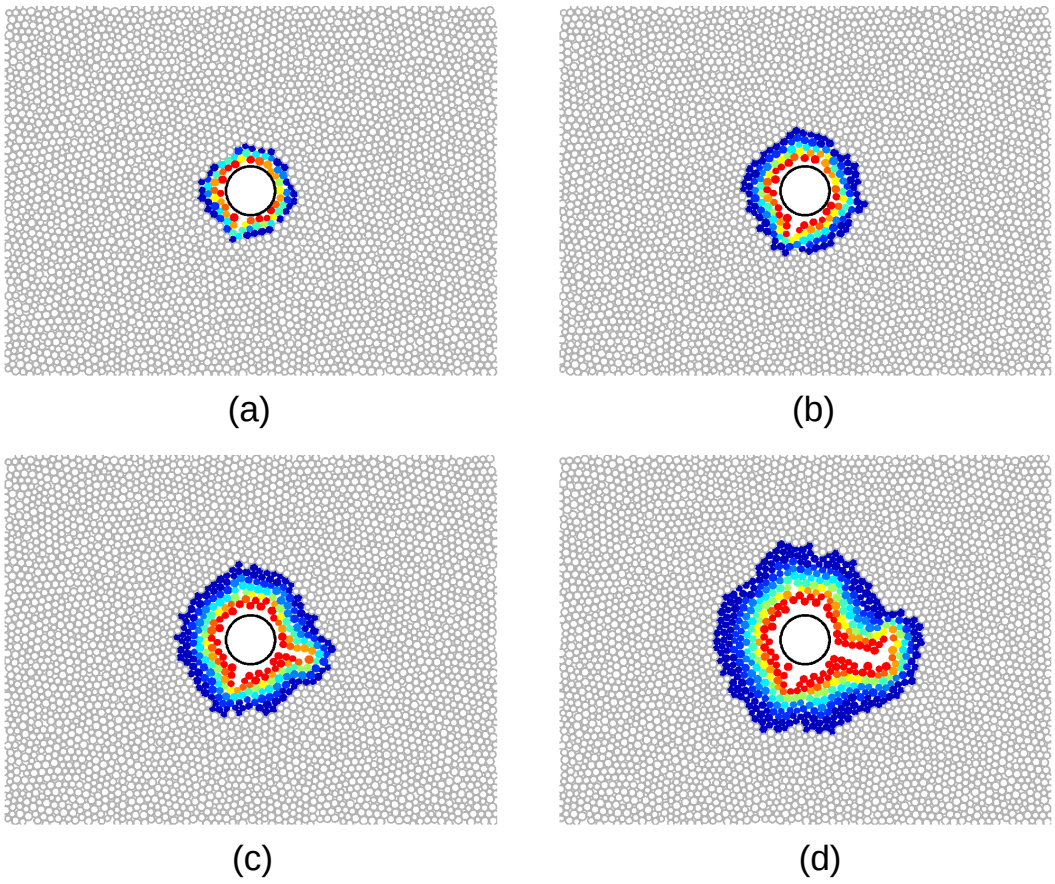

Figure 5.14: Displacement patterns for $Q = 0.04$ m^2/s at injection time (a) $t = 0.002$ s, (b) $t = 0.006$ s, (c) $t = 0.012$ s and (d) $t = 0.024$ s.

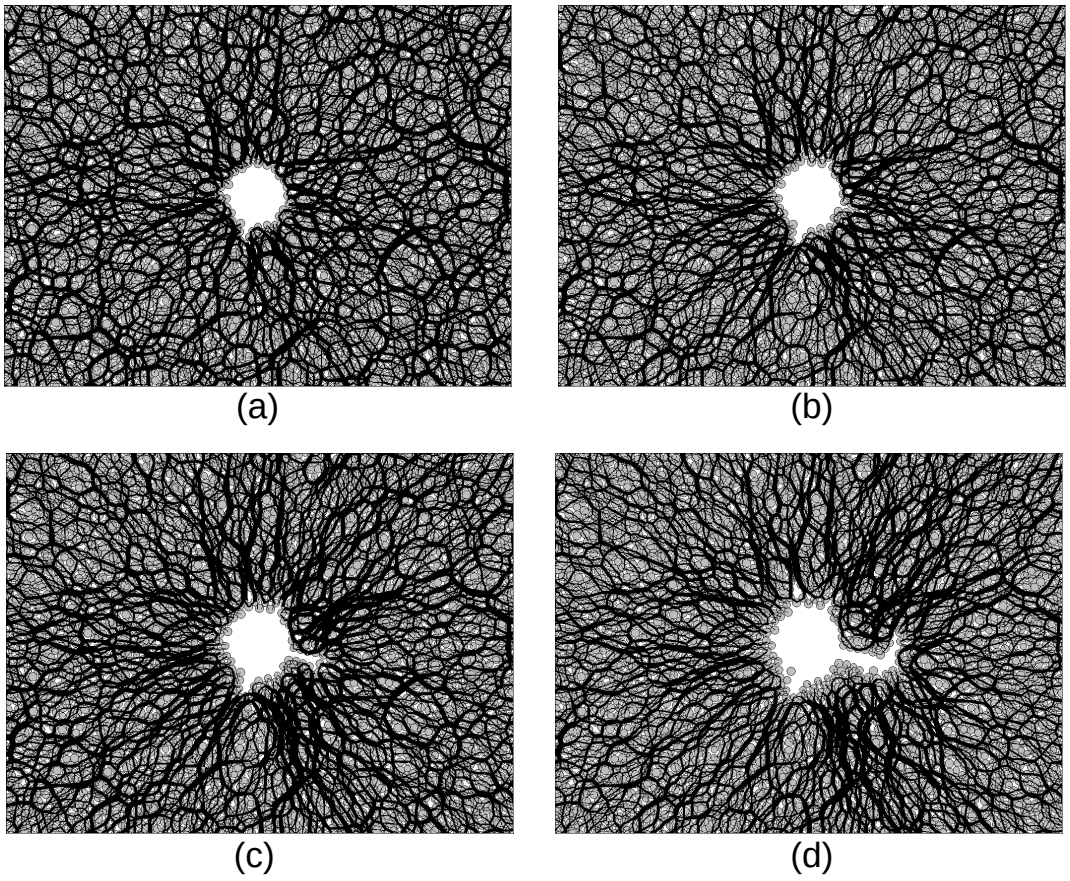

Figure 5.15: Contact force chains for $Q = 0.04$ m^2/s at injection time (a) $t = 0.002$ s, (b) $t = 0.006$ s, (c) $t = 0.012$ s and (d) $t = 0.024$ s.

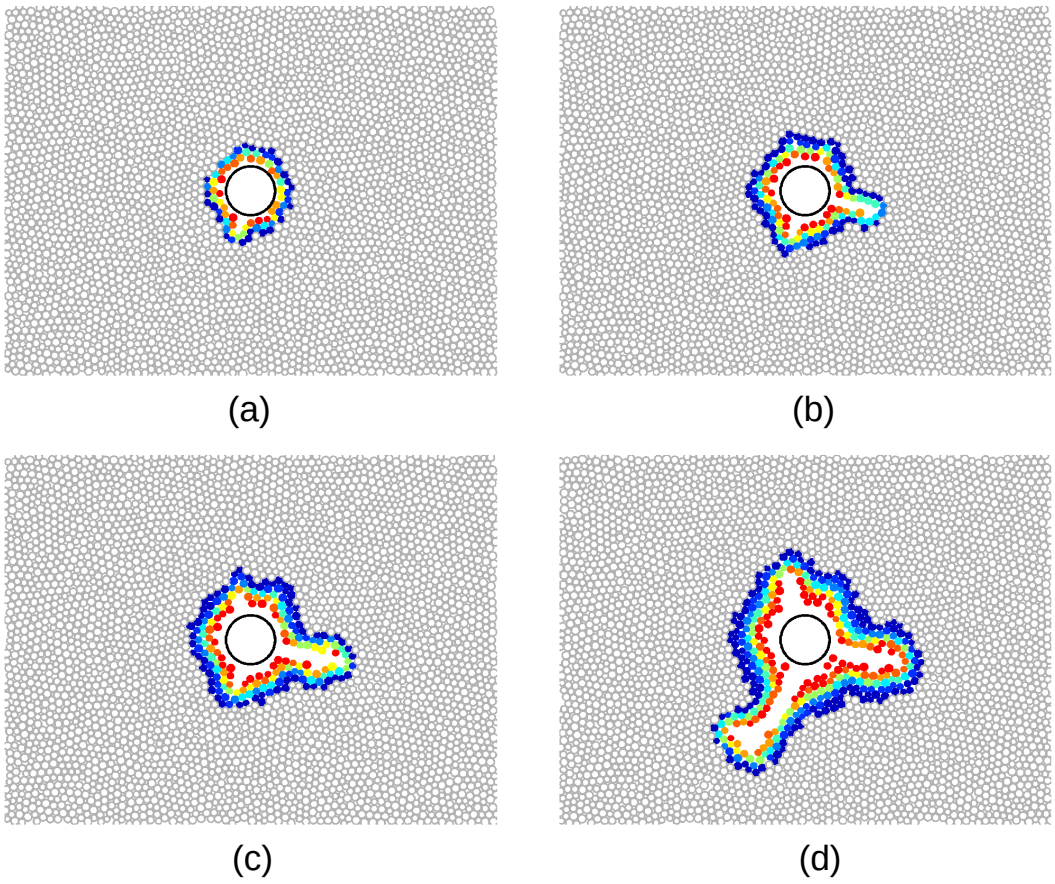

Figure 5.16: Displacement patterns for $Q = 0.08$ m^2/s at injection time (a) $t = 0.0008$ s, (b) $t = 0.0024$ s, (c) $t = 0.004$ s and (d) $t = 0.008$ s.

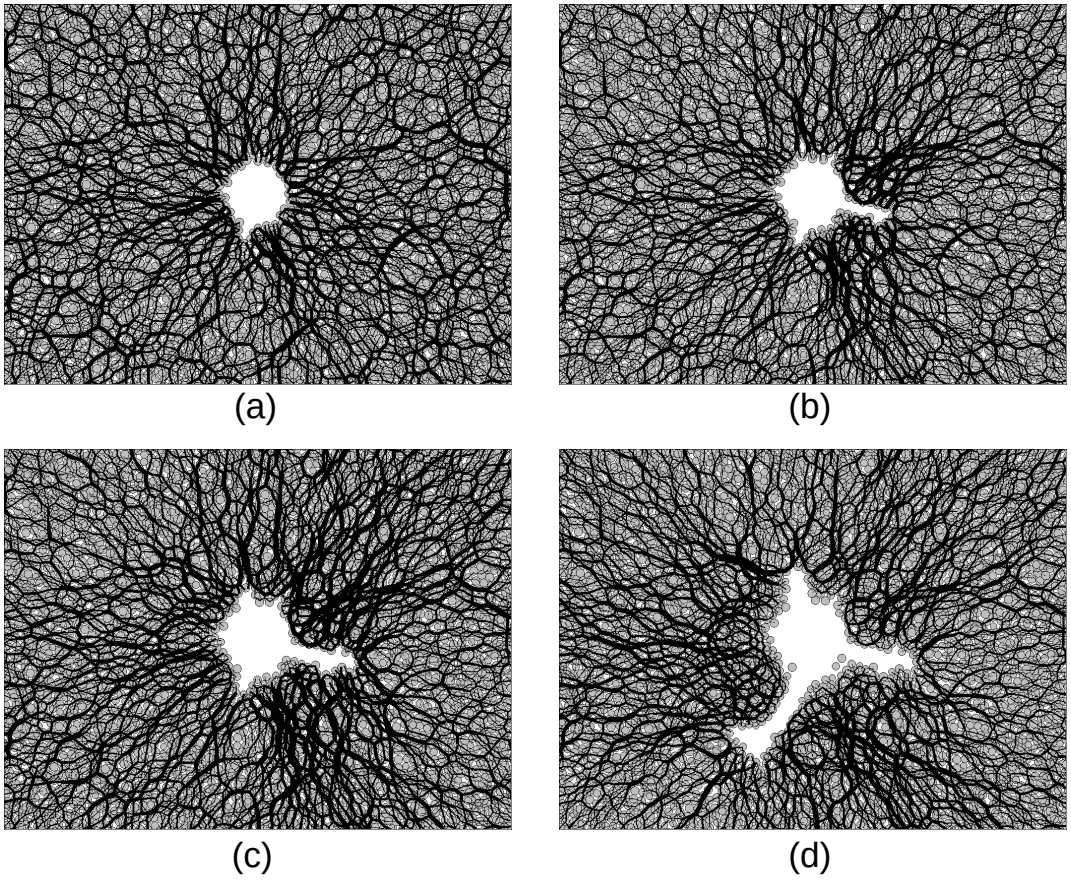

Figure 5.17: Contact force chains for $Q = 0.08$ m^2/s at injection time (a) $t = 0.0008$ s, (b) $t = 0.0024$ s, (c) $t = 0.004$ s and (d) $t = 0.008$ s.

vertical finger continues to grow.

This alternating growth scenario may be resulted from the existence of the far field confinement. The far field stress in these simulations is maintained by regulating the average radial stress on the outer wall by expanding or shrinking the confining wall radius using a servo-control algorithm. As the fingers grow, the stress field no longer maintains the circular symmetry. The side where the finger is actively growing experiences a relatively higher stress level as shown from the contact force chains in Figure 5.19. As a result, the conditions may be met on the inactive side for the fingers to grow.

In all the above cases, near the end of the injection, the finger grows in a direction perpendicular to the main branch direction, instead of the 45° angle as observed in the experiments. This may mean that the level of local stress anisotropy is also a factor that affects the fingering direction.

To better understand the finger initiation mechanism, two moments right before and after the finger initiation are chosen for the analysis. Figure 5.20 shows the particle velocity field for the two moments. As shown in Figure 5.20(a), before the initiation of the main finger, three short fingers have developed due to the borehole expansion. The particle velocities along the borehole are mainly in the radial direction. Along the short finger wall, the particle velocities have a 45° angle with the finger direction. After the initiation of the main finger in the vertical direction, the particle velocities along the finger walls are vertically aligned to make void for the finger propagation. Interestingly because of the tip dilation due to the initial opening, few particles near the interface have the trend to come back to the finger area (see 5.20(b)). Figure 5.21 shows the contact force chains for the two moments. The contact force chains before the finger initiation lines up along the radial direction due to the borehole expansion. After the finger initiation, the contact force chains near the finger propagation direction are reorganized. The finger tip area has small scale force chain due to the dilation while the large scale contact force chain aligns perpendicular with respect to the finger walls, which indicates the compression on the sides.

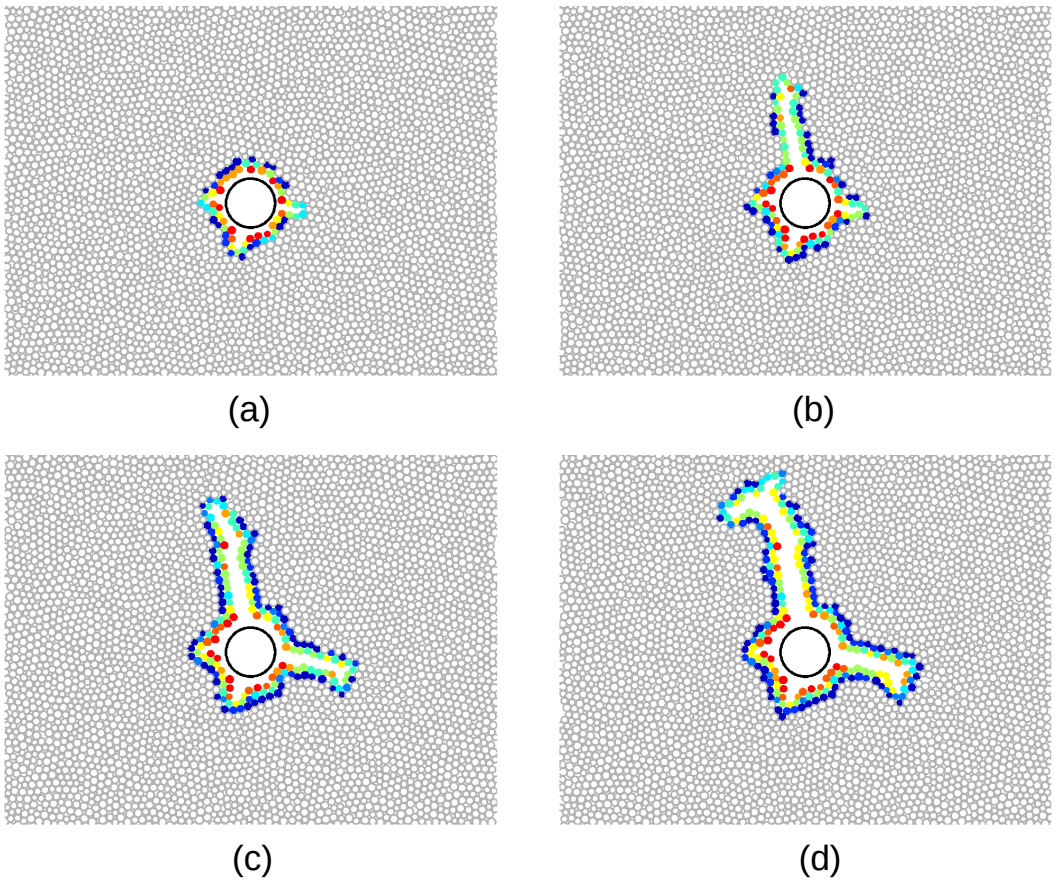

Figure 5.18: Displacement patterns for $Q = 0.16\,\mathrm{m}^2/\mathrm{s}$ at injection time(a) $t = 0.0002$ s, (b) $t = 0.0004$ s, (c) $t = 0.0008$ s and (d) $t = 0.0012$ s.

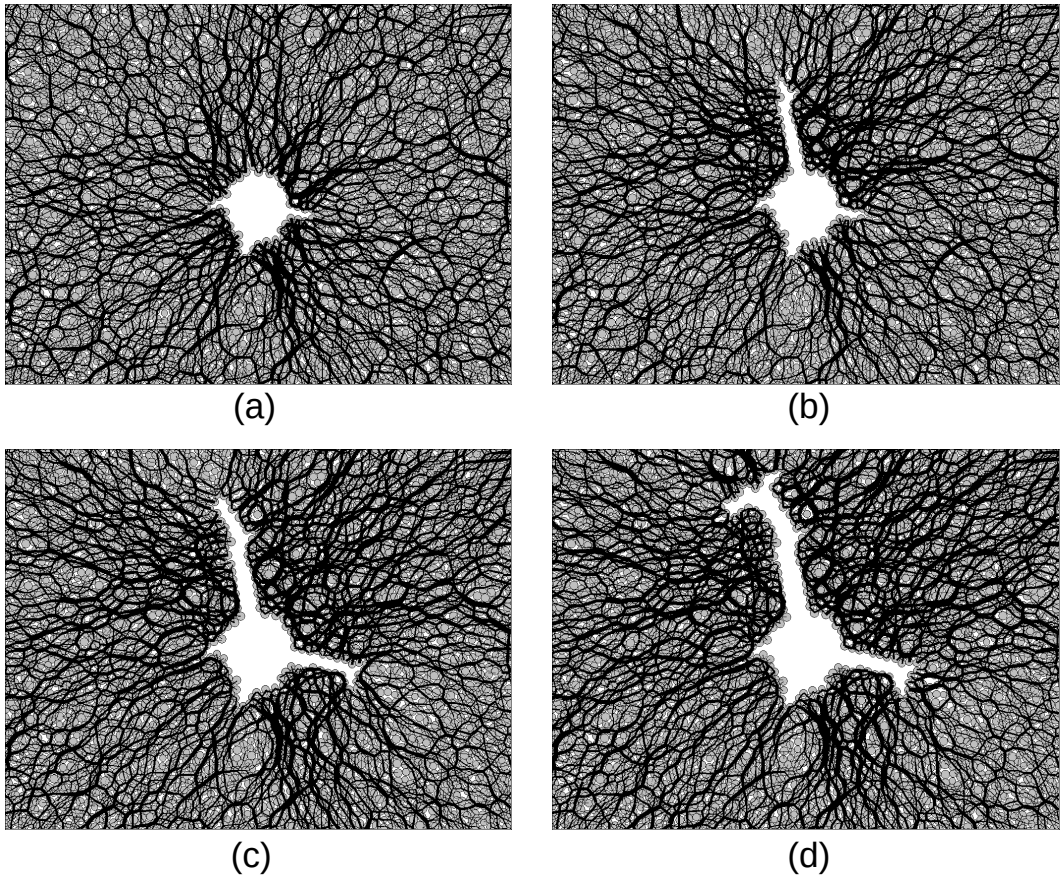

Figure 5.19: Contact force chains for $Q = 0.16$ m^2/s at injection time (a) $t = 0.0002$ s, (b) $t = 0.0004$ s, (c) $t = 0.0008$ s and (d) $t = 0.0012$ s.

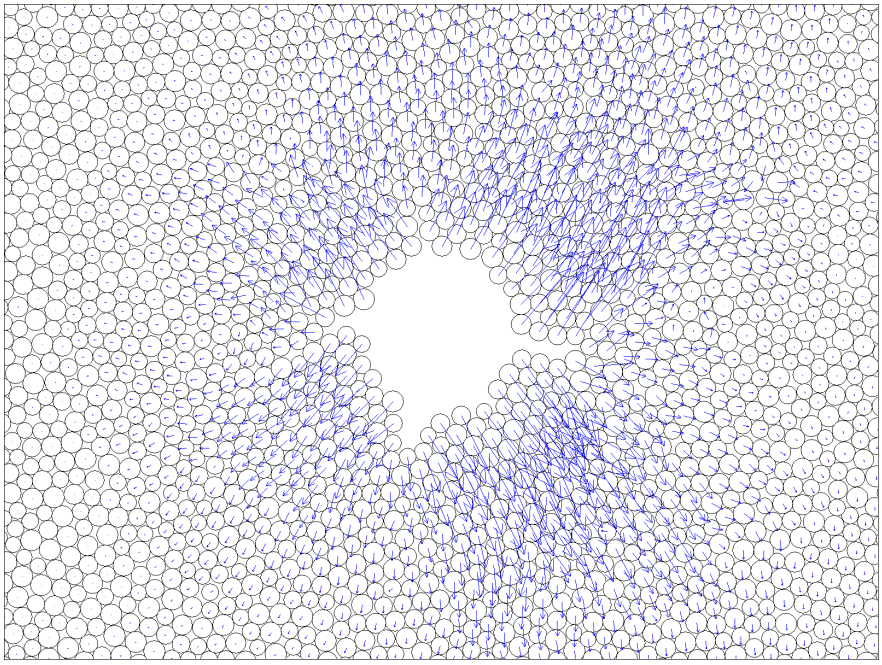

(a)

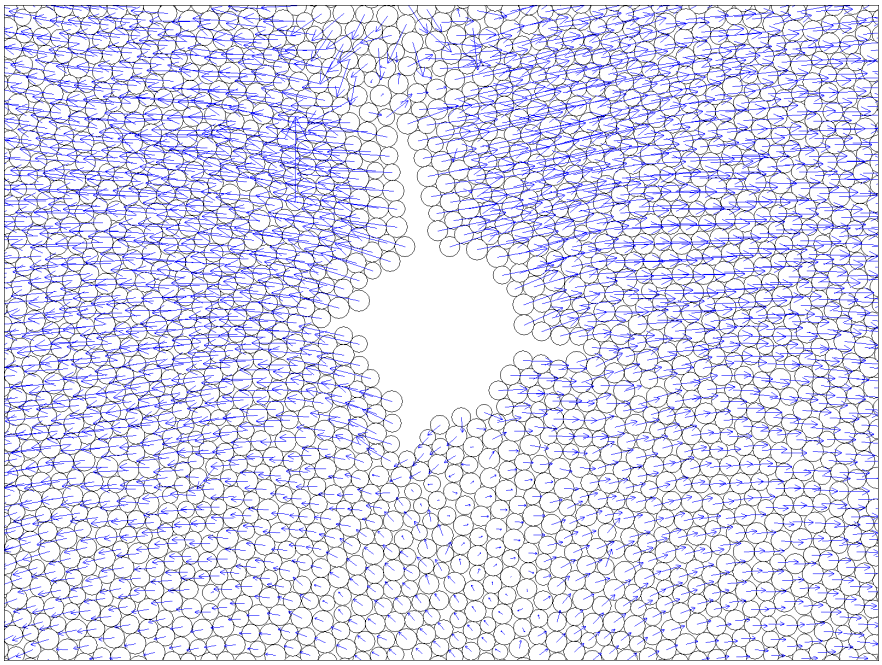

(b)

Figure 5.20: Particle velocity field for $Q = 0.16$ m^2/s at injection time (a) $t = 0.00021052$ s, (b) $t = 0.00021152$ s.

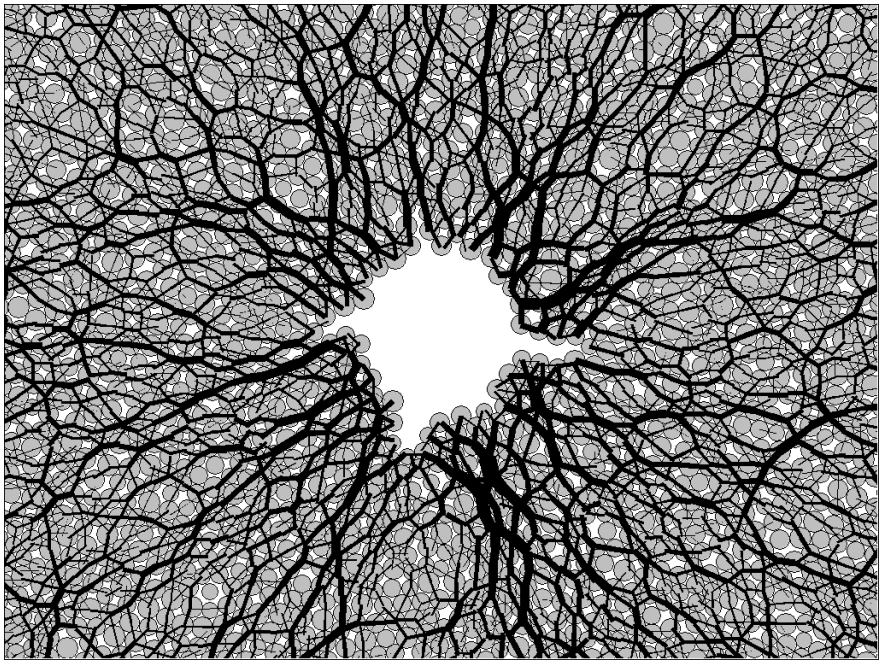

(a)

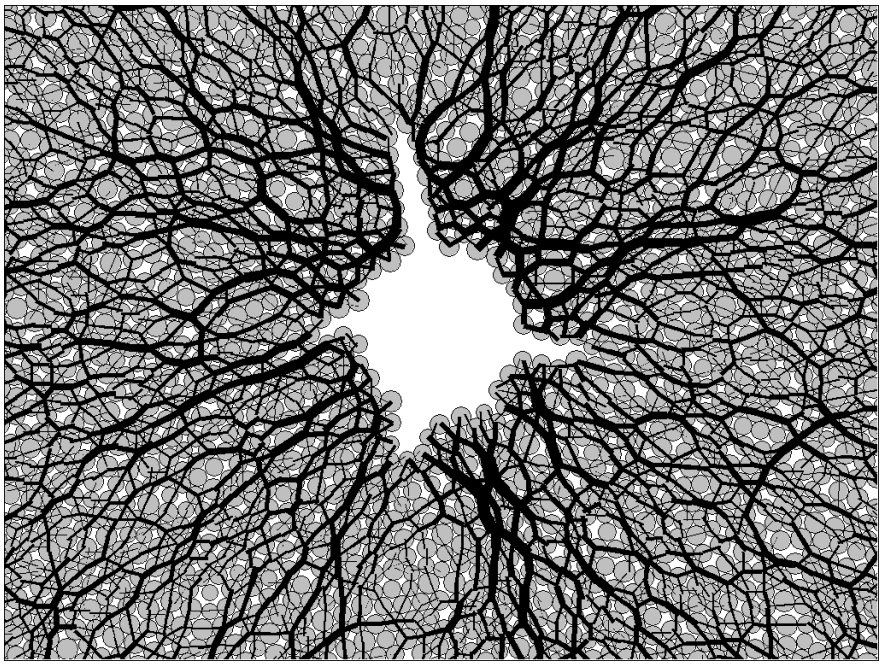

(b)

Figure 5.21: Particle velocity for $Q = 0.16\ \mathrm{m}^2/\mathrm{s}$ at injection time (a) $t = 0.00021052$ s, (b) $t = 0.00021152$ s.

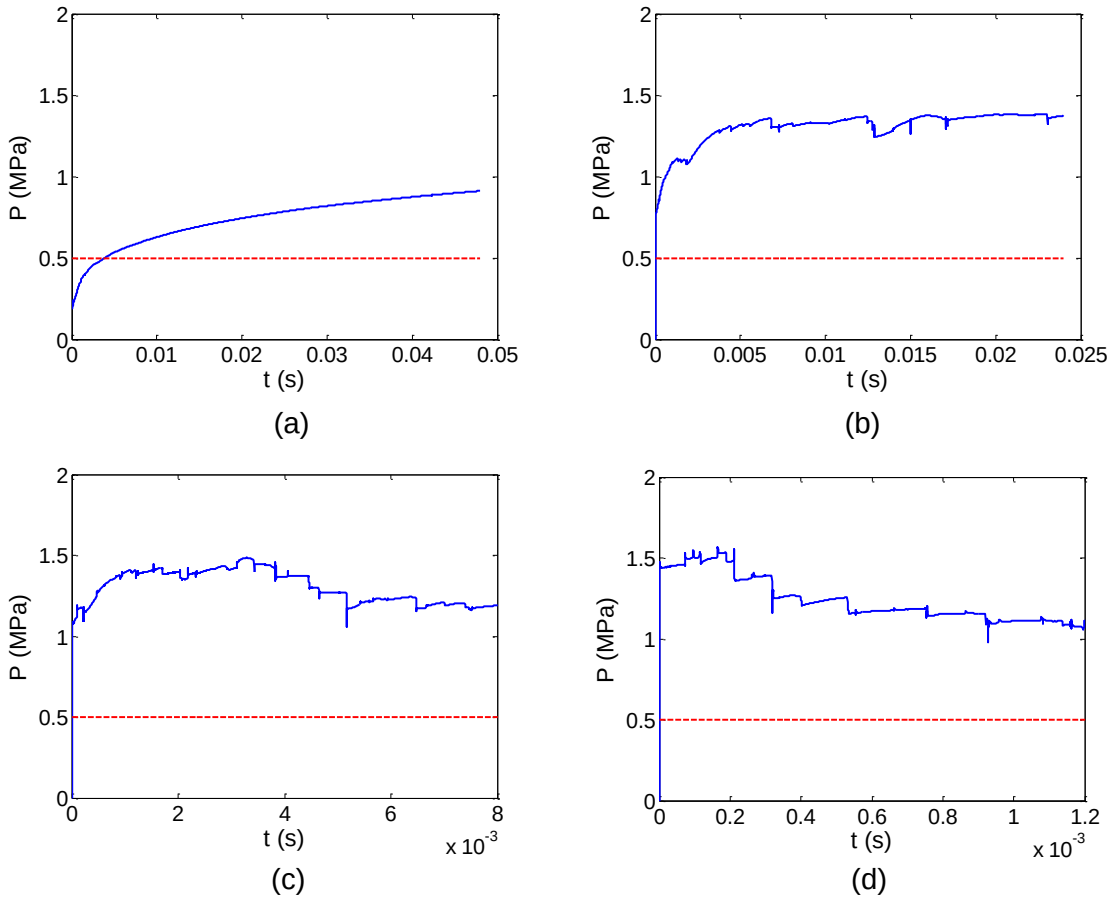

Figure 5.22: Borehole pressure history for different injection rates (a) 0.01 m^2/s, (b) 0.04 m^2/s, (c) 0.08 m^2/s and (d) 0.16 m^2/s. The red dashed line indicates the confining stress $\sigma^{'} = 0.5$ MPa.

5.5.6 Injection pressure history

Figure 5.22 shows the borehole pressure history for the four different injection rate tests: $Q = 0.01$ m^2/s, 0.04 m^2/s, 0.08 m^2/s and 0.16 m^2/s. At $Q = 0.01$ m^2/s, the borehole pressure keeps increasing which indicates a transient radial flow. At $Q = 0.04$ m^2/s, the borehole pressure keeps the increasing trend but there are many small drops due to the small fingerings generated around the borehole. At $Q = 0.08$ m^2/s and 0.16 m^2/s, the borehole pressure initially has an increasing trend corresponding to the borehole expansion stage. Later on, as the fingers start to propagate, the borehole pressure starts to decline.

5.5.7 Energy tracking

The concept of associating energy partition with the displacement regimes is investigated here. Since constant pressure is assumed on the walls of the granular fingers in this coupling scheme, there is no viscous dissipation due to fluid flow along the granular finger. We therefore focus on energy dissipation associated with viscous flow in the granular domain, energy dissipation due to particle traveling in a viscous fluid, friction and elastic storage.

Energy partition of the particle assembly during the injection process can be tracked as follows.

Body force work E_b: total accumulated work done by all body forces including applied forces and moments. Here the applied forces to each particle come from the fluid force as a result of its surrounding pore pressure.

$$E_b \leftarrow E_b + \sum_{N_p} (F_i \Delta U_i + M_i \Delta \theta_i) \tag{5.14}$$

where N_p, F_i, M_i ΔU_i and $\Delta \theta_i$ are the number of particles, externally applied force, externally applied moment, displacement increment and rotation increment, respectively. This body force work term therefore reflects the energy dissipated due to particles traveling in a viscous fluid.

Boundary work E_w: total accumulated work done by all walls to the particle assembly.

$$E_w \leftarrow E_w + \sum \sigma^{'} L_w \Delta U_w \tag{5.15}$$

where $\sigma^{'}$, L_w and ΔU_w are the confining stress on the wall, length or perimeter of the wall (2D), displacement increment of the wall.

Frictional work E_f: total dissipated energy by frictional sliding at all contacts.

$$E_f \leftarrow E_f + \sum_{N_c} \bar{F}_i^s (\Delta U_i^s)^{slip} \tag{5.16}$$

where N_c, $\bar{F}_i^s$ and $(\Delta U_i^s)^{slip}$ are the number of contacts, average shear force and

increment of slip displacement, respectively. The increment of slip displacement is equal to the total displacement subtracting the elastic portion.

$$(\Delta U_i^s)^{slip} = \Delta U_i^s - (\Delta U_i^s)^{elas} = \Delta U_i^s + \frac{(\Delta F_i^s)^{elas}}{k^s} \tag{5.17}$$

where ΔU_i^s, $(\Delta F_i^s)^{elas}$ and k^s are the total shear displacement, shear elastic force increment and shear stiffness, respectively.

Kinetic energy E_k: total kinetic energy of particles including the translational and rotational motion.

$$E_k = \frac{1}{2}\sum_{N_p}(m_i V_i^2 + I_i \omega_i \cdot \omega_i) \tag{5.18}$$

where N_p, m_i, I_i, V_i and ω_i are the number of particles, mass, moment of inertia, translational velocity and angular velocity, respectively.

Strain energy E_c: total strain energy of the particle assembly stored at all contacts in a linear contact-stiffness model.

$$E_c = \frac{1}{2}\sum_{N_c}(|F_i^n|^2/k^n + |F_i^s|^2/k^s) \tag{5.19}$$

where N_c, $|F_i^n|$, $|F_i^s|$, k^n and k^s are the number of contacts, magnitude of normal contact force, magnitude of shear contact force, normal stiffness and shear stiffness, respectively.

Besides the particle assembly, the accumulated viscous dissipation E_v of fluid flow in the porous media can also be tracked.

$$E_v \leftarrow E_v + \sum_{N_p} q_p \Delta t (P_2 - P_1) \tag{5.20}$$

where N_p, q_p, Δt and $(P_2 - P_1)$ are the number of fluid paths, flow rate at each fluid path given by Eq. (5.1), the fluid time step and the pressure difference between two pores, respectively.

Figures 5.23, 5.24, 5.25 and 5.26 show energy partition during the injection process for the four tests with injection rate $Q = 0.01$ m^2/s, 0.04 m^2/s, 0.08 m^2/s and 0.16

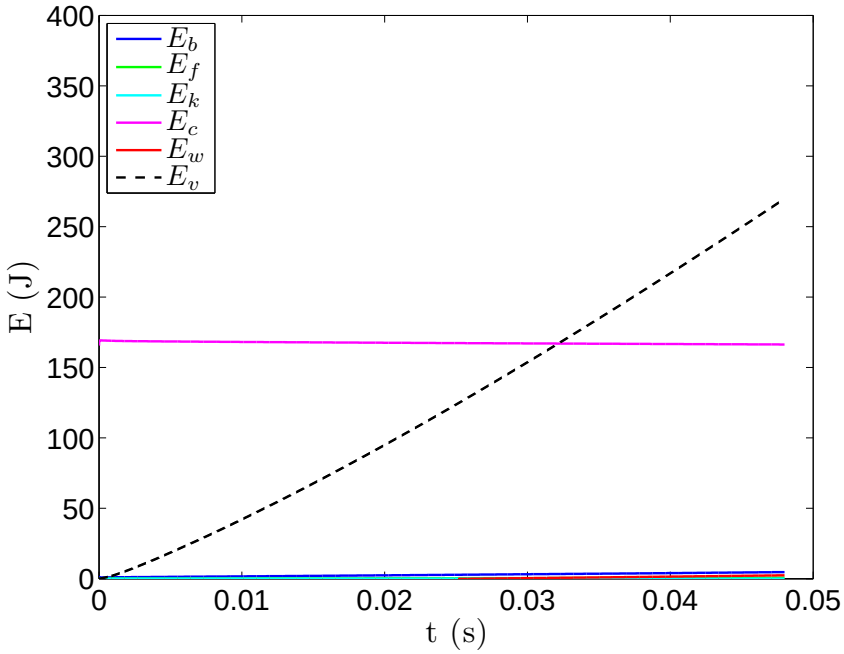

Figure 5.23: Energy partition during the injection process for injection rate 0.01 m^2/s.

m^2/s, respectively. For all the four tests, the total strain energy in the system is more or less constant under the same confining stress.

For injection rate 0.01 m^2/s, viscous dissipation of fluid flow in porous media is the dominant effect. Since there is nearly no particle movement occurring as the result of fluid injection, dissipation due to friction is close to zero. For injection rate 0.04 m^2/s and 0.08 m^2/s, although viscous dissipation still dominates, all the other terms gradually increase with time. For injection rate 0.16 m^2/s, the body force work is comparable with viscous dissipation. That implies that grain displacements in the viscous fluid become a dominating energy dissipation mechanism. The multiple increments in the Figure 5.26 is due to intermittent propagation of fingers during the injection.

Though viscous dissipation through fluid flow in the granular finger is neglected during the simulation, the energy analysis here validates our argument that the displacement regimes in the injection process essentially emerge as a result of the competition among various forms of energy dissipation mechanisms.

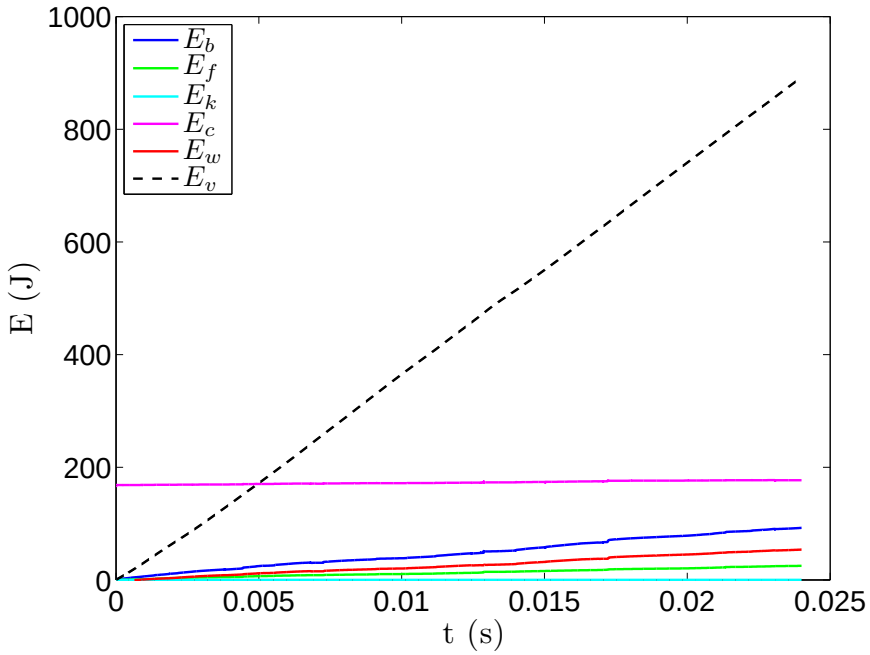

Figure 5.24: Energy partition during the injection process for injection rate 0.04 m^2/s.

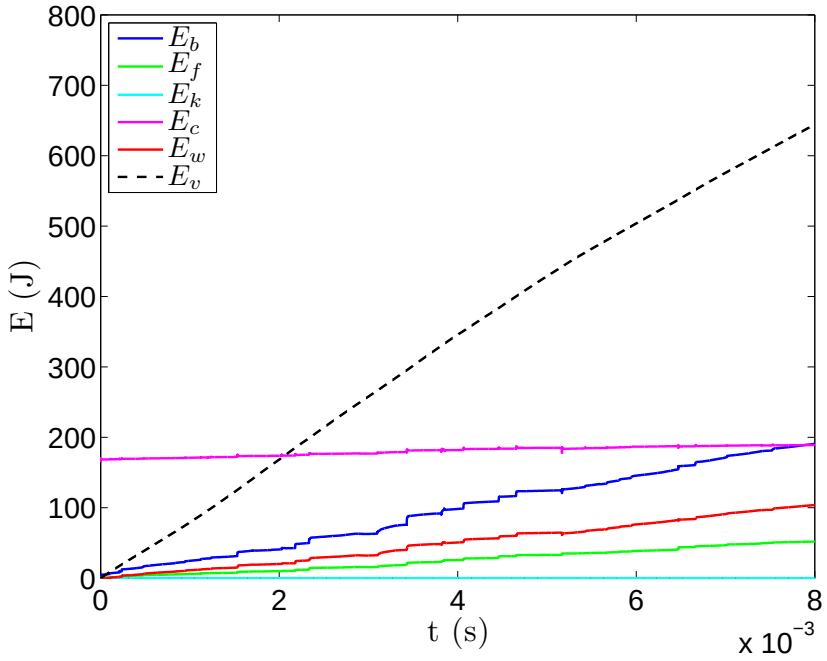

Figure 5.25: Energy partition during the injection process for injection rate 0.08 m^2/s.

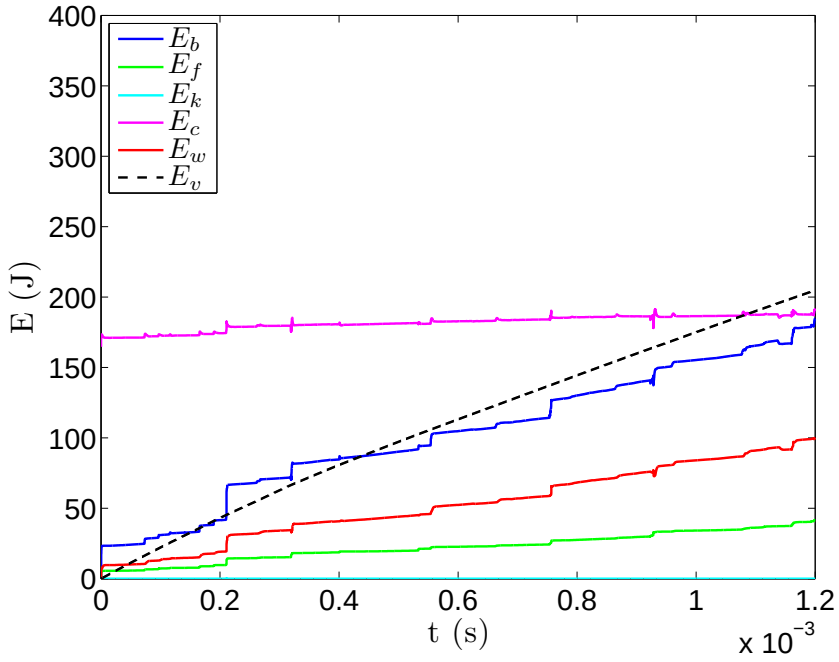

Figure 5.26: Energy partition during the injection process for injection rate 0.16 m^2/s.

5.6 Effect of Fluid Viscosity

To investigate the effect of fluid viscosity, two tests with injection fluid viscosity equal to 0.5 Pa·s and 2 Pa·s are carried out at the flow rate of 0.08 m^2/s.

Figures 5.27 and 5.28 show the fingering morphology and the borehole pressure history of the two tests. As can be seen in Figure 5.27, decreasing the fluid viscosity favors the infiltration process and hinders the fingering process; *vice versa*. Viscosity plays the similar role as the injection rate. Since these two cases have the same $v\eta$ with the tests with $\eta = 1$ Pa.s and $Q = 0.04$ and 0.16 m^2/s. The produced fingering patterns as well as the pressure histories for the same $v\eta$ are essentially the same.

5.7 Effect of Permeability

To investigate the effect of permeability, two assemblies are generated with the average particle radius 0.5 mm and 1 mm, respectively. Other parameters of these two assemblies are the same with the baseline sample in the series to investigate the injection flow rate. As the contact stiffnesses of the two tests remains unchanged,

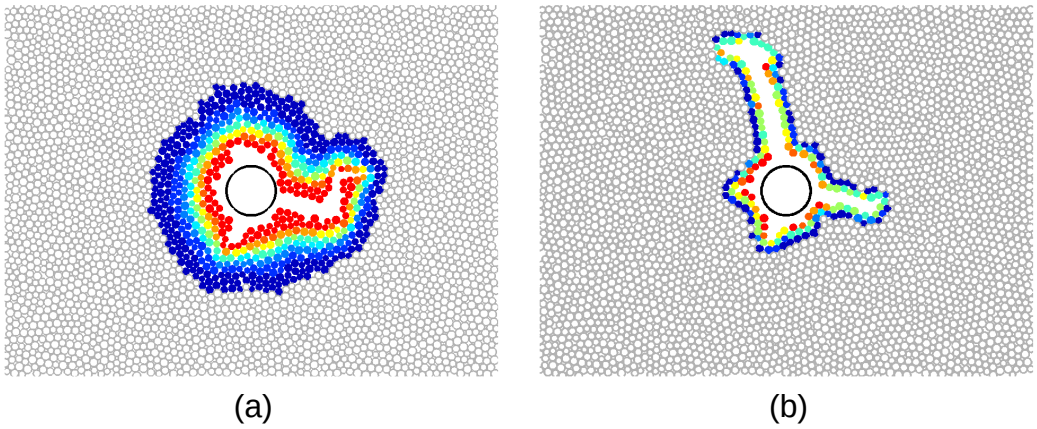

Figure 5.27: Displacement patterns for (a) $\eta = 0.5$ Pa·s at $t = 0.016$ s and (b) $\eta = 2$ Pa·s at $t = 0.0016$ s.

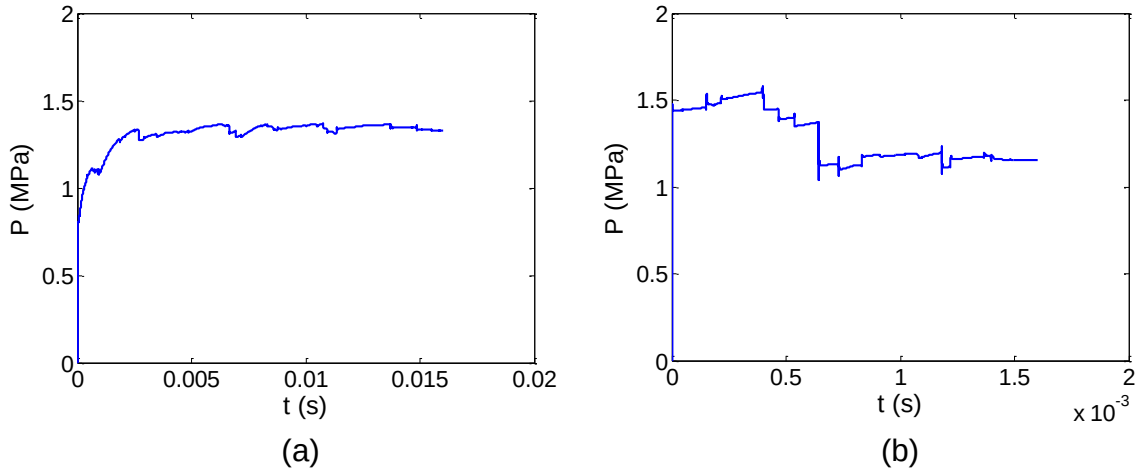

Figure 5.28: Borehole pressure history for (a) 0.5 Pa·s and (b) 2 Pa·s.

Table 5.4: Injection parameters for the effect of permeability.

Test	Particle radius (mm)	Permeability (m^2)	Modulus (MPa)
Test 1	0.5	6.037×10^{-10}	35.79
Test 2	1	2.779×10^{-9}	35.32

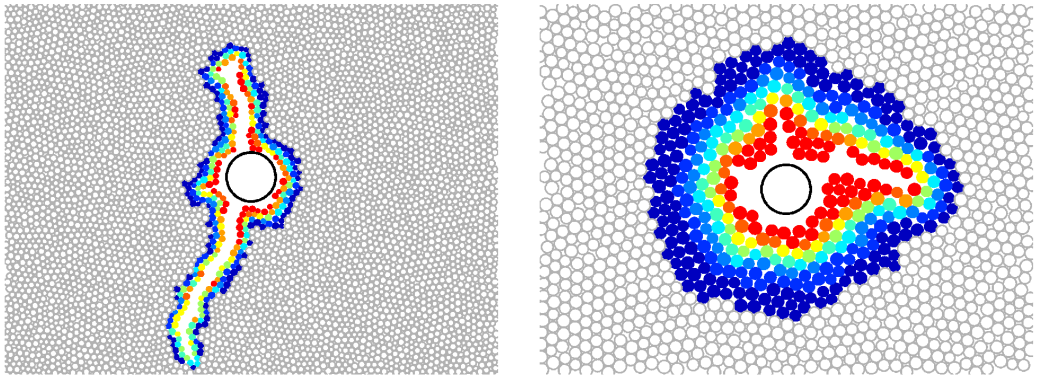

Figure 5.29: Displacement patterns for (a) $r = 0.5$ mm at $t = 0.0032$ s and (b) $r = 1$ mm at $t = 0.025$ s.

the elastic moduli of the two particle assemblies are expected to be the same as the baseline sample [Huang, 1999, Potyondy and Cundall, 2004]. However the permeability increases according to d_p^2. The measured permeability and modulus for the two assemblies are listed in Table 5.4. The injection rate for the two tests is fixed at 0.08 m^2/s and the fluid viscosity is 1 Pa·s.

Figures 5.29 and 5.30 show the fingering morphology and the borehole pressure history for the two tests . As can be seen in Figure 5.29, the fine grained assembly is more susceptible to fingering formation while the coarse grained assembly is more susceptible to the fluid permeation. It is interesting to note that the fine grain case in fact produced planar features, similar to the fracturing process in brittle materials.

5.8 Effect of Assembly Modulus

To investigate the effect of modulus, two assemblies are generated with the contact stiffness and confining stress being half of the baseline in one case and twice in the

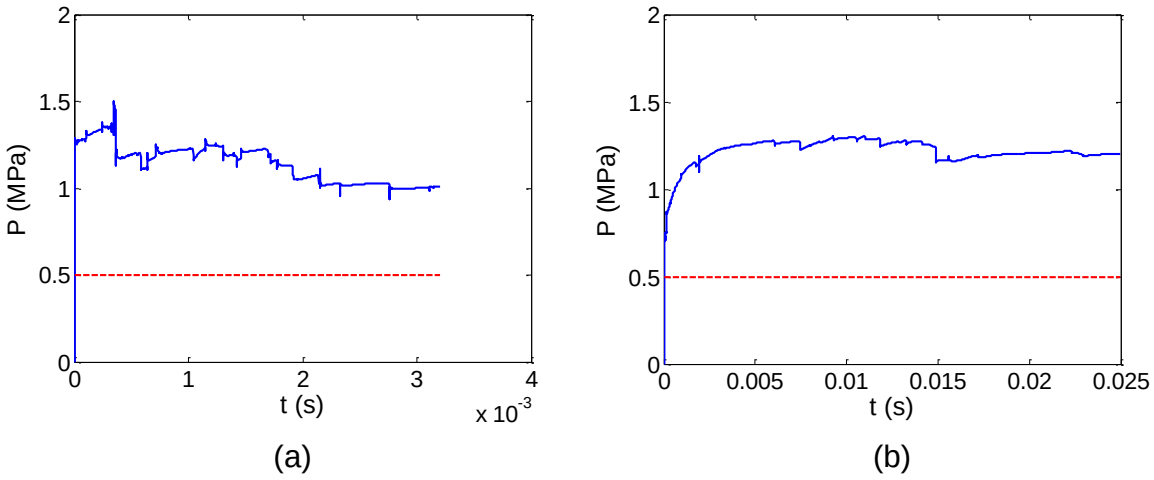

Figure 5.30: Borehole pressure history for (a) $r = 0.5$ mm and (b) $r = 1$ mm.

Table 5.5: Injection parameters for the effect of assembly modulus.

Test	Particle stiffness (N/m)	Confining (MPa)	Permeability (m^2)	Modulus (MPa)
Test 1	0.433×10^8	0.25	8.492×10^{-10}	19.57
Test 2	1.667×10^8	1	8.495×10^{-10}	61.53

other. The particle assembly configurations for the two tests are the same with the baseline test. Varying the contact stiffness and confining stress in the same ratio allows to maintain the assembly configuration and therefore guarantee the same macroscale permeability. The measured permeability and modulus for these two assemblies are listed in Table 5.5. The injection rate for the two tests is fixed at 0.08 m^2/s and the fluid viscosity is 1 Pa·s.

Figures 5.31 and 5.32 show the fingering morphology and the borehole pressure history of the two tests for the effect of assembly modulus. As can be seen in Figure 5.31, the low modulus assembly is prone to have fingering generated while the high modulus assembly is prone to have fluid flow in porous media. The results therefore support the dimensionless time τ_1 scaling in that increase in the modulus is equivalent to increase in permeability. The produced fingering patterns for these two tests are essentially the same with tests in the same τ_1 in the series for the effect of flow rate, i.e., Test 8 with $Q = 0.16$ m^2/s and Test 3 with $Q = 0.04$ m^2/s in Table 5.3.

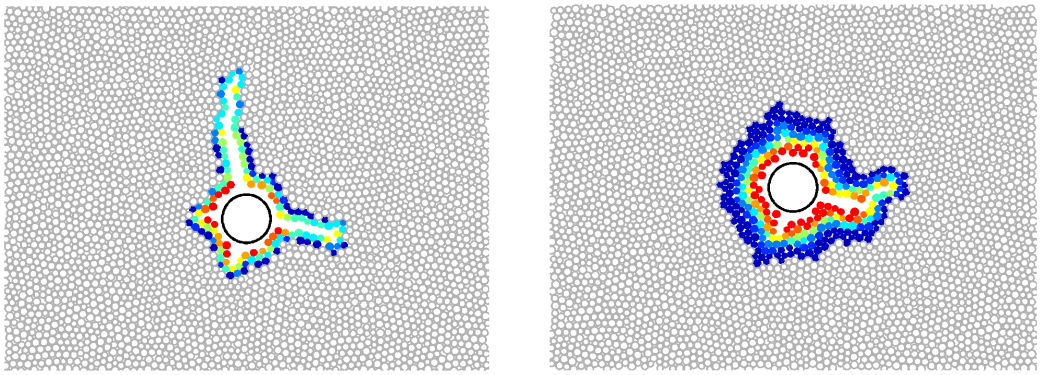

Figure 5.31: Displacement patterns for (a) $K_n = 0.433 \times 10^8$ N/m, $\sigma^{'} = 0.25$ MPa at $t = 0.0008$ s and (b) $K_n = 1.667 \times 10^8$ N/m, $\sigma^{'} = 1$ MPa at $t = 0.0144$ s.

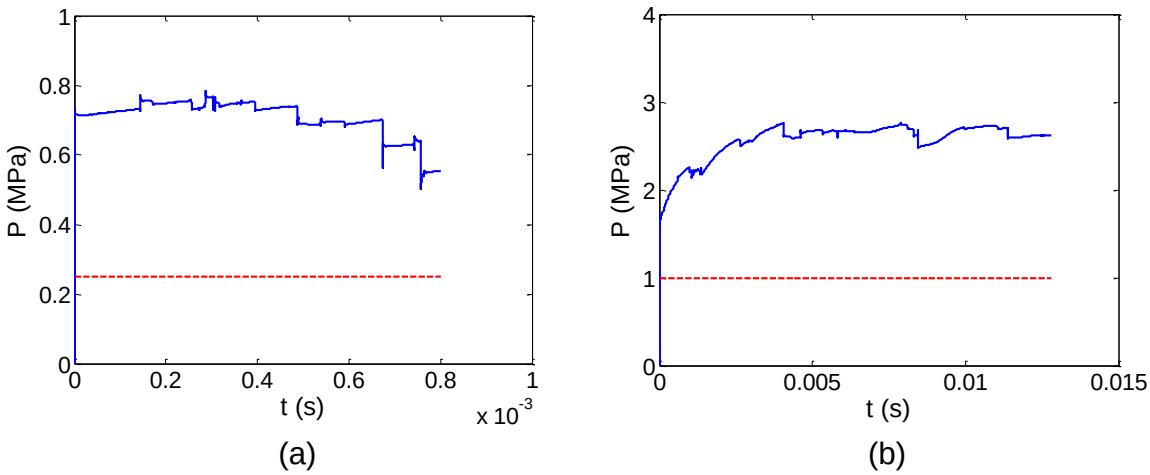

Figure 5.32: Borehole pressure history for (a) $K_n = 0.433 \times 10^8$ N/m, $\sigma^{'} = 0.25$ MPa and (b) $K_n = 1.667 \times 10^8$ N/m, $\sigma^{'} = 1$ MPa.

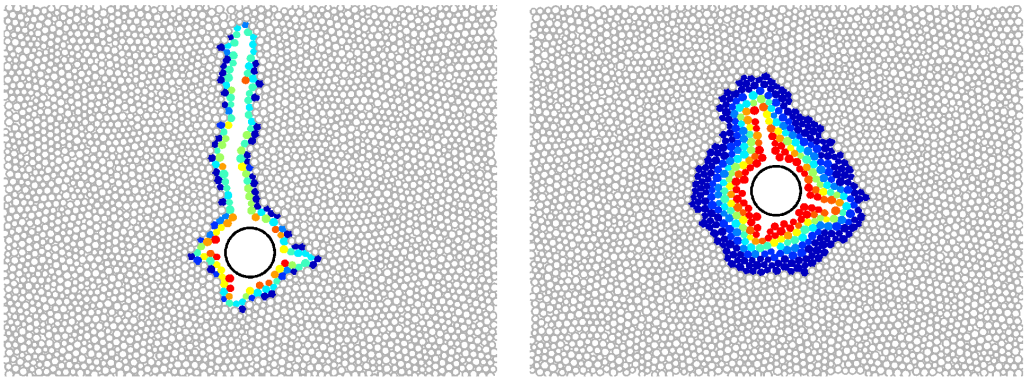

Figure 5.33: Displacement patterns for (a) $K_n = 0.433 \times 10^8$ N/m, $\sigma^{'} = 0.25$ MPa at $t = 0.0006$ s and (b) $K_n = 1.667 \times 10^8$ N/m, $\sigma^{'} = 1$ MPa at $t = 0.016$ s using a different assembly configuration.

To test the effect of particle assembly configuration, the two tests for the effect of assembly modulus are rerun by changing the initial particle assembly configuration. Figures 5.33 shows the fingering morphology of the two new tests. Compare to Figure 5.31, the fingering morphology in Figure 5.33 shows different locations of finger initiation. It means that the particle assembly configuration is a factor that affects the fingering profile.

5.9 Conclusions

In this work, the process of fluid injection into dense granular media is analyzed using the DEM code $PFC2D^{®}$ coupled with a pore network model. $PFC2D^{®}$ is employed to construct the granular media skeleton and execute the mechanical calculation. A pore network model scheme is developed to conduct the fluid flow analysis. Main findings from this analysis can be summarized as follows.

A systematic approach is developed to calibrate the microscale parameters to determine the permeability of a particle assembly according to the Kozeny-Carman correlation.

The effects of the injection flow rate, fluid viscosity, permeability and assembly modulus are investigated in the DEM/pore network model simulations. Increasing

the injection flow rate or fluid viscosity, or decreasing the assembly permeability or modulus all leads to a transition from simple radial flow pattern to localized failure in form of finger development.

Energy partition in the particle assembly and fluid flow is tracked during the injection process. Viscous dissipation is the dominant energy dissipation mechanism for the cases when the main phenomena is fluid flow in porous media. For those cases when fingering occurs, the drag force work gradually surpasses viscous dissipation as the main energy dissipation mechanism.

The numerical analysis indicates that the DEM/pore network coupling methodology is capable of reproducing the physical phenomena similar to those observed in the Hele-Shaw cell injection experiments.

Chapter VI

CONCLUSIONS AND FUTURE WORK

6.1 Conclusions

The objectives of this work are to investigate the fundamental failure mechanisms and flow patterns involved in fluid injection into dense granular media through an integrated experimental and theoretical analysis and to verify the conceptual hypothesis that in the injection process the granular media response will display a transition from the solid-like to the fluid-like behaviors.

The experimental findings with aqueous glycerin solution injected into dense dry sand conducted in a radial Hele-Shaw cell suggest that, given the same granular media properties, as the injection velocity and the fluid viscosity increase, there is a transition from the solid-like to the fluid-like behaviors in the granular media response, while fluid flow behavior shows a transition from infiltration-governed to infiltration-limited. Based on the patterns of grain displacements and fluid flow, four distinct displacement regimes can be identified from the experiments, namely, 1) a simple radial flow regime, 2) an infiltration- or leakoff-dominated regime, 3) a grain displacement-dominated regime, and 4) a viscous fingering-dominated regime. We argue that the formation of these displacement patterns to the competition among various forms of energy dissipation, i.e., viscous dissipation through flow in porous media, dissipation through grain displacements, and viscous dissipation through flow in thin channels.

The displacement regimes for the injection process in the Hele-Shaw cell are classified based on the considerations of three characteristic times: the injection time, the diffusion time that characterizes the hydromechanical coupling and the retardation time that describes the viscoelastoplatic response of the granular media. Two dimensionless times can be defined to classify the displacement regimes. The threshold values that define the transitions between the displacement regimes can be determined

from the variations of the global features such as the area ratio λ and the fractal dimensions of the finger and infiltration areas as functions of the dimensionless time τ_1. The finger growth mechanism is analyzed based on the images taken directly from the experiments and by using Particle Image Velocimetry technique. The evolution of the velocity field shows that the finger propagation has the sequence of tip blunting and splitting. The newly developed tip is at an angle of 45° with respect to the main branch, an indication that the tip propagates as a result of shear failure. The PIV results indicate that the shear strain rates are highly localized near the tip. The localized shear band at the tip may be below the resolution of this analysis.

Failure induced by fluid pressurization in a cylindrical wellbore in purely frictional media is analyzed using the discrete element method code $PFC3D^{®}$ with the coupled computational fluid dynamics add-on option. The numerical model corresponds to the case of injection in fully saturated media with the injection fluid being the same as the pore fluid in the matrix. Depending on the injection velocity, three types of responses can be identified for the behaviors of the particle assembly. When the flow velocity is relatively small, fluid simply permeates through the particle assembly and the response is similar to flow in a fixed bed. In the intermediate velocity range, the wellbore expands initially and then becomes distorted. Distortion of the wellbore leads to localized failure in form of shear bands. At large injection velocities, the wellbore experiences nearly uniform expansion and the near wellbore region is fluidized. Critical velocities corresponding to the transitions from a fixed bed flow type of behavior, to localized failure, and to the fluidization scenario can be identified from the variation of the normalized wellbore expansion rate as a function of the injection velocity.

The process of fluid injection into dense granular media is analyzed using the DEM code $PFC2D^{®}$ coupled with a pore network model. The effects of the injection flow rate, fluid viscosity, permeability and assembly modulus are investigated in the DEM/pore network model simulations. Increasing the injection flow rate or fluid viscosity, or decreasing the assembly permeability or modulus all leads to a transition from simple radial flow pattern to localized failure in form of finger development.

Energy partition in the particle assembly and fluid flow is tracked during the injection process. Viscous dissipation is the dominant energy dissipation mechanism for the cases when the main phenomena is fluid flow in porous media. For those cases when fingering occurs, the drag force work gradually surpasses viscous dissipation as the main energy dissipation mechanism. The numerical analysis indicates that the DEM/pore network coupling methodology is capable of reproducing the physical phenomena similar to those observed in the Hele-Shaw cell injection experiments.

6.2 Recommendations for Future Work

Based on the research results from this work, we suggest the following future work.

- Effects such as particle size and fluid properties (Non-Newtonian rheology) should be explored in the Hele-Shaw cell experiments.
- More PIV tests are needed to verify the finger growth mechanisms.
- The current Hele-Shaw experiments only record the inlet fluid pressure. Fluid pressure measurement in the whole domain could be implemented by using tactile pressure sensors.
- The current pore network model only considers the friction between particles. A viscosity component should be added into the contact model in order to model the viscoelastic response in the granular media.
- The borehole as well as the generated fingers is considered as one big pore during the pore network simulation. A fluid flow model needs to be applied inside the borehole and fingers.

Appendix A

LIST OF HELE-SHAW CELL EXPERIMENTS

Test name	b (in)	Q (ml/min)	η (cp)
Aug11_1_100_0.062_100	0.062	100	942
Aug11_2_100_0.093_70	0.093	70	942
Aug11_3_100_0.125_20	0.125	20	942
Aug11_4_100_0.031_50	0.031	50	942
Aug11_5_100_0.125_2.5	0.125	2.5	942
Aug11_6_100_0.125_35	0.125	35	942
Aug12_1_100_0.031_100	0.031	100	942
Aug12_2_100_0.031_80	0.031	80	942
Aug12_3_100_0.031_10	0.031	10	942
Aug12_4_100_0.125_60	0.125	60	942
Aug13_1_100_0.125_80	0.125	80	942
July12_1_100_0.031_125 (C4)	0.031	125	942
July14_1_100_0.031_25	0.031	25	942
July14_2_100_0.062_50	0.062	50	942
July14_3_100_0.062_25	0.062	25	942
July14_4_100_0.125_5 (C1)	0.125	5	942
July14_5_100_0.062_25	0.062	25	942
July21_1_100_0.062_50	0.062	50	942

Test name	b (in)	Q (ml/min)	η (cp)
July22_1_100_0.031_125	0.031	125	942
July26_1_100_0.062_25 (C2)	0.062	25	942
July29_1_100_0.062_50 (C3)	0.062	50	942
Aug10_3_90_0.093_10	0.093	10	176
Aug17_1_90_0.031_10	0.031	10	176
Aug17_2_90_0.062_80	0.062	80	176
Aug3_2_90_0.062_10	0.062	10	176
Aug3_3_90_0.062_5	0.062	5	176
Aug6_1_90_0.062_6	0.062	6	176
Aug6_2_90_0.062_8	0.062	8	176
Aug9_1_90_0.031_100	0.031	100	176
July16_1_90_0.062_25 (B2)	0.062	25	176
July16_2_90_0.031_25	0.031	25	176
July16_3_90_0.031_125	0.031	125	176
July16_4_90_0.031_25	0.031	25	176
July16_5_90_0.125_5 (B1)	0.125	5	176
July20_2_90_0.062_50	0.062	50	176
July20_3_90_0.062_50	0.062	50	176
July20_4_90_0.031_125	0.031	125	176
July20_5_90_0.031_125	0.031	125	176
July22_2_90_0.031_125 (B4)	0.031	125	176
Sep10_1_90_0.062_50 (B3)	0.062	50	176

Test name	b (in)	Q (ml/min)	η (cp)
Sep22_1_90_0.125_1	0.125	1	176
Sep23_1_90_0.125_2.5	0.125	2.5	176
Sep24_1_90_0.125_1.5	0.125	1.5	176
Aug13_2_50_0.125_100	0.125	100	5
Aug13_3_50_0.031_45	0.031	45	5
Aug13_4_50_0.031_60	0.031	60	5
Aug20_1_50_0.062_13	0.062	13	5
Aug20_2_50_0.062_10	0.062	10	5
Aug20_3_50_0.125_12	0.125	12	5
Aug3_1_50_0.062_125	0.062	125	5
July19_1_50_0.031_25	0.031	25	5
July19_3_50_0.031_125 (A4)	0.031	125	5
July19_4_50_0.062_25	0.062	25	5
July19_5_50_0.062_25 (A2)	0.062	25	5
July19_6_50_0.125_5 (A1)	0.125	5	5
July20_1_50_0.062_50 (A3)	0.062	50	5

Bibliography

A. Al-Busaidi, J. F. Hazzard, and R. P. Young. Distinc element modeling of hydraulically fractured Lac du Bonnet granite. *J. Geophys. Res.*, 110:B06302, 2005.

A. Alsiny, I. Vardoulakis, and A. Drescher. Deformation localization in cavity inflation experiments on dry sand. *Geotechnique*, 42(3):395–410, 1992.

G. Batchelor. *An Introduction to Fluid Dynamics*. Cambridge University Press, Cambridge UK, 1967.

J. Bear. *Dynamics of Fluids in Porous Media*. Dover Publications, 1988.

D. Bensimon, L. P. Kadanoff, S. Liang, B. I. Shraiman, and C. Tang. Viscous flows in two dimensions. *Rev. Mod. Phys.*, 58:977–999, 1986.

M. Biot. General theory of three-dimensional consolidation. *J. Appl. Phys.*, 12: 155–164, 1941.

B. Bohloli and C. J. de Pater. Experimental study on hydraulic fracturing of soft rocks: Influence of fluid rheology and confining stress. *J. Petro. Sci. Eng.*, 53:1–12, 2006.

W. Borchardt-Ott. *Crystallography: An introduction*. Springer, 2011.

H. Chang. *Hydraulic fracturing in particulate materials*. PhD thesis, Georgia Institute of Technology, 2004.

X. Cheng, L. Xu, A. Patterson, H. M. Jaeger, and S. R. Nagel. Towards the zero-surface-tension limit in granular fingering instability. *Nat. Phys.*, 4:234–237, 2008.

C. Chevalier, A. Lindner, M. Leroux, and E. Clément. Morphodynamics during air injection into a confined granular suspension. *J. Non-Newtonian Fluid Mech.*, 158: 63–72, 2009.

R. L. Chouke, P. van Meurs, and C. van der Poel. The instability of slow, immiscible, viscous liquid-liquid displacements in permeable media. *Trans. AIME*, 216:188–194, 1959.

P. Coussot. *Flows of concentrated granular mixtures*, chapter 12, pages 291–315. Taylor & Francis, 2002.

P. Cundall. Fluid formulation for PFC2D. Itasca Consulting Group, 2000.

B. Damjanac, I. Gil, M. Pierce, M. Sanchez, A. van As, and J. McLennan. A new approach to hydraulic fracturing modeling in naturally fractured reservoirs. In *44th U.S. Rock Mech./Geomech. Symp., Salt Lake City*, 2010.

R. de Felice. The voidage function for fluid-particle interaction systems. *Int. J. Multiphase Flow*, 20:153–159, 1994.

C. J. de Pater and Y. Dong. Experimental study of hydraulic fracturing in sand as a function of stress and fluid rheology. *SPE 105620 presented at the 2007 Hydraulic Fracturing Technology Conference, College Station, Texas*, 2007.

E. Detournay. Propagation regimes of fluid-driven fractures in impermeable rocks. *Int. J. Geomech.*, 4(1):35–45, 2004.

E. Detournay and A. H.-D. Cheng. Poroelastic response of a borehole in a non-hydrostatic stress field. *Int. J. Rock Mech. Min. Sci.*, 25(3):171–182, 1988.

E. Detournay, A. P. Peirce, and A. Bunger. Viscosity-dominated hydraulic fractures. In *Proc. 1st Canada-US Rock Mechanics Symposium - Rock Mechanics Meeting Society's Challenges and Demands*. Taylor and Francis/Balkema, 2007.

Y. Dong. *Hydraulic fracture containment in sand*. PhD thesis, Delft Institute of Technology, 2010.

Y. Dong and C. de Pater. Observation and modeling of the hydraulic fracture tip in sand. In *Proc. 42nd U.S. Rock mechanics Symposium and 2nd U.S.-Canada Rock Mechanics Symposium*, San Francisco, CA, 2008.

F. Dullien. *Porous media fluid transport and pore structure.* Academic Press, 1991.

R. Ehrlich and B. Weinberg. An exact method for characterization of grain shape. *J. Sediment. Res.*, 40:205–212, 1970.

A. Einstein. Eine neue bestimmung der molekdldimensionen. *Ann. Physik*, 19:289–306, 1905.

I. Fatt. The network model of porous media I. Capillary pressure characteristics. *Trans. AIME*, 207, 1956a.

I. Fatt. The network model of porous media II. Dynamic properties of a single size tube network. *Trans. AIME*, 207, 1956b.

I. Fatt. The network model of porous media III. Dynamic properties of networks with tube radius distribution. *Trans. AIME*, 207, 1956c.

D. Garagash and E. Detournay. An analysis of the influence of the pressurization rate on the borehole breakdown pressure. *Int. J. Solids Structures*, 34(24):3099–3118, 1997.

GeoDelft. *Hydraulic fracturing with distinct element method.* 2002.

E. Golovin, H. Jasarevic, A. Chudnovsky, J. W. Dudley, and G. K. Wong. Observation and characterization of hydraulic fracturing in cohesionless sand. *Proc. 44th U.S. Rock Mech. Symp., Salt Lake City, UT*, 2010.

S. A. Hall, D. M. Wood, E. Ibraim, and G. Viggiani. Localised deformation patterning in 2D granular materials revealed by digital image correlation. *Granul. Matter.*, 12:1–14, 2010.

J. F. Hazzard, R. P. Young, and S. J. Oates. Numerical modelling of seismicity induced by fluid injection in a fractured reservior. In *Proceedings of the Fifth North American Rock Mechanics Symposium*, volume Vol.3, pages 249–255, Moorea, French Polynesia, 2002. Antenne Museum - EPHE.

R. Hill. *The Mathematical Theory of Plasticity.* The Oxford Engineering Science Series. Oxford University Press, 1950.

T. Hirata. Fracturing due to fluid intrusion into viscoelastic materials. *Phys. Rev. E*, 57:1772–1779, 1998.

G. Homsy. Viscous fingering in porous media. *Ann. Rev. Fluid Mech.*, 19:271–311, 1987.

H. Huang. *Discrete Element Modeling of Tool-Rock Interaction.* PhD thesis, University of Minnesota, 1999.

H. Huang and E. Detournay. Cylindrical cavity expansion from a finite radius. In *Deep Foundations and Geotechnical In-situ Testing, ASCE GSP 205*, 2010.

R. Hurt. *Toughness-dominated hydraulic fractures in cohesionless particulate materials.* PhD thesis, Georgia Institute of Technology, 2012.

International Center for Numerical Methods in Engineering (CIMNE). *GID Reference Manual 8.0.* 2008. Minneapolis, Minnesota.

Itasca Consulting Group. *FLAC User Manual.* 2005. Minneapolis, Minnesota.

Itasca Consulting Group. *PFC3D 4.00 User Manual.* 2008. Minneapolis, Minnesota.

ITOCHU Technology Solution Corporation. *CCFD User Manual.* 2008. Minneapolis, Minnesota.

H. Jasarevic, E. Golovin, A. Chudnovsky, J. W. Dudley, and G. K. Wong. Observation and modeling of hydraulic fracturing initiation in cohesionless sand. *Proc. 44th U.S. Rock Mech. Symp., Salt Lake City, UT*, 2010.

O. Johnsen, R. Toussaint, K. J. Maloy, and E. G. S. Flekkoy. Pattern formation during air injection into granular materials confined in a circular Hele-Shaw cell. *Phys. Rev. E*, 74(1):011301, 2006.

O. Johnsen, C. Chevalier, A. Lindner, R. T. E. Clement, K. J. Maloy, E. G. Flekkoy, and J. Schumittbuhl. Decompaction and fluidization of a saturated and confined granular medium by injection of a viscous liquid or gas. *Phys. Rev. E*, 78(1):051302, 2008a.

O. Johnsen, R. Toussaint, K. J. Maloy, E. G. Flekkoy, and J. Schumittbuhl. Coupled air/granular flow in a linear Hele-Shaw cell. *Phys. Rev. E*, 77(1):011301, 2008b.

M. Khodaverdian and P. McElfresh. Hydraulic fracturing stimulation in poorly consolidated sand: Mechanisms and consequences. *SPE 63233 presented at the SPE Annual Technical Conference and Exhibition, Dallas, TX*, 2000.

E. Lemaire, P. Levitz, G. Daccord, and H. V. Damme. From viscous fingering to viscoelastic fracturing in colloidal fluids. *Phys. Rev. Lett.*, 67(15):2009–2012, 1991.

R. Lenormand, E. Touboul, and C. Zarcone. Numerical models and experiments on immiscible displacements in porous media. *J. Fluid Mech.*, 189:165–187, 1988.

L. Li. *Particle scale reservoir mechanics.* PhD thesis, Norwegian University of Science and Technology, 2002.

L. Li and R. Holt. Particle scale reservoir mechanics. *Oil Gas Sci.Technol.*, 57: 525–538, 2002.

C. W. Macosko. *Rheology: Principles, Measurements, and Applications.* Wiley-VCH, 1994.

L. Murdoch. Hydraulic fracturing of soil during laboratory experiments: methods and observations. *Géotechnique*, 43(2):255–265, 1993a.

L. Murdoch. Hydraulic fracturing of soil during laboratory experiments: propagation. *Géotechnique*, 43(2):266–276, 1993b.

L. Murdoch. Hydraulic fracturing of soil during laboratory experiments: theoretical analysis. *Géotechnique*, 43(2):277–287, 1993c.

L. Paterson. Radial fingering in Hele-Shaw cell. *J. Fluid Mech.*, 113:513–529, 1981.

L. Paterson. Diffusion-limited aggregation and two-fluid displacements in porous media. *Phys. Rev. Lett.*, 52:1621–1624, 1984.

S. Pinto, M. Couto, A. Atman, S. Alves, A. Bernardes, H. de Resende, and E. Souza. Granular fingers on jammed systems: new fluidlike patterns arising in grain-grain invasion experiments. *Phys. Rev. Lett.*, 99(068001), 2007.

D. Potyondy and P. Cundall. A bonded-particle model for rock. *Int. J. Rock Mech. Min. Sci.*, 41(8):1329–1364, 2004.

M. Raffel, C. Willert, S. Wereley, and J. Kompenhans. *Particle image velocimetry: a practical guide*. Springer-Verlag, 2007.

A. L. Rechenmacher and R. J. Finno. Digital image correlation to evaluate shear banding in dilative sands. *Geotech. Test. J.*, 27:13–22, 2004.

P. Saffman and G. Taylor. The penetration of a fluid into a porous medium or Hele-Shaw cell containing a more viscous liquid. *Proc. R. Soc. Lond. A*, 245(1242): 312–329, 1958.

M. Schroeder. *Fractals, chaos, power laws: minutes from an infinite paradise*. New York : W.H. Freeman, 1991.

H. Shin and J. C. Santamarina. Fluid-driven fractures in uncemented sediments: Underlying particle-level processes. *Earth & Plan. Sci. Lett.*, 299:180–189, 2010.

K. Soga, S. Au, M. Jafari, and M. Bolton. Laboratory investigation of multiple grout injections into clay. *Géotechnique*, 54(2):81–90, 2004.

K. Soga, K. Gafar, M. Ng, and S. Au. Macro and micro behaviour of soil fracturing. In *Proc. the International Symposium on Geomechanics and Geotechnics of Particulate Media*, pages 421–427, 2006.

J. J. Stickel and R. L. Powell. Fluid mechanics and rheology of dense suspensions. *Annu. Rev. Fluid Mech.*, 37:129–149, 2005.

The Soap and Detergent Association. Glycerine: an overview. Technical report, 1990.

W. Thielicke and E. J. Stamhuis. PIVlab: http://pivlab.blogspot.com/, 2012.

Y. Tsuji. Multi-scale modeling of dense phase gas-particle flow. *Chem. Engng. Sci.*, 62(3410-3418), 2007.

Y. Tsuji, T. Kwaguchi, and T. Tanata. Discrete particle simulation of two-dimensional fluidized bed. *Powder Tech.*, 77:79–87, 1993.

D. Turcotte. *Fractals and chaos in geology and geophysics.* Cambridge University Press, 1997.

H. van Damme, E. Lemaire, Y. Abdelhaye, A. Mourchid, and P. Levitz. Pattern formation in particulate complex fluids: a guided tour. In K. Bardhan, B. Chakrabarti, and A. Hansen, editors, *Non-linearity and breakdown in soft condensed matter*, Lecture Notes in Physics. Springer-Verlag, 1993.

T. Vicsek. *Fractal growth phenomena.* World Scientific, 1992.

J. Wesrerweel. *Digital particle velocimetry - theory and application.* Delft University Press, 1993.

D. Wilkinson and J. F. Willemsen. Invasion percolation: a new form of percolation theory. *J. Phys. A: Math. Gen.*, pages 3365–3376, 1983.

T. A. Witten and L. M. Sander. Diffusion-limited aggregation, a kinetic critical phenomenon. *Phys. Rev. Lett.*, 47:1400–1403, 1981.

H. Xu and A. Yu. Numerical simulation of the gas-solid flow in a fluidized bed by combining discrete particle method with computational fluid dynamics. *Chem. Engng. Sci.*, 52(16):2785–2809, 1997.

H. Zhao and J. V. Maher. Associated-polymer effects in a Hele-Shaw experiment. *Phys. Rev. E*, 47:4278–4283, 1993.

X. P. Zhao and R. P. Young. Numerical simulation of seismicity induced by hydraulic fracturing in naturally fractured reservoirs. *SPE 124690 presented at the SPE Annual Technical Conference and Exhibition, New Orleans, LA*, 2009.

R. W. Zimmerman and G. S. Bodvarsson. Hydraulic conductivity of rock fractures. *Transport Porous Med.*, 23:1–30, 1996.

VITA

Fengshou Zhang was born on October 5th (August 19th in Chinese lunar calendar), 1982 in Lianyuan, Hunan Province in central China. He obtained his BS in Civil Engineering (2004) and MS in Geotechnical Engineering (2007) from Tongji University in Shanghai, China. In August 2007, he started his graduate research in the Geosystems Engineering Group at Georgia Institute of Technology under the supervision of Dr. Haiying Huang. He obtained a MS (2010) and will receive his PhD degree in Civil Engineering in May 2012 from Georgia Institute of Technology.